Doctoral Thesis

Theoretical Reaction Mechanism Study on Organic and Inorganic Materials for Renewable Energy and Environment

Jin Chul Kim

School of Energy and Chemical Engineering

(Chemical Engineering)

Ulsan National Institute of Science and Technology

2023

Theoretical Reaction Mechanism Study on Organic and Inorganic Materials for Renewable Energy and Environment

Jin Chul Kim

School of Energy and Chemical Engineering

(Chemical Engineering)

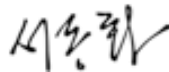Ulsan National Institute of Science and Technology

Theoretical Reaction Mechanism Study on Organic and Inorganic Materials for Renewable Energy and Environment

A thesis/dissertation submitted to

Ulsan National Institute of Science and Technology

in partial fulfillment of the

requirements for the degree of

Doctor of Philosophy

Jin Chul Kim

12.06.2022 of submission

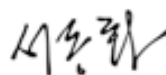Approved by

_____

Advisor

Dong-Hwa Seo

Theoretical Reaction Mechanism Study on Organic and Inorganic Materials for Renewable Energy and Environment

Jin Chul Kim

This certifies that the thesis/dissertation of Jin Chul Kim is approved.
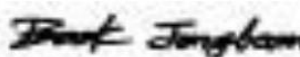
12.06.2022 of submission

Signature

Advisor: Dong-Hwa Seo

Signature

Co-advisor: Sang Kyu Kwak

Signature

Jong-beom Baek

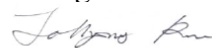Signature

Kwangjin An

Signature

Ja Hyoung Ryu

Signature

Yoon Seok Jung

Abstract

Concerning about the increases of energy demand and environmental issue have let to the development of renewable energy with low greenhouse gas emissions. To produce the industrial compounds without fossil fuel consumption, the themes of research on renewable energy have been focused towards to the method to produce the chemical materials by using earth-abundant resources such as plants, wind, and solar energy. However, the low efficiency, high initial cost of installation, and discontinuity of source acquirement of renewable energy are still slowing down its application. To overcome these challenges, renewable energy technologies still need to be improved.

Effective and technological developments to the practical application of renewable energy are derived from in-depth understanding of reactions related to renewable energy and environment. Furthermore, novel materials and strategies can be established by combining theoretical approaches and knowledge of reactions. In this context, Molecular modeling and simulation are the appropriate method to investigate the reaction mechanism for desired substances or to identify the cause of a phenomenon at the atomic level. In this thesis, we described the theoretical research on the reaction mechanism related with renewable energy system.

In Chapter 1, we introduce shortly the renewable energy systems and the mechanistic studies for in-depth understanding of chemical engineering. Also, we described the previous and ongoing research about the renewable technologies and applications using molecular simulation methods. Finally, we explained the multi-scale molecular simulation method and its theoretical meanings used in this thesis, including the density functional theory (DFT) calculation, molecular dynamics (MD), and Monte Carlo (MC) simulation.

In Chapter 2, we suggested the new strategy for formation of desired organic materials from biomass (renewable energy source) with highly effective catalysts. First, it was found that solvent effect of 1-butanol and the catalytic performance of hydrotalcite in glucose isomerization mechanism using DFT calculation. Furthermore, the reaction mechanistic pathways for the fructose hydrogenation to mannitol and sorbitol which is used as the biomass, were investigated by DFT calculation. The catalytic effect of the Cu metal catalyst favorably induced the formation of mannitol than the formation of sorbitol during the fructose adsorption step.

In Chapter 3, we theoretically demonstrated that the formic acid and supercritical ethanol mixture solvents expedited the solvothermal liquefaction reaction of biomass lignin constituents. Using the reactive molecular dynamics simulation and density functional theory calculation, the mechanisms by

which solvents break C−O bond and C−C bond in each Dilignol molecule were observed over time. In this liquefaction reaction, the hydrogen detached from the formic acid directly participates in dissociation of C−O bond and C−C bond, and the supercritical ethanol transfers the radical hydrogen from formic acid to dilignol. This mechanism study suggested the biomass utilization method that can produce a lot of hydrogen without a metal catalyst.

In Chapter 4, we theoretically proposed the feasibility of universal synthesis of the metal sulfide electrolyte that can improve the performance of all solid-state battery developed for effective storage of renewable energy and reduced carbon footprint. Using an alkahest solvent system composed of EDA-EDT mixture solvents, not only conventional sulfide SE precursors of Li_2S, P_2S_5, and Na_2S, but also metal sulfides, such as GeS_2 were fully dissolved by nucleophilic attack of thiolate. It was elucidated that EDT molecules have strong dissolving power by proton transfer to EDA and that the dissolution of sulfide precursors is feasible through the investigation of reaction mechanism.

In Chapter 5, we provided the insight of mineral carbonation reaction for carbon dioxide storage and utilization using DFT calculation and MD simulation. Calcium hydroxide has been mainly studied as a medium for mineral carbonation, but its efficiency was not good. In this study, we revealed that water molecules are intercalated in interlayer of calcium hydroxide and the interlayer distance between the calcium hydroxide increases. Remarkably, the water molecules near the surface of the calcium hydroxide accelerated the carbonation phenomenon of CO_2 through the studies.

Contents

List of Figures

Chapter 1

in each reaction step are omitted.

Figure 2.2.10   Binding energies of fructose ($\Delta E_{B.E.}$) and mannitol selectivity ($\Delta\Delta E_{B.E.}$) in each solvent.

Chapter 3

and red, respectively.

Chapter 4

the Ge atoms are depicted using the ball-and-stick model, and the deprotonated EDT molecules are depicted using the stick model. The remaining atoms are indicated as lines. The dissolved three Ge atoms are colored pink, and the remaining Ge, C, S, N, and H atoms are colored green, gray, yellow, blue, and white, respectively

Chapter 5

Chapter 6

Chapter 1. Introduction

1.1 General introduction to renewable energy and the environment

Currently, many of the world's economies are facing increasing energy demand and environmental pollution. **Figure 1.1** depicts the current global energy consumption, which indicates that more than 80% of the world's energy originates from fossil fuels, such as coal, oil, and natural gas.[1] The excessive consumption of these resources is not only rapidly depleting fossil fuel reserves, but it is also causing a detrimental effect on the environment owing to the release of large amounts of greenhouse gases such as carbon dioxide (CO_2).[2-4] Renewable and environmentally friendly energy sources, such as biofuel, biomass, and sustainable solar energy, are required to meet the current energy demand and address environmental issues, and they are garnering increasing interest. Renewable energy sources have considerable potential to provide energy with almost zero greenhouse gas emissions, diversify the energy supply, and reduce dependence on fossil fuels (**Figure 1.2**).[5,6] However, many problems, such as high financial risks, legal regulation, low availability of renewable resources, and low power quality, remain even though significant research is being conducted to develop renewable technologies, such as technologies for producing desired products while reducing carbon footprints, methods for synthesizing industrial chemicals while minimizing CO_2 formation using biomass, and technologies for carbon capture and utilization (**Figure 1.3**).[7-10] To overcome these challenges, in-depth knowledge of environmental and renewable energy-related reactions is required, and novel materials or strategies for increasing efficiency must be designed based on this knowledge.
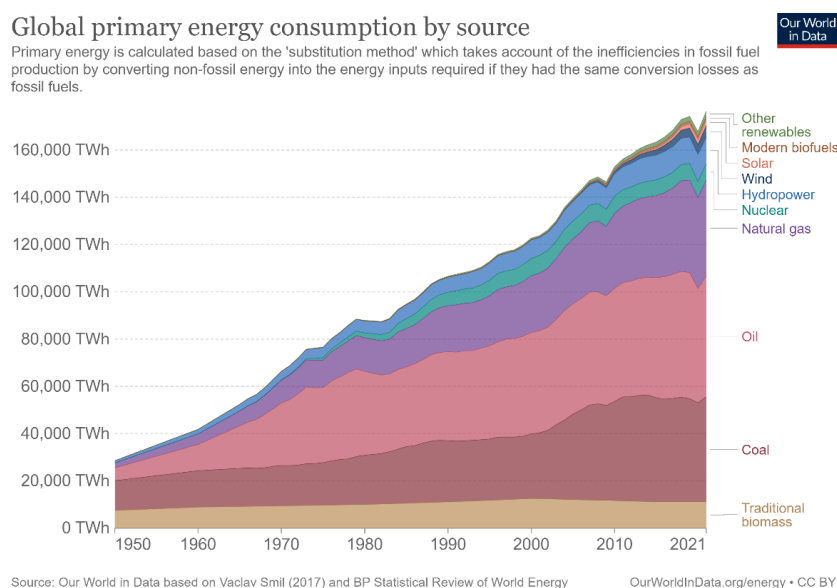
Figure 1.1. Global primary energy consumption until 2021. Obtained from Energy Transitions: Global and National Perspectives in ref. 1.
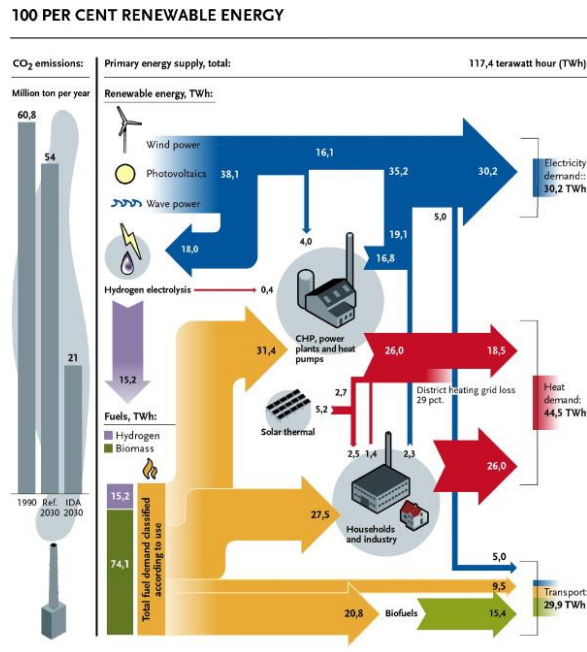
Figure 1.2. Flow diagram of a 100% renewable energy system. Reproduced with permission from ref. 6. Copyright 2008 Elsevier Ltd.

1.2 Mechanistic study: an in-depth understanding of chemical reactions

Most engineering-related industries, such as industries that produce energy and organic materials by refining petrochemical raw materials, industries that produce batteries for automobiles and electric devices, food and pharmaceutical industries, and technology industries that produce clean energy and pollutant treatment for environmental preservation, are closely related to chemical reactions.[11−14] However, each application has numerous issues, such as low catalyst performance and uneconomical synthesis methods, because it is challenging to precisely monitor chemical reaction processes (**Figure 1.3**), but these issues can be solved by theoretically studying reaction mechanisms.
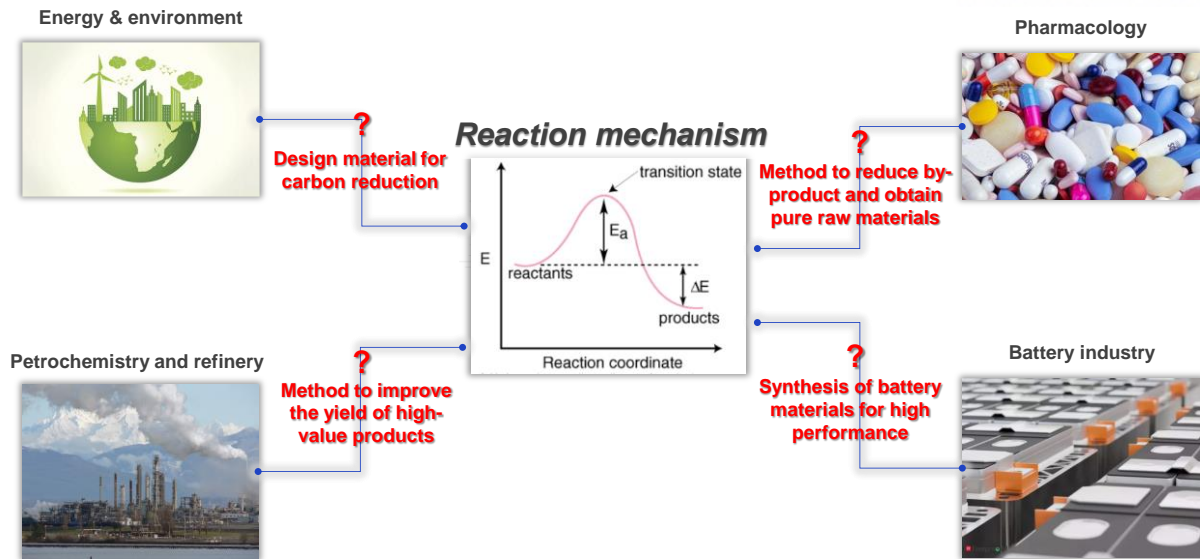
Figure 1.3. Schematic of the reaction mechanism for solving issues in chemical engineering.

A reaction mechanism or reaction pathway describes the successive steps that occur at the molecular level in a chemical reaction. Chemical reactions are quite complex and involve many factors. In particular, even a simple reaction has various possible pathways, depending on external conditions. As shown in **Figure 1.4**, there are many different pathways composed of elementary reactions that depend on molecules in the intermediate steps in an overall reaction where one A_2 molecule reacts with two B_2 molecules to form two AB_2 molecules. The fundamental and theoretical knowledge underlying molecular reactions must be understood because of their complexity and diversity, and the reaction mechanisms should be investigated to validate and comprehend how reactions proceed.
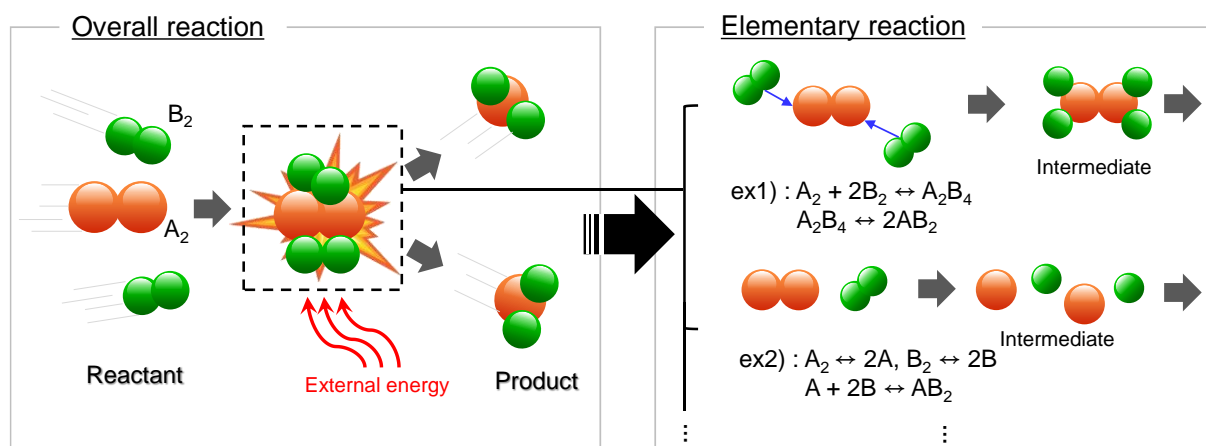
Figure 1.4. Schematic of the overall reaction and elementary reactions.

To thoroughly understand chemical reactions, it is necessary to analyze the activation energy and heat of reaction for each reaction mechanism step and to identify the rate-determining step (RDS) with the highest activation energy among all reaction steps. A transition state is a state that has the highest potential energy in the reaction coordinate (**Figure 1.5**). The activation energy is calculated as the difference between the transition state energy and the reactant energy. The following Arrhenius equation demonstrates that a reaction with high activation energy has a low reaction rate constant, resulting in extremely sluggish reactions:[15]

$$k(T) = Aexp(^{-E_a}/_{kT}),$$

where E_a is the activation energy, $k(T)$ is the rate constant, and A is the pre-exponential factor, which is related to the number of atomic collisions per unit time. Menzinger and Wolfgang[15] stated that the pre-exponential factor is expressed as an excitation function ($\sigma(E)\ or\ \sigma(V)$), which is an energy-dependent or velocity-dependent cross-section. Since the activation step of chemical reactions always includes a collisional process, the probability of collisional reactions can be expressed using the $\sigma(V)$ cross-section, which is defined for collisions at the relative velocity as follows:

$$Rate = -\left(\frac{dn_A}{dt}\right)_v = \sigma(v)vn_An_B,$$

where n_A and n_B are the A and B reactant concentrations, respectively. Assuming that $F(T,v)$ is the velocity distribution of reactant molecules produced by the Maxwell–Boltzmann distribution at thermal equilibrium, the normal relationship between the temperature-dependent rate constant and the energy cross-section can be calculated as

$$k(T) = \left[\left(\frac{2}{kT}\right)^{3/2}\left(\frac{1}{\mu\pi}\right)^{1/2}\int_0^\infty \frac{E\sigma(E)\exp(E_0-E)}{kT}dE\right]\exp\left(-\frac{E_0}{kT}\right).$$

This equation can be easily obtained by calculating the activation energy and frequency factor.

The determination of the reaction rate and activation energy through this theoretical approach is supported by the molecular simulation method, which can also identify the precise reaction pathway and feasibility through this knowledge. Furthermore, it can reveal the driving force of the chemical phenomena. Numerous previous studies have attempted to use molecular simulations to comprehend the chemical reaction and improve the performance of catalysts or materials in many renewable energy-related and environmental research fields.[16–21]
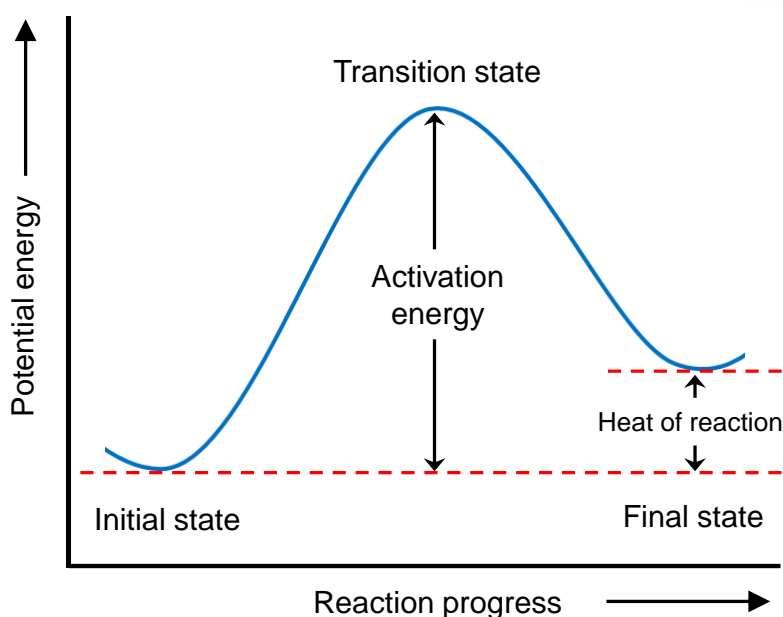
Figure 1.5. Schematic of the reaction coordinate diagram.

1.2.1 Mechanistic study on effective biomass conversion

Biomass produced from plants is a renewable hydrocarbon energy source. Lignocellulose is the most abundant biomass resource and is composed of cellulose, hemicellulose, and lignin (**Figure 1.6**).[22–24] However, lignocellulose is extremely challenging to use because of its complexity and a lack of efficient technologies. Recently, molecular simulations have been used to investigate the reaction mechanisms for converting lignocellulose to high-value chemicals such as aromatic compounds, bioplastic precursors, and liquid fuels using heterogeneous catalysts (**Figure 1.7**).
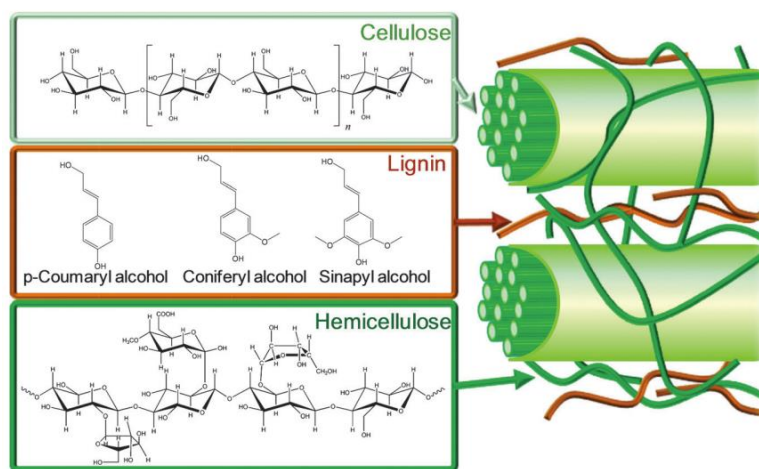
Figure 1.6. Structure of lignocellulosic biomass comprising cellulose, hemicellulose, and lignin. Reproduced with permission from ref. 22. Copyright 2012 Royal Society of Chemistry.

In these studies, many heterogeneous catalysts were used to improve the biomass conversion process by reducing the activation energy. It was easy to use molecular simulations to identify the RDS and to evaluate the performance of the heterogeneous catalysts. Additionally, the potential for advances in catalysts has been demonstrated by explaining the relationship between the performance and electronic properties of catalysts.
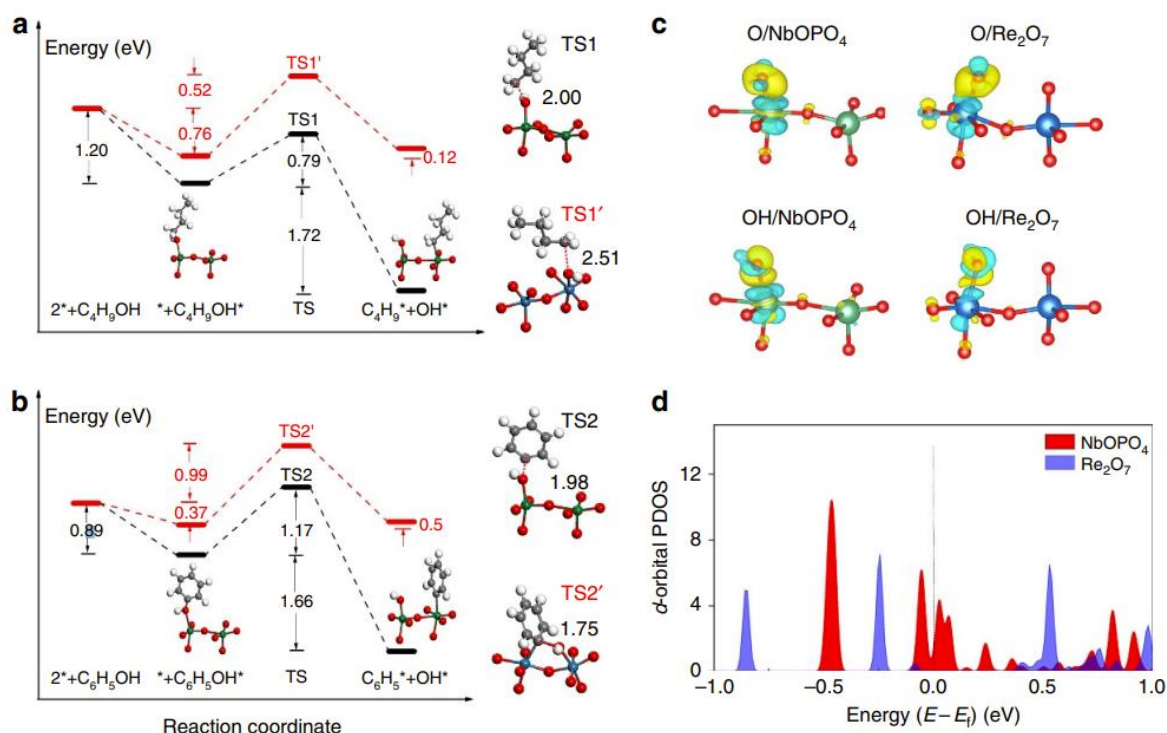
Figure 1.7. Calculated results of computational studies. Calculated energy profiles of the C–O bond cleavage of (a) C_4H_9OH and (b) C_6H_5OH. The black and red lines indicate $NbOPO_4(100)$ and $Re_2O_7(010)$, respectively. The structures of the initial and final states on $NbOPO_4(100)$ are shown, whereas the transition states involving the C–O bond cleavage of C_4H_9OH and C_6H_5OH are represented as TS1, TS10, TS2, and TS20, with the elongated C–O bond lengths shown. The emerald, dark blue, white, gray, and red balls represent the Nb, Re, H, C, and O atoms, respectively. (c) Iso-surfaces of the charge density difference for O and OH adsorption on the $NbOPO_4(100)$ and $Re_2O_7(010)$ surfaces. For clarity, only the local active sites are shown. The yellow regions indicate charge accumulation, and the light blue regions indicate charge depletion. The emerald, dark blue, white, and red balls represent the Nb, Re, H, and O atoms, respectively. (d) The *d*-orbital projected density of states for the surface Nb_{5c} and Re_{5c} atoms, demonstrating their relative energies, which are aligned to the Fermi level (E_F). Reproduced with permission from ref. 24. Copyright 2016 Springer Nature.

1.2.2 Mechanistic study on effective rechargeable lithium-ion batteries

Renewable energy sources such as solar and wind energies are receiving significant attention because they can help prevent the emission of CO_2 and air pollutants in the atmosphere, but their inconsistent and discontinuous energy availability makes it difficult for them to compete with fossil fuels. Therefore, the use of renewable energy sources requires an efficient energy storage method. The lithium-ion battery (LIB) industry is currently making efforts to develop sustainable energy storage systems (**Figure 1.8**).[25–27] LIBs are a type of rechargeable battery that uses the reversible reduction of lithium ions to store energy as a key component of its electrochemistry.
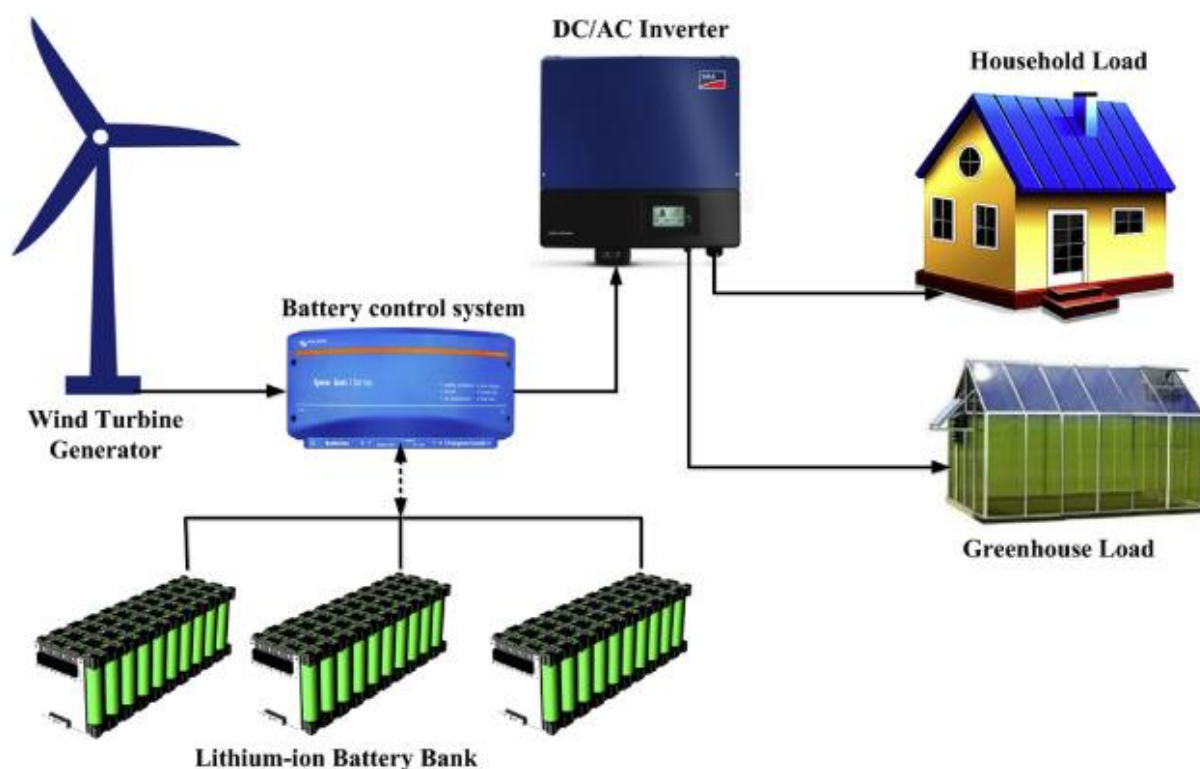
Figure 1.8. Schematic representation of the relationship between LIBs and renewable energy. Reproduced with permission from ref. 25. Copyright 2018 Elsevier Ltd.

However, LIBs have scientific issues, such as battery performance degradation and safety concerns.[28,29] To solve these issues, many previous studies have been recently conducted to explore new materials to use as electrodes or electrolytes for LIBs in order to maintain performance while increasing energy density. In particular, molecular simulations have been used to easily propose new high-performance battery materials based on theoretical knowledge (**Figures 1.9** and **1.10**).[30–36] These theoretical

principles and reaction mechanisms in LIB systems may provide insights into the future development of advanced renewable energy storage technologies for batteries.
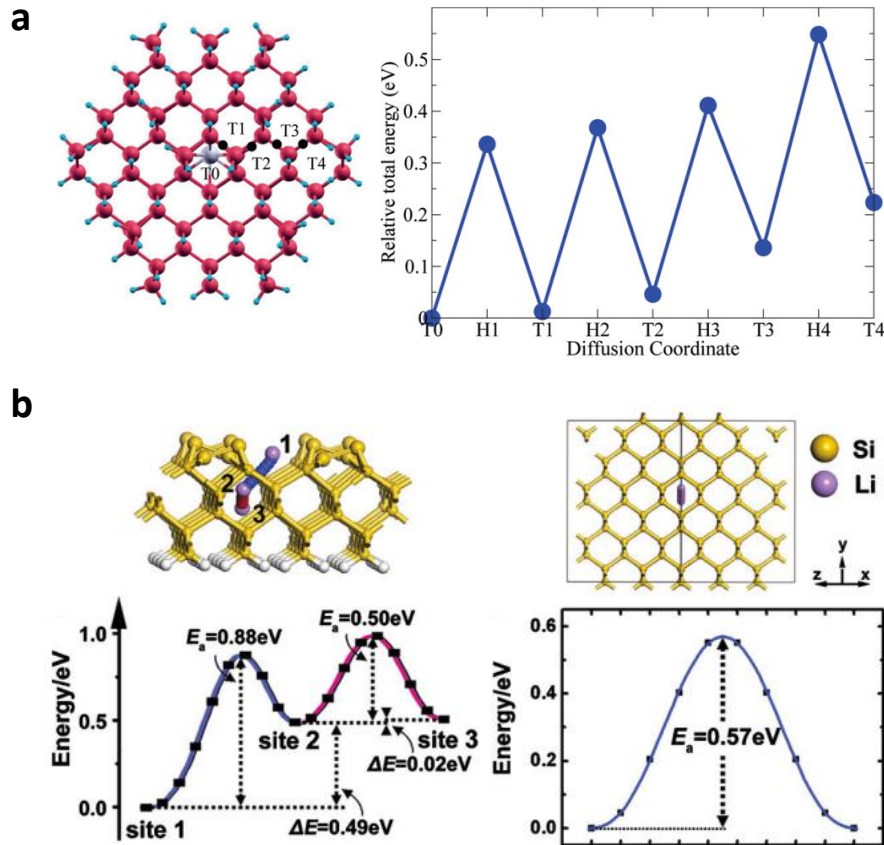
Figure 1.9. (a) Changes in the total energy when Li diffuses from the center tetrahedral site of a $Si_{210} H_{136}$ nanocrystal with a diameter of 22 Å to the surface. T0–T4 indicate the different tetrahedral positions. The black dots in the left figure indicate the hexagonal sites, which are saddle points of the diffusion pathway from T0 to T4. Reproduced with permission from ref. 30. Copyright 2010 American Chemical Society. (b) Li transport path through the Si(100) thin film and the corresponding energy profile. Li transport in a $3 \times 3 \times 3$ Si supercell (216 Si atoms) and the corresponding transport barrier. Reproduced with permission from ref. 31. Copyright 2010 American Institute of Physics.
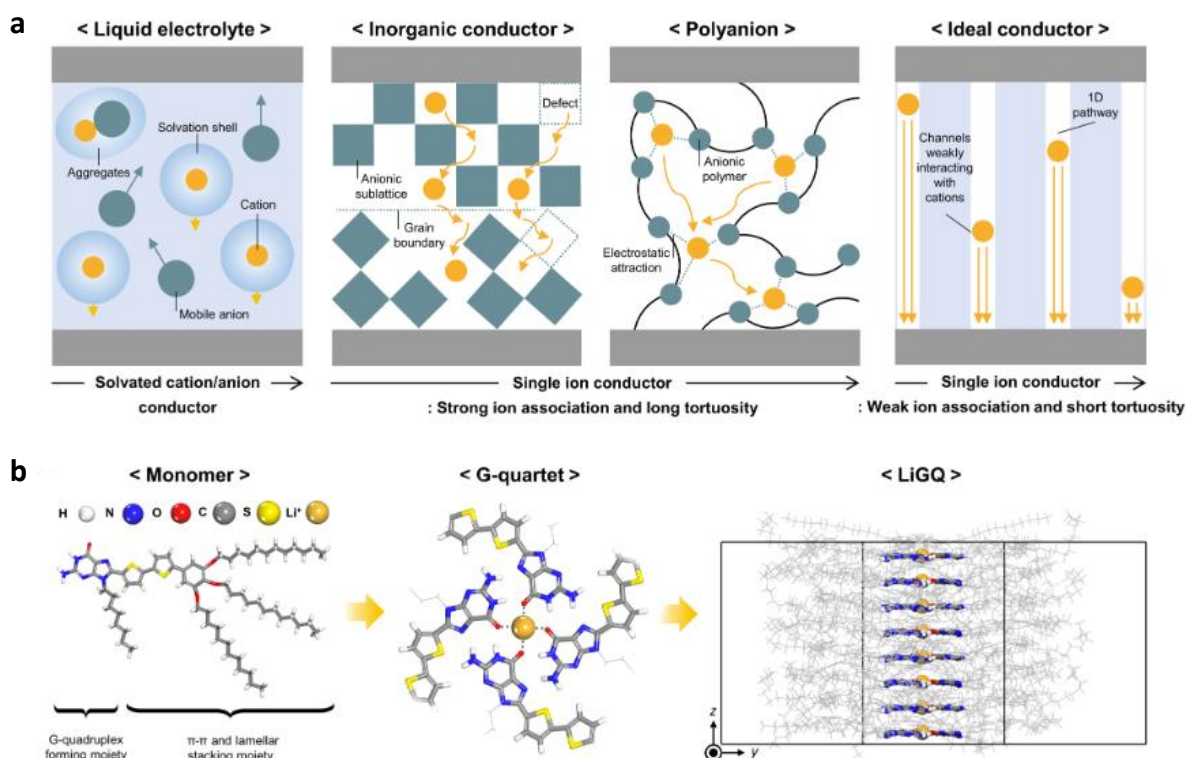
Figure 1.10 (a) Schematic comparison of ion transport phenomena in various ion conductors: traditional conductors versus ideal conductors. (b) Theoretically simulated chemical structure of a single-strand Li^+-centered G-quadruplex and its self-assembly procedure. The dotted line represents the ion–dipole interaction between Li^+ and the G-quartet. The close stacking of the G-quartets in the vertical direction results in the formation of one-dimensional central channels that allow straightforward Li^+ conduction pathways in the Li^+-centered G-quadruplex. To represent the Li^+-centered G-quadruplex clearly, its hydrocarbons and bithiophenes are blurred. Reproduced with permission from ref. 36. Copyright 2022 American Association for the Advancement of Science.

1.2.3 Mechanistic study on the effective mineral trapping of CO₂

The mineral trapping of CO_2 (or mineral carbonation) is an effective method for capturing and storing CO_2 (**Figure 1.11**). It is advantageous for immobilizing CO_2 because it stably prevents CO_2 from leaking into the atmosphere for a long period, making it possible to recycle stored CO_2 as a renewable energy source. The in situ mineral carbonation method involves the direct injection of CO_2 into geologic reservoirs without transporting or further processing the host rocks.[37] Under the injection condition, CO_2 is in a supercritical state ($scCO_2$) that contains some portion of dissolved water, and it finally reacts

with divalent metal cations to form insoluble carbonate minerals, such as calcite ($CaCO_3$), magnesite ($MgCO_3$), dolomite ($Ca_{0.5}Mg_{0.5}CO_3$), and siderite ($FeCO_3$). In this context, obtaining sufficient divalent metal cations from an appropriate source is essential for facilitating the increase in carbonate minerals.
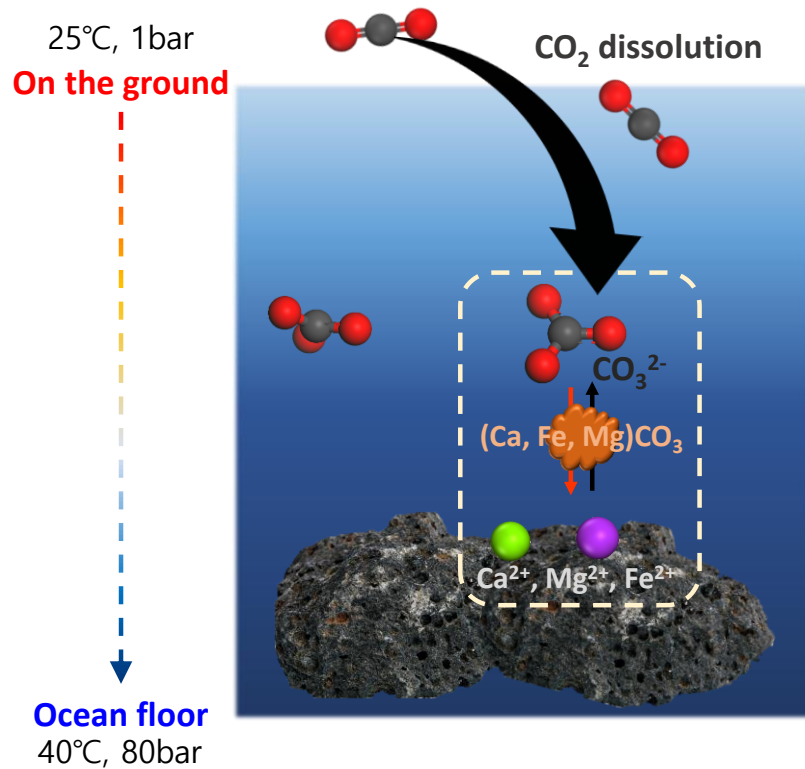
Figure 1.11. Schematic illustration of the mineral trapping of CO_2 on the ocean floor.

Although there is currently limited availability of such a carbon storage method due to the lack of efficient technologies, several molecular simulation studies have partially provided insights into the mineral carbonation reaction and used theoretical approaches to explore solutions to expedite the reaction. Considering that the dissolution of metal cations from the surface of silicate minerals has been found to be the rate-limiting step in the mineralization reaction with wet $scCO_2$,[38] the adsorption characteristics of water and CO_2 molecules on the mineral surface have been addressed.[39] An in-depth understanding of the mineral carbonation reaction mechanism will provide a renewable energy source and a solution to the air pollution problem because it will result in the rapid disposal of CO_2.

1.4 Reference

1. Vaclav Smil (2017). Energy Transitions: Global and National Perspectives 2nd Edition.

2. Herzog, H.; Eliasson, B.; Kaarstad, O. *Scientific American* **2000**, 282, 72−79.

3. Staples, M. D.; Malina, R.; Barrett, S .R. H. *Nature Energy*, **2017**, 2, 16202.

4. Rejinders, L.; Hujibregs, M. A. J. *J. Clean. Prod.* **2007**, 15, 1806−1812.

5. Møller, K. T.; Sheppard, D.; Ravnsbæk, D. B.; Buckley, C. E.; Akiba, E.; Li, H.-W.; Jensen, T. R. *Energies* **2017**, 10, 1645.

6. Lund, H.; Mathiesen, B. V. *Energy* **2009**, 34, 524−531.

7. Lund, H. *Energy* **2007**, 32, 912−919.

8. Pérez-Ortiz, M.; Jiménez-Fernández, S.; Gutiérrez, P.A.; Alexandre, E.; Hervás-Martínez, C.; Salcedo-Sanz, S. *Energies* **2016**, 9, 607.

9. Lai, J.-P.; Chang, Y.-M.; Chen, C.-H.; Pai, P.-F. *Appl. Sci.* **2020**, 10, 5975.

10. Rigo, P.D.; Rediske, G.; Rosa, C.B.; Gastaldo, N.G.; Michels, L.; Neuenfeldt, A.L., Jr.; Siluk, J.C.M. *Sustainability* **2020**, 12, 10195.

11. Degnan, T. F *Curr. Opin. Chem. Eng.* **2015**, 9, 75−82.

12. Nelson, J. P.; Bolin, W. D. *IEEE Trans. Ind. Applicat.*, **1995**, 31, 419–428.

13. Ali, M. F.; Ali, B. E.; Speight, J. G. *Handbook of Industrial Chemistry: Organic Chemicals, McGraw-Hill Education*, New York, **2005**.

14. Centi, G.; Quadrelli, E. A.; Perathoner, S. *Energy Environ. Sci.*, **2013**, 6, 1711–1731.

15. Menzinger, M.; Wolfgang, R. *Angew. Chem. internat. Edit.* **1969**, 8, 438–444.

16. Sangha, A. K.; Petridis, A. L.; Smith, J. C.; Ziebell, A.; Parks, J. M. *Environ. Prog. Sustain. Energy* **2012**, 31, 47−54.

17. Kim, H. Y.; Joo, S. H. *J. Mater. Chem. A* **2020**, 8, 8195−8217.

18. Liu, S.; Yang, H.; Huang, X.; Liu, L.; Cai, W.; Gao, J.; Li, X.; Zhang, T.; Huang, Y.; Li B. *Adv. Funct. Mater.* **2018**, 28, 1800499.

19. Gu, G. H.; Noh, J.; Kim, I.; Jung, Y. *J. Mater. Chem. A* **2019**, 7, 17096−17117.

20. Huang, X.; Cheng, D.; Chen, F.; Zhan, X. *Renew. Energy* **2016**, 96, 490−497.

21. Moses, O. A.; Chen, W.; Adam, M. L.;Wang, Z.; Liu, K.; Shao, J.; Li, Z.; Li, W.; Wang, C.; Zhao, H.; Pang, C. H.; Yin, Z.; Yu, X.; *Materials Reports: Energy* **2021**, 1, 100049.

22. Alonso, D. M.; Wettstein, S. G.; Dumesic, J. A. *Chem. Soc. Rev.* **2012**, 41, 8075−8098.

23. Lin, L.; Han, X.; Han, B.; Yang, S. *Chem. Soc. Rev.* **2021**, 50, 11270−11292.

24. Xia, Q.; Chen, Z.; Shao, Y.; Gong, X.; Wang, H.; Liu, X.; Parker, S. F.; Han, X.; Yang, S.; Wang, Y. *Nat. Commun.* **2016**, 7, 11162.

25. Ghorbanzadeh, M.; Astaneh, M.; Golzar, F. *Energy* **2019**, 166, 1194−1206.

26. Lecce, D. D.; Verrelli, R.; Hassoun, J. *Green Chem.* **2017**, 19, 3442−3467.

27. Diouf, B.; Pode, R. *Renew. Energy* **2015**, 76, 375−380.

28. Chen, Y.; Kang, Y.; Zhao, Y.; Wang, L.; Liu, J.; Li, Y.; Liang, Z.; He, X.; Li, X.; Tavajohi, N.; Li, B. J. Energy Chem. 2021, 59, 83−99.

29. Han, X.; Lu, L.; Zheng, Y.; Feng, X.; Li, Z.; Li, J.; Ouyang, M. *eTransportation* **2019**, 1, 100005.

30. Chan, T.-L.; Chelikowsky, J. R. *Nano Lett*. **2010**, 10, 3, 821−825.

31. Peng, B.; Cheng, F.; Tao, Z.; Chen, J. *J. Chem. Phys.* **2010**, 133, 034701.

32. Dhattarwal, H. S.; Chen, Y.-W.; Kuo, J.-L.; Kashyap, H. K. *J. Phys. Chem. C* **2020**, 124, 50, 27495−27502.

33. Huang, S.-P.; Zhang, J.; Ren, Y.-R.; Chen, W.-K. *Appl. Surf. Sci.* **2021**, 569, 151002.

34. Alfaruqi, M. H.; Kim, S.; Park, S.; Lee, S.; Lee, J.; Hwang, J.-Y.; Sun, Y.-K.; Kim, J. ACS Appl. Mater. Interfaces 2020, 12, 14, 16376−16386.

35. Liu, T.; Jin, Z.; Liu, D.-X.; Du, C.; Wang, L.; Lin, H.; Li, Y. *Sci. Rep.* **2020**, 10, 6897.

36. Cho, S,-K.; Lee, K. M.; Kang, S.-H.; Jeong, K.; Han, S.-P.; Lee, J. E.; Lee, S.; Shin, T. J.; Ryu, J. H.; Yang, C.; Kwak S. K.; Lee S.-Y.; *Sci. Adv.* **2022**, 8, eabp8751.

37. Oelkers, E. H.; Gislason, S. R.; Matter, J. *Elements* **2008**, 4, 333−337.

38. Kwak, J. H. ; Hu, J. Z.; Hoyt, D. W.; Sears, J. A.; Wang, C.; Rosso, K. M.; Felmy, A. R. *J. Phys. Chem. C* **2010**, *114*, 4126−4134.

39. Kerisit, S.; Weare, J. H.; Felmy, A. R. *Geochim. Cosmochim. Acta* **2012**, *84*, 137−151.

40. Jensen, F. *Introduction to Computational Chemistry*, John Wiley & Sons Ltd, England, 2nd edition, **2007**.

41. Sholl, D. S.; Steckel, J. A. *Density Functional Theory: A Practical Introduction*, John Wiley & Sons Ltd, Canada, **2009**.

42. Kohn, W.; Sham, L. J. *Phys. Rev.* **1965**, 140, A1133.

43. Lesar, R. *Introduction to Computational Materials Science*, Cambridge University Press, **2013**.

44. van Duin, A. C. T.; Dasgupta, S.; Lorant, F.; Goddard, W. A. *J. Phys. Chem. A* **2001**, 105, 41, 9396−9409.

Chapter 2. Highly Effective and Selective Catalytic System for the Biomass Production

2.1 Highly Efficient Hydrotalcite/1-Butanol Catalytic System for the Production of the High-Yield Fructose Crystal from Glucose

This chapter includes the following contents:

2.1.1 Introduction

Glucose is the most abundant and cheapest hexose sugar available in nature and is also readily available from polysaccharides such as nonedible cellulosic biomass following pretreatment and hydrolysis.[2,3] Recently, the chemical conversion of glucose into high-value chemicals such as furandicarboxylic acid,[4–6] a key monomer for poly(ethylene furanoate), has been extensively studied. 2,5-Dimethylfuran is a promising biofuel because its properties, including the boiling point, high energy density, high research octane number, and immiscibility with water, compare favorably to those of gasoline.[7–9] 5-Hydroxymethylfurfural (HMF) is a key platform chemical for the formation of these important compounds.[10–12]

However, the direct use of glucose as a raw material for HMF is very difficult because glucose is easily transformed into many byproducts, such as anhydroglucose, humin, and levulinic acid, following dehydration, which is favored by its strong cyclic structure.[13–17] In this regard, isomerization of glucose to fructose is a key step for the synthesis of bioplastics and biofuels from glucose, as the synthesis of HMF from fructose is facilitated compared with that from glucose.[9,18–21] Industrially, fructose is produced using immobilized glucose isomerase, which converts extremely concentrated glucose solution to a mixture of about 42% fructose and 50% glucose with some other sugars.[22] However, the operation cost of this current enzymatic process is high as glucose isomerase is expensive, the operation is carried out in buffered solution to maintain pH, and the enzyme is easily deactivated by feed impurities.[23] Therefore, suitable catalytic processes to replace this costly enzymatic process are highly desirable. A number of acidic and basic heterogeneous catalysts, such as zeolites[24–31] and hydrotalcite,[32][−36] have been reported to be active for the catalytic conversion of glucose to fructose.

Among these materials, basic hydrotalcite is the most promising catalyst for industrial application owing to its easy preparation by simple precipitation and its high fructose yield. Hydrotalcite is a layered double hydroxide of general formula $[Mg_{1-x}Al_x(OH)_2]^{x+}$ $(A_{x/n}^{n-})\cdot mH_2O$, where Mg^{2+} ions are partially substituted by Al^{3+} in the brucite-type layers and A^{n-} is an interlayer anion.[37] The catalytic activity of hydrotalcite depends highly on its pretreatment, the initial glucose concentration, and the solvent. Rehydrated hydrotalcite retains abundant weak basic sites through exfoliation of layers, leading to enhanced catalytic performance.[32] As glucose isomerization is an equilibrium reaction that gives a mixture of glucose and fructose, the separation of fructose from glucose is also very important. Commercially, chromatography is widely used for this purpose, but this technique requires expensive equipment and has low productivity and yields.[23,38−40] Alternative processes have been proposed to achieve sugar separation, such as zeolite adsorption,[41] ion exchange membranes,[42,43] and liquid membranes,[44] but these techniques are complex and the associated equipment and operation costs are high. Hence, the development of a more efficient and cost-effective separation process for glucose/ fructose mixtures is also highly desired for commercialization of the catalytic isomerization of glucose into fructose.

Herein, we propose a novel protocol for high-yield production of fructose from a highly concentrated glucose solution (10 wt %) using hydrotalcite as the catalyst in 1- butanol, which is a sustainable solvent than can be produced from a variety of waste biomass sources. We investigated the solvation effect in catalytic isomerization of glucose to fructose and the reaction mechanism of glucose isomerization into fructose on hydrotalcite through density functional theory (DFT) calculation. (**Figure 2.1.1**)Theoretical calculation suggested that the isomerization of glucose was preferred to be bound on the hydrotalcite surface in 1-butanol solvent.
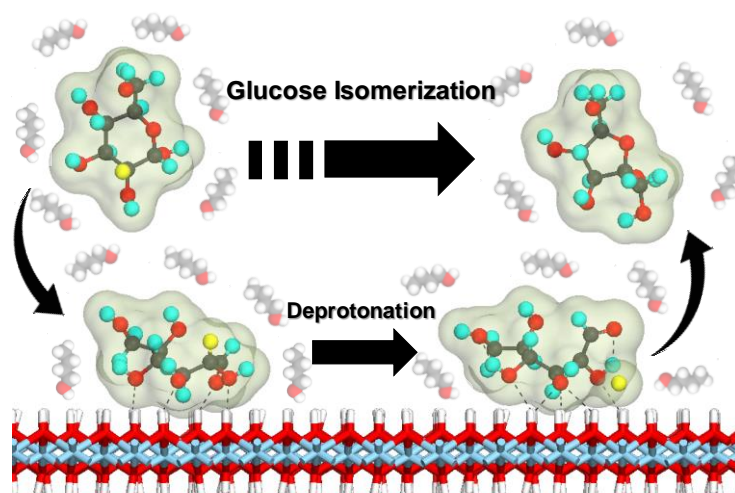
Figure 2.1.1 Schematic mechanism of isomerization from glucose to fructose on hydrotalcite layer.

2.1.2 Computational Models and Methods

All DFT calculations were performed with Dmol[3] program.[45,46] We used Perdew-Burke-Ernzerhof (PBE) exchange correlation functional[47] and DNP 4.4 basis set with the DFT semi-core pseudopotential (DSPP) core treatment was employed to this study. For the dispersion-correction effect, the Tkatchenko-Scheffler scheme[48] was used. The convergence criteria for energy, force, and displacement were set to $1×10-5$ Ha, 0.002 Ha/Å, and 0.005 Å, respectively. The electrostatic contribution of implicit solvent was considered by employing the Conductor-like Screening Model (COSMO) method.[49] The dielectric constants of solvent are water ($\varepsilon = 78.54$), DMF ($\varepsilon = 36.7$), GVL ($\varepsilon = 36.47$), and 1-butanol ($\varepsilon = 17.7$). The solvation energy (ΔE_{solv}) of glucose was calculated as follows,

$$\Delta E_{solv} = E_{sol,0} - E_{vac,0}$$

where $E_{sol,0}$ and $E_{vac,0}$ are the total energy of the geometry-optimized glucose molecule in each solvent environment and in vacuum, respectively. Note that '0' represents the energy-optimized state. The bond dissociation energy (ΔE_{bond}) was calculated as follows,

$$\Delta E_{bond} = -(E_{sol,elong} - E_{sol,0})$$

where $E_{sol,elong}$ is the total energy of glucose molecule when the bond (O…H) in hydroxyl group connected to anomeric carbon of glucose is elongated to 2.5 Å, which can be considered long enough to regard the O-H bond as dissociated. For the catalyst, Mg-Al hydrotalcite (Mg:Al = 2:1) was used with basic $\mu3$-O sites. For the model system, first, we constructed a $3×4×1$ supercell of the 3R structure as introduced in Radha et al's work,[50] and randomly selected 4 Mg atoms from each layer were substituted to Al atoms. To consider the charge balance and basic sites made from experimental procedure,[51] hydrogen atoms were removed to make μ_3-O sites from single hydrotalcite layer (herein 8 H atoms). For the slab model, vacuum region (~15 Å) along the (001) direction was introduced. Note that in order to avoid the self-interaction of the adsorbed glucose, the slab system was extended twice in the direction of (100). To account for the random distribution of basic sites on the surface and binding effect with and without basic site, we constructed two surface models, *i.e.*, one is the model, where each 4 H atoms were removed from both faces, and the other is the model, where all H atoms were removed from downward face. (**Figure 2.1.2**)

The binding energy between glucose and hydrotalcite ($\Delta E_{B.E.}$) was calculated as follows,

$$\Delta E_{B.E.} = E_{glu-surface} - E_{surface} - E_{glu}$$

where $E_{glu-surface}$ is the total energy of glucose-adsorbed hydrotalcite system, and $E_{surface}$, E_{glu} are the

energies of the hydrotalcite system and glucose molecule, respectively. Note that the solvent effect was treated by the COSMO method.
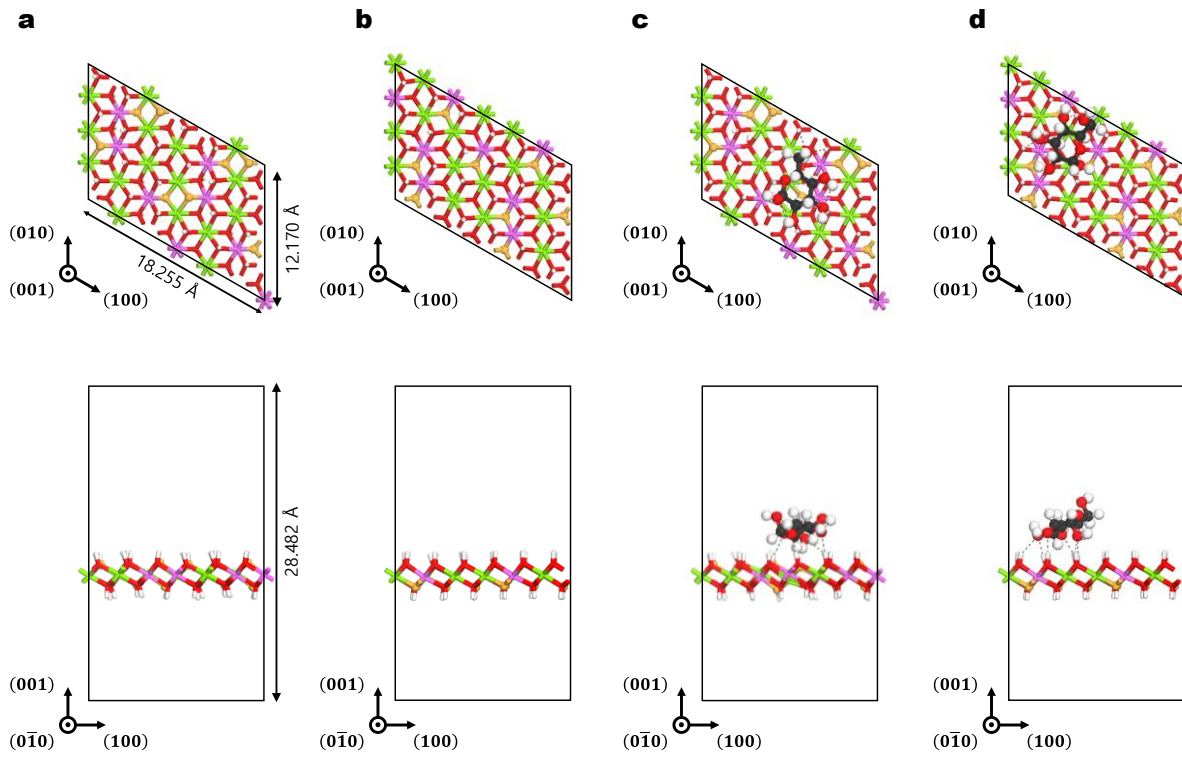
Figure 2.1.2 DFT-optimized structures of hydrotalcite and adsorbed glucose molecule. (a) Top view (top) and front view (bottom) of Mg-Al hydrotalcite system having basic sites at both faces. (b) Top view (top) and front view (bottom) of Mg-Al hydrotalcite system having basic sites only at bottom face. (c) Top view (top) and front view (bottom) of the optimized configuration of glucose-adsorbed hydrotalcite at basic site. (d) Top view (top) and front view (bottom) of the optimized configuration of glucose-adsorbed hydrotalcite at non-basic site. For clear view, hydrotalcite is shown in stick model, whereas μ_3-O sites and glucose molecule are shown in ball-and-stick model. Color scheme is as follows; carbon (dark gray), hydrogen (white), μ_3-oxygen (orange), the other oxygen (red), magnesium (green), and aluminum (pink).

2.1.3 Results and Discussion

To theoretically predict the characteristic trends of this base-catalyzed glucose conversion and fructose formation depending on the solvents, we conducted density functional theory (DFT) calculations considering the effect of solvents implicitly around the glucose and hydrotalcite. Considering that proton transfer for the ring opening of glucose was an initiation of the isomerization, to compare the reactivity (or conversion) of glucose with respect to the solvents, we measured solvation energies of the glucose molecule and bond dissociation energy in its hydroxyl group while varying the solvent environment. As shown in **Figure 2.1.3**, as the dielectric constant of the solvent increased (i.e., in the order of 1- butanol, GVL, DMF, water), higher solvation energy (ΔE_{solv}) and lower bond dissociation energy (ΔE_{bond}) were measured. In this regard, a certain preference in the conversion of glucose was expected to be correlated to the solvated state of glucose by each solvent. Subsequently, the proton transfer to open the ring structure occurred accordingly. Based on the results, water was the best environment for glucose conversion. For glucose to react to form fructose, we anticipated that the adsorption of glucose to the hydrotalcite surface should be facilitated for better base-catalyzed dehydrogenation. Among probable configurations searched, the most stable configuration was found through DFT calculation under each solvent environment. To account for the random distribution of basic sites on the surface and binding effect with and without basic sites, average binding energies for these sites were calculated (**Figure 2.1.2**).
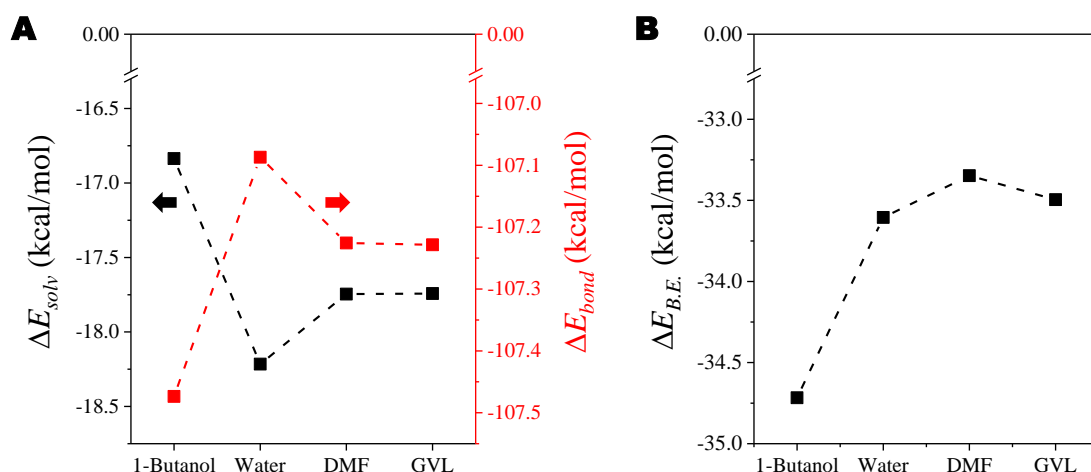
Figure 2.1.3 DFT calculations of the solvation energy of glucose, bond dissociation energy of OH, and the binding energy of glucose on hydrotalcite with respect to the solvents. (a) Solvation (black dashed line) and bond dissociation energy (red dashed line) of glucose at each solvent and (b) binding energies of the glucose molecule on the hydrotalcite surface with respect to solvents.

Regardless of solvents, adsorbed configurations of glucose were similar to each other. When interacting with a basic site, five OH groups of glucose formed hydrogen bonds with hydrotalcite, whereas four OH groups interacted with the surface without basic sites. Here, the binding energy ($\Delta E_{B.E.}$) of the glucose molecule on the hydrotalcite surface in 1-butanol (-34.7 kcal/mol) was larger than other solvents (-33.3 to -33.6 kcal/mol) (**Figure 2.1.3B**), which implied that glucose was thermodynamically favored to be bound on the surface.

The initiation of base-catalyzed isomerization reaction is known to be abstraction of H atom from C2 carbon. However, we noted that ring opening in the solvent phase should be preceded for the deprotonation reaction of C2 carbon over the basic hydrotalcite surface. That is reason why we mentioned as quoted "Considering that proton transfer in glucose was an initiation of the isomerization" in the main text. To validate our assumption, reaction mechanisms of ring opening depending on the solvent were calculated (**Figure 2.1.4**) and compared with following deprotonation reaction (**Figure 2.1.5**).
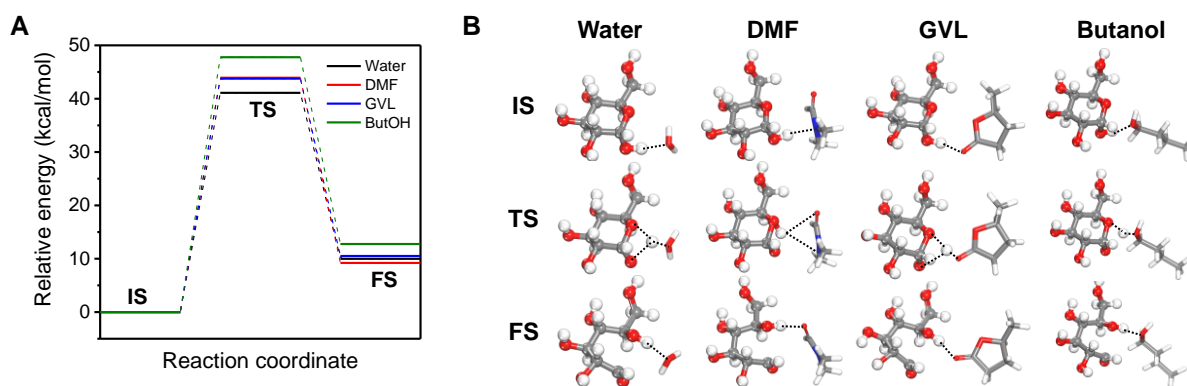
Figure 2.1.4 Reaction mechanism of glucose ring opening on each solvent. (a) Energy profile and (b) configurations of ring opening mechanism. 'IS', 'TS', and 'FS' are abbreviations of 'Initial State', 'Transition State', and 'Final State'. Black dotted lines in (b) represent closely interacting atoms in the reaction. Glucose and solvent molecules are shown by ball-and-stick and stick models, respectively. Color scheme is as follows; carbon (gray), hydrogen (white), oxygen (red), and nitrogen (blue).

In the ring opening mechanism, one additional explicit solvent was added near the glucose molecule as well as applying COSMO (i.e., implicit solvent) method. As similar to the bond dissociation energy result (Figure 2.1.3A) in the manuscript, the ring opening under water solvent showed the lowest activation energy (41.098 kcal/mol), and higher activation energies were required in the order of GVL (43.753 kcal/mol), DMF (43.937 kcal/mol) and butanol (47.778 kcal/mol) solvent. Further, the

isomerization reaction mechanism as well as H abstraction from C2 carbon was studied over the basic hydrotalcite surface depending on the solvent (Figure 2.1.5).
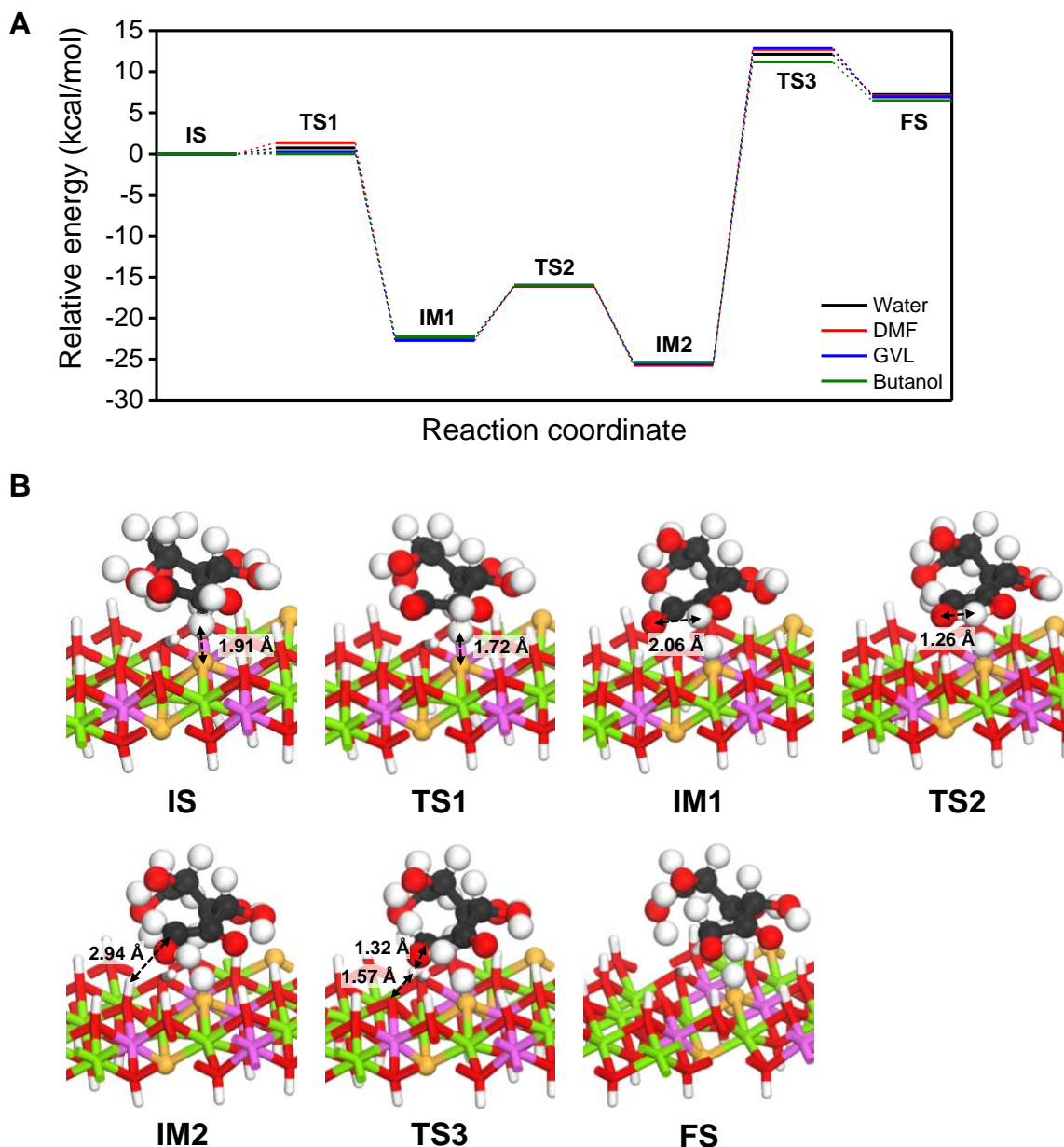
Figure 2.1.5 Reaction mechanism of the isomerization of ring-opened glucose on basic hydrotalcite. (a) Energy profile and (b) configurations of ring opening mechanism. 'IS', 'TS', and 'FS' are abbreviations of 'Initial State', 'Transition State', and 'Final State'. Small letters in (b) represents the distance (in Å unit) between reacting atoms. For clear view, hydrotalcite is shown in stick model, whereas μ_3-O sites and glucose molecule are shown in ball-and-stick model. Color scheme is as follows; carbon (dark gray), hydrogen (white), μ_3-oxygen (orange), the other oxygen (red), magnesium (green), and aluminum (pink).

From IS to IM1, H atom was almost spontaneously detached from C2 carbon of ring-opened glucose, accompanying marginal amount of activation energy (E_a = 0.03 to 1.33 kcal/mol) and large heat of reaction (ΔE = -22.25 to -22.72 kcal/mol), due to the strong basicity of hydrotalcite surface. In this respect, the ring opening reaction should occur for the isomerization reaction to proceed, resulting in a consistent trend with experimental conversion. Also, following reactions were regarded as hydride shift from IM1 to IM2 and protonation reactions from IM2 to FS. In the hydride shift reaction, it required relatively low E_a (6.17 to 6.67 kcal/mol) and ΔE (-3.13 to -3.19 kcal/mol) for all solvents. The rate-determining step was the final protonation reaction from hydrotalcite surface to glucose molecule. In this reaction, butanol environment made the lowest E_a (36.61 kcal/mol). For the other solvents, higher E_a's were required in the order of water (37.57 kcal/mol), DMF (38.45 kcal/mol), and GVL (38.49 kcal/mol). Thus, we conclude that solvent conditions affected on the Ea of RDS, which contributed to the largest fructose yield under butanol solvent in experiment.

2.1.4 Conclusion

In this work, we developed a promising protocol for the production of fructose crystal from glucose-containing biomass using only heterogeneous catalysis for the first time. Through the solvation energy and the initial bond dissociation energy of glucose with each solvent using DFT calculation, we identified that the effect of 1-butanol solvent served as an important factor in the glucose isomerization reaction. Furthermore, we investigated the reaction mechanism of glucose isomerization on the hydrotalcite, and the low activation energy of this reaction showed that isomerization from fructose to glucose is possible. By this protocol, this process for fructose production is simple, inexpensive, and green when compared with current industrial procedures that rely on enzymatic isomerization reactions.

2.1.5 References

1. Upare, P. P.; Chamas, A.; Lee, J. H.; Kim, J. C.; Kwak, S. K.; Hwang, Y. K.; Hwang, D. W. *ACS Catalysis* **2020**, 10(2), 1388–1396.

2. To, A. T.; Chung, P. W.; Katz, A. *Angew. Chem., Int Ed.* **2015**, 54, 11050−11053.

3. Pal, R. K.; Chakraborty, S. *Bioresour. Technol.* **2013**, 148, 611−614.

4. Zhang, J.; Li, J.; Tang, Y.; Lin, L.; Long, M. *Carbohydr. Polym.* **2015**, 130, 420−428.

5. Casanova, O.; Iborra, S.; Corma, A. *ChemSusChem* **2009**, 2, 1138−1144.

6. Pan, T.; Deng, J.; Xu, Q.; Zuo, Y.; Guo, Q. X.; Fu, Y. *ChemSusChem* **2013**, 6, 47−50.

7. Saha, B.; Abu-Omar, M. M. *ChemSusChem* **2015**, 8, 1133−1142.

8. Roman-Leshkov, Y.; Barrett, C. J.; Liu, Z. Y.; Dumesic, J. A. *Nature* **2007**, 447, 982−985.

9. Upare, P. P.; Hwang, D. W.; Hwang, Y. K.; Lee, U.-H.; Hong, D.-Y.; Chang, J.-S. *Green Chem.* **2015**, 17, 3310−3313.

10. 1Li, C.; Zhao, Z. K.; Wang, A.; Zheng, M.; Zhang, T. *Carbohydr. Res.* **2010**, 345, 1846−1850.

11. Zhao, H.; Holladay, J. E.; Brown, H.; Zhang, Z. C. *Science* **2007**, 316, 1597−600.

12. Simeonov, S. P.; Coelho, J. A.; Afonso, C. A. *ChemSusChem* **2013**, 6, 997−1000.

13. Ohara, M.; Takagaki, A.; Nishimura, S.; Ebitani, K. *Appl. Catal. A* **2010**, 383, 149−155.

14. Hoang, T. M.; Lefferts, L.; Seshan, K. *ChemSusChem* **2013**, 6, 1651−1658.

15. Pileidis, F. D.; Titirici, M. M. *ChemSusChem* **2016**, 9, 562−582.

16. Jeong, G. T.; Ra, C. H.; Hong, Y. K.; Kim, J. K.; Kong, I. S.; Kim, S. K.; Park, D. H. *Bioprocess Biosyst. Eng.* **2015**, 38, 207−217.

17. Ren, H.; Zhou, Y.; Liu, L. *Bioresour. Technol.* **2013**, 129, 616−619.

18. Amarasekara, A. S.; Williams, L. D.; Ebede, C. C. *Carbohydr. Res.* **2008**, 343, 3021−3024.

19. Tong, X.; Li, Y. *ChemSusChem* **2010**, 3, 350−355.

20. Liu, F.; Barrault, J.; Vigier, K. O.; Jerome, F. *ChemSusChem* **2012**, 5, 1223−1126.

21. Li, H.; Yang, S.; Saravanamurugan, S.; Riisag, A. *ACS Catal.* **2017**, 7, 3010−3029.

22. Sproull, R. D.; Lim, H. C.; Schneider, D. R. *Biotechnol. Bioeng.* **1976**, 18, 633−648.

23. Zhang, Y.; Hidajat, K.; Ray, A. K. *Biochem. Eng. J.* **2004**, 21, 111−121.

24. Saravanamurugan, S.; Paniagua, M.; Melero, J. A.; Riisager, A. *J. Am. Chem. Soc.* **2013**, 135, 5246−5249.

25. Bermejo-Deval, R.; Assary, R. S.; Nikolla, E.; Molinera, M.; Roman-Leshkov, Y.; Hwang, S.-J.; Palsdottira, A.; Silvermana, D.; Lobog, R. F.; Curtiss, L. A.; Davis, M. E. *Proc. Natl. Acad. Sci. U.S.A.* **2012**, 109, 9727−9732.

26. Bermejo-Deval, R.; Gounder, R.; Davis, M. E. *ACS Catal.* **2012**, 2, 2705−2713.

27. Dijkmans, J.; Gabriels, D.; Dusselier, M.; Clippel, F. D.; Vanelderen, P.; Houthoofd, K.;

Malfliet, A.; Pontikes, Y.; Sels, B. F. *Green Chem.* **2013**, 15, 2777−2785.

28. Yang, G.; Pidko, E. A.; Hensen, E. J. *ChemSusChem* **2013**, 6, 1688−1696.

29. Ren, L.; Guo, Q.; Kumar, P.; Orazov, M.; Xu, D.; Alhassan, S. M.; Mkhoyan, K. A.; Davis, M. E.; Tsapatsis, M. *Angew. Chem., Int. Ed.* **2015**, 54, 10848−10851.

30. Moreau, C.; Durand, R.; Roux, A.; Tichit, D. *Appl. Catal. A* **2000**, 193, 257−264.

31. de Mello, M. D.; Tsapatsis, M. *ChemCatChem* **2018**, 10, 2417−2423.

32. Yu, S.; Kim, E.; Park, S.; Song, I. K.; Jung, J. C. *Catal. Commun.* **2012**, 29, 63−67.

33. Yabushita, M.; Shibayama, N.; Nakajima, K.; Fukuoka, K. *ACS Catal.* **2019**, 9, 2101−2109.

34. Delidovich, I.; Palkovits, R. *Catal. Sci. Technol.* **2014**, 4, 4322−4329.

35. Lee, G.; Jeong, Y.; Takagaki, A.; Jung, J. C. *J. Mol. Catal. A: Chem.* **2014**, 393, 289−295.

36. Delidovich, I.; Palkovits, R. *J. Catal.* **2015**, 327, 1−9.

37. Cavani, F.; Trifiro, F.; Vaccari, A. *Catal. Today* **1991**, 11, 173−302.

38. Hashimoto, K.; Adachi, S.; Noujima, H.; Ueda, Y. *Biotechnol. Bioeng.* **1983**, 25, 2371−2393.

39. Reich, W. S. *Biochem. J.* **1939**, 33, 1000−1004.

40. Beste, Y. A.; Lisso, M.; Wozny, G.; Arlt, W. *J. Chromatogr. A* **2000**, 868, 169−188.

41. Cheng, Y. L.; Lee, T. Y. *Biotechnol. Bioeng.* **1992**, 40, 498−504.

42. Luz, D. A.; Rodrigues, A. K.; Silva, F. R.; Torres, A. E.; Cavalcante, C. L.; Brito, E. S.; Azevedo, D. C. S. *Bioresour. Technol.* **2008**, 99, 2455−2465.

43. Morthensen, S. T.; Sigurdardottir, S. B.; Meyer, A. S.; Jorgensen, H.; Pinelo, M. *J. Membr. Sci.* **2017**, 523, 327−335.

44. Di Luccio, M.; Smith, B. D.; Kida, T.; Borges, C. P.; Alves, T. L. M. *J. Membr. Sci.* **2000**, 174, 217−224.

45. Delley, B. *J. Chem. Phys.* **1990**, 92, 508-517.

46. Delley, B. *J. Chem. Phys.* **2000**, 113, 7756-7764.

47. Perdew, J.P.; Burke, K.; Ernzerhof, M. *Phys. Rev. Lett.* **1996**, 77, 3865-3868.

48. Tkatchenko, A.; Scheffler, M. *Phys. Rev. Lett.* **2009**, 102, 073005.

49. Klamt, A.; Schüürmann, G. *J. Chem. Soc., Perkin Trans. 2*, **1993**, 5, 799-805.

50. Radha, A.V.; Kamatha, P.V.; Shivakumara, C. *Acta Cryst. B* **2007**, 63, 243-250.

51. Lari, G. M.; de Moura, A. B. L.; Weimann, L.; Mitchell, S.; Mondelli, C.; Pérez-Ramírez, J. *J. Mater. Chem. A,* **2017**, 5, 16200-16211.

2.2 A Robust and Highly Selective Catalytic System of Copper–Silica Nanocomposite and 1-Butanol in Fructose Hydrogenation to Mannitol

This chapter includes the following contents:

2.2.1 Introduction

Biomass, a renewable carbon source, offers great potential among the available alternative resources for the production of valuable chemicals and liquid fuels. In particular, carbohydrates are the most abundant biomass and great attention has been paid to chemical conversion into valuable chemicals and fuels.[2] Mannitol is a kind of polyol which is mostly used as low calorie sweetener in diabetic food and in chewing gums as it is poorly absorbed from the intestines.[3] It is also widely used in pharmaceutical, cosmetic, surfactants and coating industries.[4] The global mannitol market size was valued at USD 209 million in 2015 and it is expected to reach USD 418 million by 2024.[5]

Mannitol is naturally occurring sugar and it can be extracted form vegetables, fruits, manna, seaweed, and algae. However, the extraction of mannitol from these plants is not economical.[6] Currently, most of mannitol (around 50000 tons per year) are produced by the catalytic hydrogenation of fructose, which is more abundant hexose in nature.[7] Nickel-based catalysts such as Raney Ni are one of the most common catalysts used for the aqueous phase hydrogenation of fructose.[8] However, nickel-based catalysts gives mannitol yield of around 50% with a significant amount of sorbitol, an isomer of mannitol. Some noble metal catalysts such as Ru and Pt were reported to be more active than nickel-based catalysts, but these catalysts are expensive and the selectivity to mannitol is still limited to around 50%.[9] In terms of mannitol selectivity, Cu-based catalysts are more desirable than the noble and nickel-based catalysts, although the catalytic activities were a little lower.[10] Recently, Zelin et al. investigated various types of Cu-based catalysts for fructose hydrogenation in ethanol/water (70:30) mixture as solvent.[10b] They found that the metallic Cu nanoparticles dispersed on the surface of SiO2 as a neutral support was the most active and selective catalyst, which gave fructose conversion of 98% with mannitol selectivity of 78% after 6 h at 100°C and 40 bar from the initial fructose concentration of 1 wt%. However, the catalyst stability such as Cu leaching during the liquid-phase reaction is of concern.

Recently, we have developed a copper-silica nanocomposite catalyst, which were very active, selective, and robust for hydrogenation of biomass derived carboxylic acid (C4–C6) and their esters into desired products in vapor phase conditions.[11] We have also found that 1-butanol was very effective solvent in terms of product selectivity as well as catalyst stability in liquidphase dehydration of fructose over Amberlyst-15 catalyst and hydrogenation of 5-hydroxymethyl furfural (HMF) over coppersilica nanocomposite and ruthenium-tin/zinc oxide catalyst.[12] 1-butanol is also a sustainable solvent that can be produced from a variety of waste biomass sources and it is widely used in production of cosmetics and pharmaceuticals.[13] (**Figure 2.2.1**)
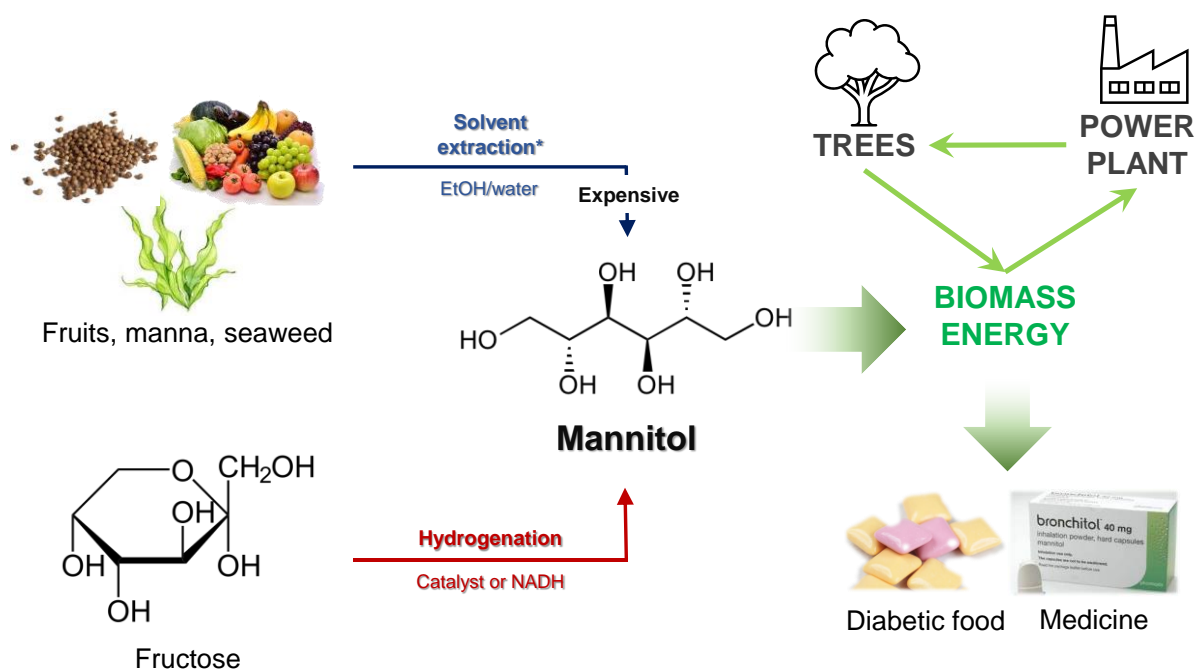
Figure 2.2.1 Schematic images for source and application of mannitol.

To overcome the limitations of the prior art, we herein propose a new process protocol for mannitol production from fructose based on copper-silica nanocomposite catalyst and 1-butanol solvent (**Figure 2.2.2**). This protocol gave an unprecedented mannitol yield of 83% from high fructose concentration of 10 wt% and interestingly, the highly pure mannitol could be recovered from the sorbitol-containing 1-butanol solution by simple filtration from experimental results. (**Figure 2.2.3**) So, we investigated the reaction mechanism of the fructose hydrogenation for understanding high selectivity of mannitol in copper catalyst using the DFT calculation.
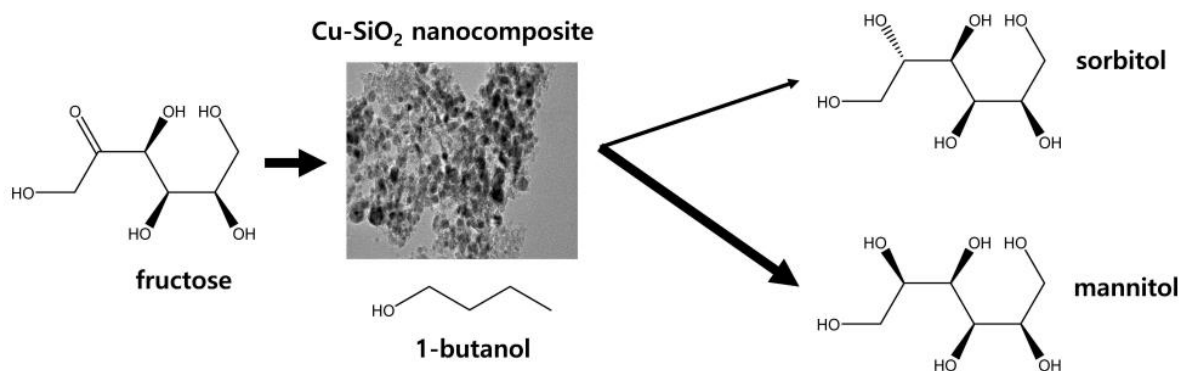
Figure 2.2.2 A reaction scheme of fructose hydrogenation to mannitol over Cu SiO$_2$ nanocomposite in 1-butanol.
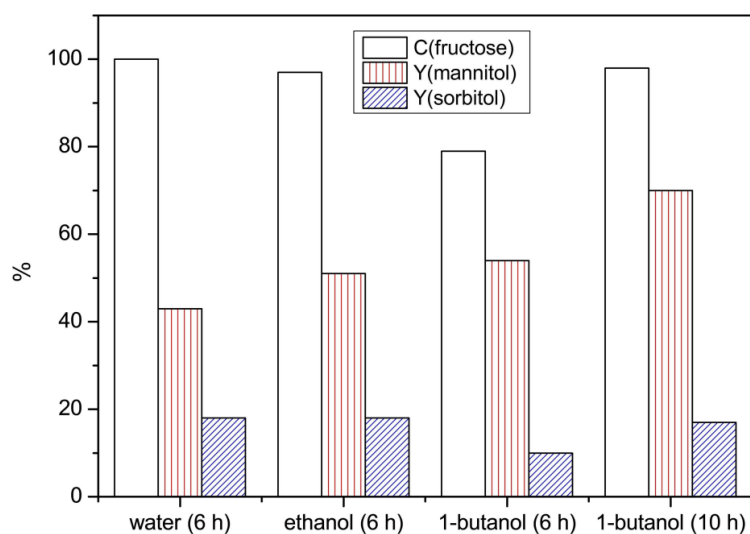
Figure 2.2.3 Catalytic activity of fructose hydrogenation in different solvents. Reaction conditions: Cu(50)-SiO$_2$, 1.0 g; fructose, 5 g; solvent, 45 g; temperature, 120°C; H$_2$ pressure, 25 bar; reaction time, 6 and 10 h. C = conversion, Y = yield.

2.2.2 Computational Models and Methods

To carry out theoretical DFT calculations on the Cu SiO2 catalyst, we employed a slab model consisting of four atomic layers of Cu with (111) surface of the crystal structure (**Figure 2.2.4**). Top two layers of the model system were relaxed while bottom two layers were fixed to represent the bulk phase during the optimization calculation. The vacuum region of slab model was set to about 18 Å for all slab models to avoid self-interaction error. By checking the distances between adsorbed hydrogens, the most stable configuration of adsorbed hydrogen atoms on the surface of copper slab model was found **(Figure 2.2.4b)**.

DFT calculations were conducted with Dmol[3] program.[14] We used Perdew-Burke-Ernzerhof (PBE) exchange-correlation functional[15] and DNP 4.4 basis set with the DFT semi-core pseudopotential (DSPP) core treatment. For the correction of dispersion force, the Tkatchenko–Scheffler scheme was used.[16] The convergence criteria for energy, force, and displacement were set to 1×10 5 Ha, 0.02 Ha nm^{-1}, and 0.0005 nm, respectively. The electrostatic contribution of solvent was described implicitly by employing the conductor-like screening model (COSMO) method[17] with the dielectric constant of 1-butanol (ε=17.7). As well as implicit solvation effect, a butanol molecule was added around the adsorbed fructose molecule for the consideration of explicit interaction with solvent. To calculate transition states in the mechanism of fructose hydrogenation, we employed complete single linear synchronous transit (LST) and quadratic synchronous transit (QST) methods,[18] and the convergence criteria of the root mean square force was set to be 0.02 Ha nm^{-1}.
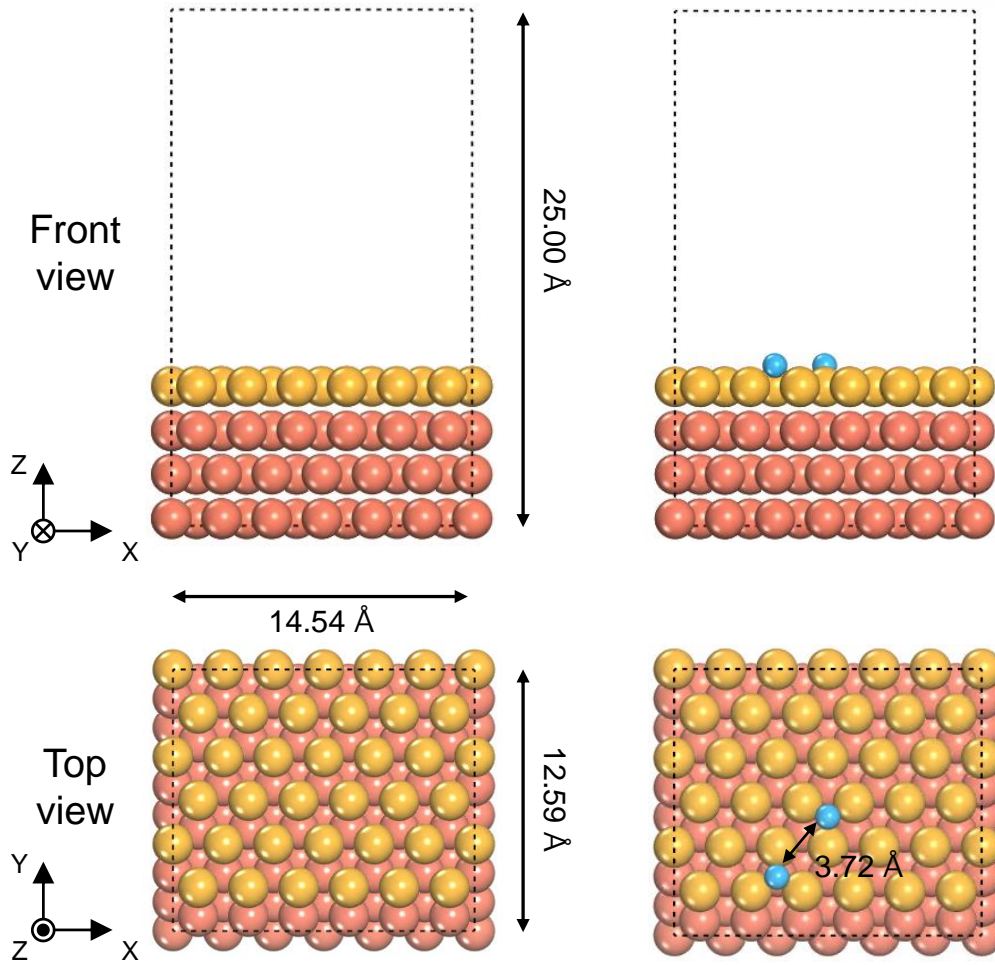
Figure 2.2.4 (a) DFT calculation model for Cu slab with (111) surface. (b) Optimized configuration of hydrogen atoms on the Cu surface. For the clear view, Cu atoms on top layer and the other atoms are colored in orange and reddish brown, respectively. Adsorbed hydrogen atoms are colored in sky blue.

2.2.3 Result and Discussion

To investigate the selective formation of mannitol by hydrogenation of fructose using $Cu-SiO_2$ catalyst, we compared the formation mechanism of mannitol to that of sorbitol under 1-butanol solvent via density functional theory (DFT) calculations. We considered dissociative adsorption of hydrogen molecule on the Cu (111) surface and sought the configuration of adsorbed fructose on the surface. When an adsorbed hydrogen atom is detached and bound to the C=O bond of fructose, the product becomes mannitol or sorbitol by the difference of relative position of hydrogen atoms (**Figure 2.2.5**). Thus, it is important to check the chirality of hydrogenated product, which could be changed depending on the adsorbed orientation of fructose.
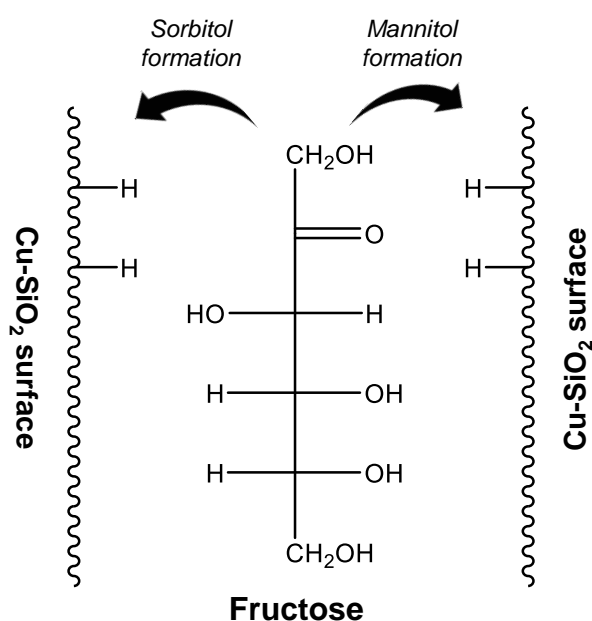
Figure 2.2.5 Orientation dependency of the hydrogenation reaction of adsorbed fructose on the Cu-SiO$_2$ surface.

First, solvent molecule (i. e., 1-butanol) stably interacted through hydrogen bonding with carbonyl group of adsorbed fructose, where the hydrogenation by the adsorbed hydrogen took place (**Figure 2.2.6**). Next, between the copper surface and fructose, three types of interactions were mainly observed, that is, interactions between Cu···HO-C, Cu···H-C, and Cu-H···O=C. For the comparison of the adsorbed configurations, we identified which and how many interactions were included for the atom pairs that closely interacted within 3 Å (**Figure 2.2.7**).
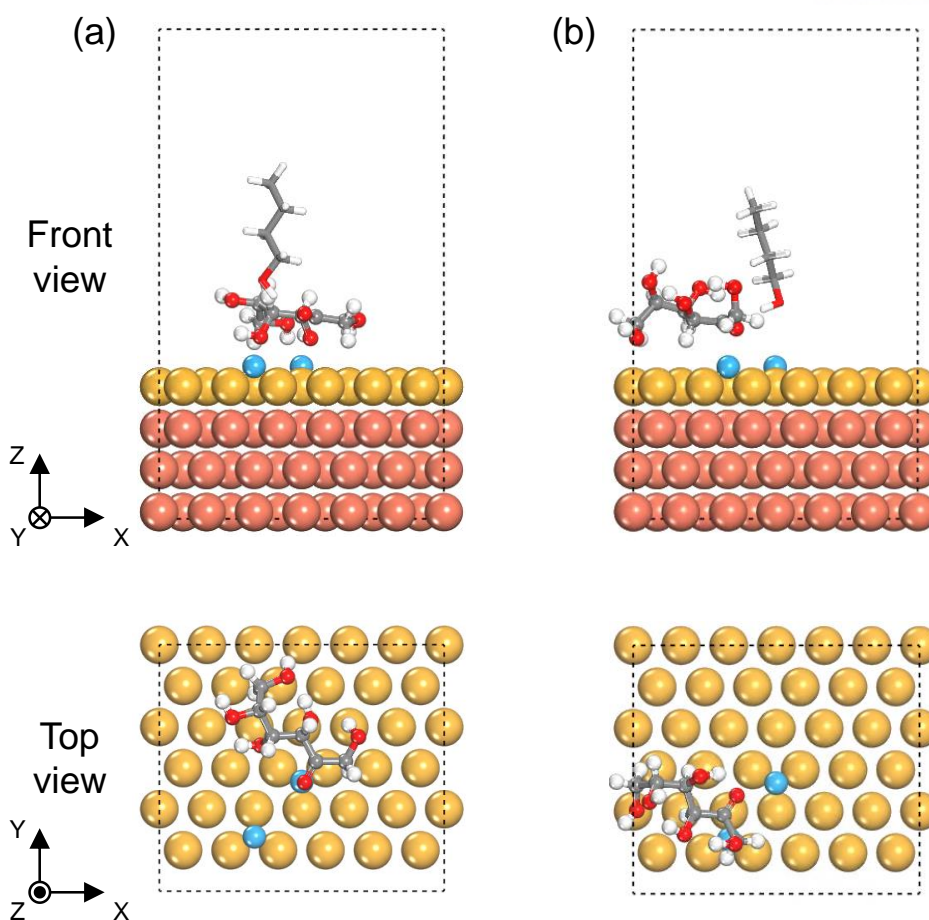
Figure 2.2.6 Optimized configurations of fructose at the (a) $IS_{ad,m}$, and (b) $IS_{ad,s}$ states. Cu slab and adsorbed hydrogen atoms are shown by space-filling model, while the fructose and 1- butanol molecules are shown by ball-and-stick model. Green dotted line represents hydrogen bonding between butanol and carbonyl group of fructose. In the color scheme, Cu atoms in top layer, the other Cu atoms in bottom three layers, and adsorbed hydrogens are colored in orange, reddish brown, and sky blue, respectively. In the fructose and 1-butanol molecules, carbon, hydrogen, and oxygen atoms are colored in gray, white, red, respectively. At the top view, bottom three Cu layers are omitted.

At the adsorbed configuration where the formation of mannitol was preferred ($IS_{ad,m}$), there were four Cu···HO-C, two Cu···H-C, and one Cu-H···O=C interactions, while at the fructose configuration of forming sorbitol ($IS_{ad,s}$), there were one Cu···HO-C, two Cu···H-C, and one Cu-H···O=C interactions. Due to large coulombic interaction energies in Cu···HO C interaction compared to that in Cu···H C interaction, configuration of $IS_{ad,m}$ was thermodynamically favored. Also, in terms of the binding energy ($\Delta E_{B.E.}$), $\Delta E_{B.E.}$ of $IS_{ad,m}$ was 44.18 kcal/mol, whereas $\Delta E_{B.E.}$ of $IS_{ad,s}$ was 34.19 kcal/mol. From this result, selective formation of mannitol was expected to be done by the preferred orientation of adsorbed

fructose on the copper surface.
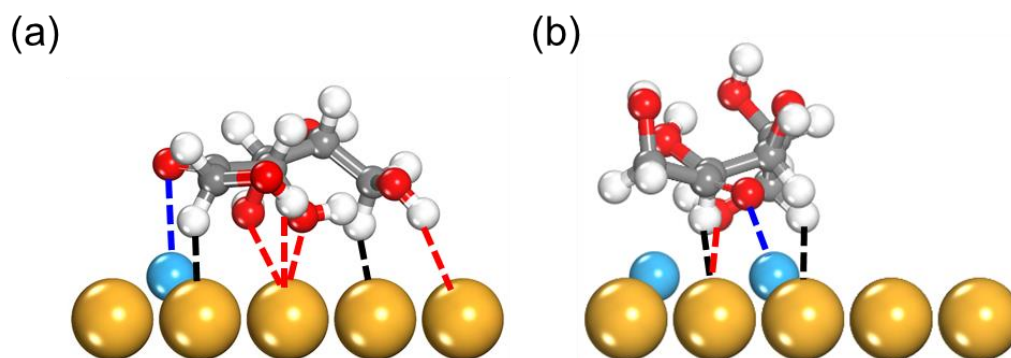
Figure 2.2.7 Magnified view of the optimized configurations of fructose at the (a) $IS_{ad,m}$, and (b) $IS_{ad,s}$ states. In (a) and (b), closely interacting atom pairs and their interaction types are indicated by dashed lines with red for Cu···HO-C, black for Cu···H-C, and blue for Cu-H···O=C interactions, respectively. For the clear view, top layer of Cu surface and adsorbed hydrogen are shown by space-filling model, while the fructose molecule is shown by ball-and-stick model. Cu and adsorbed H atoms are colored in orange and sky blue, respectively. For fructose molecules, carbon, hydrogen, and oxygen atoms are colored in gray, white, and red, respectively.

We further investigated the selective formation by tracking hydrogenation mechanisms for the formations of mannitol and sorbitol on Cu surface, respectively (**Figures 2.2.8** and **2.2.9**). By considering the previous mechanistic study on the hydrogenation of fructose,[19] a hydrogen atom adsorbed on the copper surface was transferred to the carbon of the C=O bond in fructose at the first step (i. e., from IS to IM). The activation energy (E_a) and heat of reaction (ΔE) for the first hydrogen transfer in mannitol formation were estimated to be 7.89 and 6.36 kcal/mol, respectively, while in the sorbitol formation reaction, the energies of 10.39 and 7.20 kcal/mol were required for E_a and ΔE, respectively. After the hydrogen transfer step, at the IM to FS step, another hydrogen atom was attached to the oxygen in C(H)-O⁻ of intermediate structure. In this reaction step, each reaction route for mannitol and sorbitol formation required marginal amount of E_a and exhibited large exothermic heat of ΔE (i. e., E_a and ΔE for mannitol pathway were 5.47 and 30.29 kcal/mol, respectively, and 3.24 and 25.97 kcal/mol for sorbitol pathway, respectively). Thus, comparing the $\Delta E_{B.E.}$, E_a and ΔE obtained from theoretical calculations, in addition to the stable initial structure of adsorbed fructose at $IS_{ad,m}$, mannitol pathway was more thermodynamically favorable than sorbitol pathway. Theoretically, mannitol was expected to be formed selectively on the Cu-SiO$_2$ catalyst, which was consistent with experimental observation.
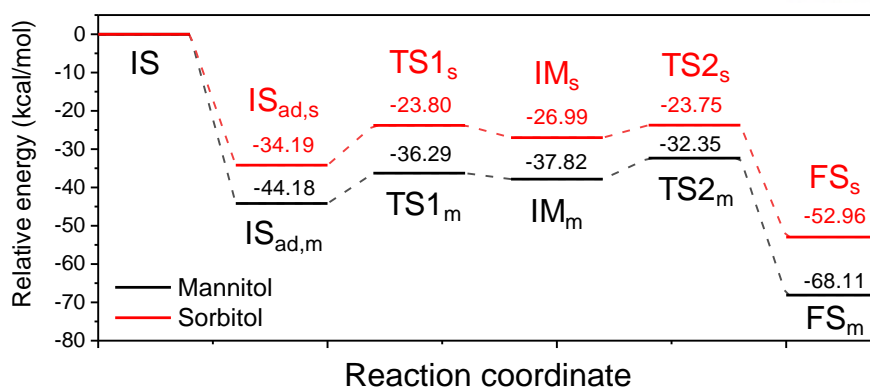
Figure 2.2.8 Reaction energy profiles of two fructose hydrogenation reaction.
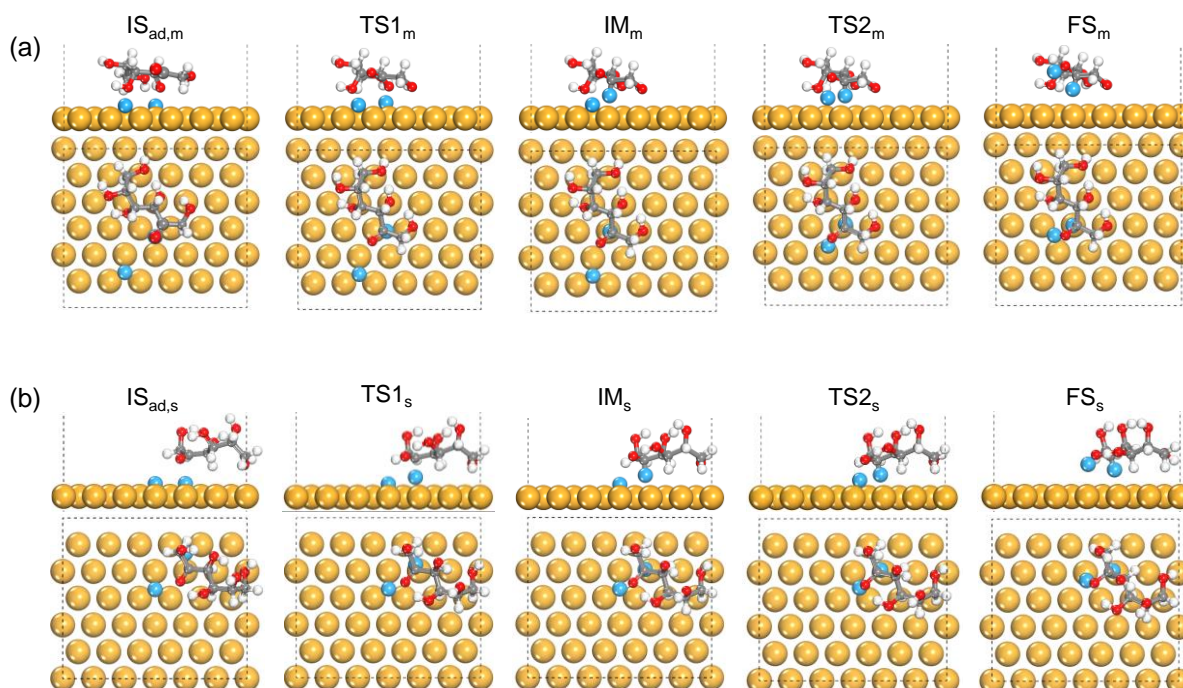
Figure 2.2.9 Front and top views of the configurations of the reaction states of (a) mannitol, and (b) sorbitol formation. For the clear view, top layer of Cu surface and adsorbed hydrogen are shown by space-filling model, while the fructose molecule are shown by ball-and-stick model. Copper and adsorbed hydrogen are colored in orange and sky blue, respectively. For fructose molecule, carbon, hydrogen, and oxygen atoms are colored in gray, white, red, respectively. 1-butanol molecule and bottom Cu layers in each reaction step are omitted.

We conducted further calculations under the other solvent conditions. In this calculation, we considered the implicit solvent condition (i. e., COSMO) for estimating the difference between binding

energies ($\Delta\Delta E_{B.E.}$) of $IS_{ad,m}$ and $IS_{ad,s}$ under each solvent (**Figure 2.2.10**). Here, $\Delta\Delta E$B.E. represents the selective formation of mannitol over sorbitol. The binding energies of $IS_{ad,m}$ under water and ethanol solvent conditions were slightly smaller than that estimated in 1-butanol (*i. e.*, $-\Delta E_{B.E.}$' s of 37.87, 38.56, and 38.85 kcal/mol for water, ethanol, and 1-butanol conditions, respectively). On the contrary, the binding energies of $IS_{ad,s}$ under water and ethanol were larger than that estimated in 1-butanol (*i. e.*, $-\Delta E_{B.E.}$' s of 32.51, 30.63, and 29.38 kcal/mol for water, ethanol, and 1-butanol conditions, respectively). Thus, the differences of binding energies between $IS_{ad,m}$ and $IS_{ad,s}$ under water and ethanol solvents were smaller than that of 1-butanol solvent (i. e., $\Delta\Delta E_{B.E.}$' s of 5.36, 7.93, and 9.47 kcal/mol for water, ethanol, and butanol conditions, respectively), indicating the reduced selectivity on mannitol formation at water and ethanol as shown in the experimental observation.
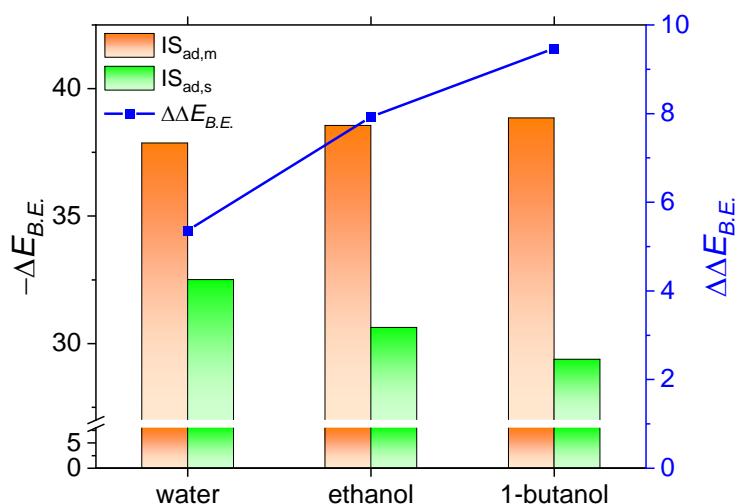
Figure 2.2.10 Binding energies of fructose ($\Delta E_{B.E.}$) and mannitol selectivity ($\Delta\Delta E_{B.E.}$) in each solvent.

2.2.4 Conclusion

We developed a promising protocol for the production of mannitol crystals from fructose using Cu(80)-SiO$_2$ nanocomposite as catalyst and 1-butanol as solvent for the first time. Using the DFT calculation, we identified that the stable initial structure of adsorbed fructose at $IS_{ad,m}$, mannitol pathway was more thermodynamically favorable than sorbitol pathway, and the mannitol formation reaction has the lower activation energy than that of sorbitol. Therefore, the present protocol is a novel and effective method to produce a pure mannitol from fructose in both an environmental and an industrial context.

2.2.5 References

1. Upare, P. P.; Hwang, Y. K.; Kim, J. C.; Lee, J. H.; Kwak, S. K.; Hwang, D. W. *ChemSusChem* **2020**, *13*, 5050–5057.

2. a) Alonso, D. M.; Bond, J. Q.; Dumesic, J. A. *Green Chem.* **2010**, 12, 1493–1513; b) Bozell, J. J.; Petersen, G. R. *Green Chem.* **2010**, 12, 539–554; c) Corma, A. ; Iborra, S.; Velty, A. *Chem. Rev.* **2007**, 107, 2411–2502; d) Kamm, B. *Angew. Chem. Int. Ed.* **2007**, 46, 5056–5058.

3. Makkee, M.; Kieboom, A.; Van Bekkum, H. *Starch* **1985**, 37, 136–141.

4. Dai, Y.; Meng, Q.; Mu, W.; Zhang, T. *J. Funct. Foods* **2017**, 36, 404–409.

5. Research and markets, Alternative sweetner- A Global Market Overview 2017–2022.

6. Bhatt, S. M.; Mohan, A.; Srivastava, S. K. *Biotechnol.* **2013**, 914187,1–13.

7. Saha, B. C.; Racine, F. M. *Appl. Microbiol. Biotechnol.* **2011**, 89, 879–891.

8. a) Liaw, B.-J.; Chen, C.-H.; Chen, Y.-Z. *Chem. Eng. J.* **2010**, 157, 140–145; b) Toukoniitty, B.; Kuusisto, J.; Mikkola, J.-P.; Salmi, T.; Murzin, D. Y. *Ind. Eng. Chem. Res.* **2005**, 44, 9370–9375; c) Zhang, J.; Xu, S.; Wu, S.; Liu, Y. *Chem. Eng. Sci.* **2013**, 99, 171–176.

9. a) Crezee, E.; Hoffer, B. W.; Berger, R. J.; Makkee, M.; Kapteijn, F.; Moulijn, J. A. *Appl. Catal. A* **2003**, 251, 1–17; b) Heinen, A. W.; Peters, J. A.; van Bekkum, H. *Carbohydr. Res.* **2001**, 330, 381–390.

10. a) Kuusisto, J.; Mikkola, J.-P.; Casal, P. P.; Karhu, H.; Väyrynen, J.; Salmi, T. *Chem. Eng. J.* **2005**, 115, 93–102; b) Zelin, J.; Meyer, C. I.; Regenhardt, S. A.; Sebastian, V.; Garetto, T. F.; Marchi, A. J. *Chem. Eng. J.* **2017**, 319, 48–56.

11. a) Upare, P. P.; Hwang, Y. K.; Lee, J. M.; Hwang, D. W.; Chang, J. S. *ChemSusChem* **2015**, 8, 2345–2357; b) Upare, P. P.; Lee, J. M.; Hwang, Y. K.; Hwang, D. W.; Lee, J. H.; Halligudi, S. B.; Hwang, J. S.; Chang, J. S. *ChemSusChem* **2011**, 4, 1749.

12. a) Upare, P. P.; Chamas, A.; Lee, J. H.; Kim, J. C.; Kwak, S. K.; Hwang, Y. K.; Hwang, D. W. *ACS Catal.* **2019**, 10, 1388–1396; b) Upare, P. P.; Hwang, D. W.; Hwang, Y. K.; Lee, U.-H.; Hong, D.-Y.; Chang, J.-S. *Green Chem.* **2015**, 17, 3310–3313; c) Upare, P. P.; Hwang, Y. K.; Hwang, D. W. *Green Chem.* **2018**, 20, 879–885.

13. García, V.; Päkkilä, J.; Ojamo, H.; Muurinen, E.; Keiski, R. L. *Renewable Sustainable Energy Rev.* **2011**, 15, 964–980.

14. a) Delley, B. *J. Chem. Phys.* **1990**, 92, 508–517; b) Delley, B. *J. Chem. Phys.* **2000**, 113, 7756–7764.

15. Perdew, J. P.; Burke, K.; Ernzerhof, M. *Phys. Rev. Lett.* **1996**, 77, 3865.

16. Tkatchenko, A.; Scheffler, M. *Phys. Rev. Lett.* **2009**, 102, 073005.

17. Klamt, A.; Schüürmann, G. *J. Chem. Soc. Perkin Trans. 2* **1993**, 799–805.

18. a) Bell, S.; Crighton, J. S. *J. Chem. Phys.* **1984**, 80, 2464–2475; b) Halgren, T. A.; Lipscomb, W. N. *Chem. Phys. Lett.* **1977**, 49, 225–232.

19. Castoldi, M. C. M.; Câmara, L. D. T.; Monteiro, R. S.; Constantino, A. M.; Camacho, L.; de Carneiro, J. W. M.; Aranda, D. A. G. *React. Kinet. Catal. Lett.* **2007**, 91, 341–352.

Chapter 3. Solvothermal liquefaction of alkali lignin to obtain a high yield of aromatic monomers while suppressing solvent consumption

This chapter includes the following contents:

3.1 Introduction

Lignin, which is 15–30 wt% lignocellulosic biomass, is the largest renewable source of naturally obtainable aromatic hydrocarbons. The efficient utilization of lignin has been acknowledged as the most logical alternative to the depleting fossil fuels for providing carbon-based sustainable chemicals and high-value polymeric materials, and for meeting growing energy demand.[2,3] Despite its outstanding potential as a renewable source of aromatic compounds, the recalcitrant nature of technical lignin (which is separated from lignocellulosic biomass) makes it extremely difficult to depolymerize.[4,5] Because of the lack of efficient and economically viable techniques for lignin depolymerization, most of the technical lignins, which are separated from wood using various methods (e.g., kraft pulping, sulfite pulping, soda pulping, organosolv pulping, concentrated strong acid hydrolysis, stream explosion, and ammonia fiber explosion), are currently burned as a low energy boiler fuel or used in low-value materials.[6]

To date, various types of thermochemical approaches with or without using molecular hydrogen and catalysts have been developed for lignin valorization.[2,3,7–9] For example, hot-water based hydrolysis in the presence of base catalysts[10–13] and hydrogenolysis in the presence of heterogeneous catalysts and hydrogen[14,15] have been investigated to produce phenol derived monomeric species under mild conditions. However, hot-water hydrolysis is unable to suppress the recombination reaction of highly reactive intermediates species, resulting in a high amount of char formation. Recently, considering the high solubility of the feedstock and their active hydrogen donation ability, the use of short-chain mono-alcohols (e.g., methanol, ethanol, and isopropanol) in the presence of nonnoble metal (e.g., Ni, Cu)-based or noble metal (e.g., Pd and Ru)-based catalysts have shown promising results in the fractionation of lignocellulosic biomass;[16–22] the reductive catalytic hydrogenolysis of intact lignin (which is not separated from the wood) could produce 20–50 wt% aromatic monomers under mild conditions. These short-chain alcohols, however, are far less efficient in producing aromatic monomers when applied in the depolymerization of the technical lignins even under harsh reaction conditions.[23,24]

The severity of technical lignin depolymerization is governed by the structural stability of the lignin. For example, the native lignin in the wood, which is enriched with thermally labile β-aryl ether groups (45–84% occurrence) with low bond dissociation energies (BDE: 54–72 kcal/mol), can be easily depolymerized under mild conditions, whereas it is difficult to depolymerize the technical lignin, which is enriched with a highly stable C–C (~ 90% occurrence) crosslinked structure having a high BDE (86– 118 kcal/mol).[3,4] This is because, during the lignin separation from lignocellulosic biomass, ether linkages in the intact lignin are cleaved and new stable C–C linkages are formed, making technical lignin highly thermochemically resistant.[5,25,26] For example, methanol, an effective solvent for the depolymerization of the intact lignin under mild reaction conditions (200–250 °C),[16–19] is not very capable of liquefying technical lignin even above its critical point (280–340 °C).[27–29] Not only does the formation of condensed linkages during the lignin separation, but also the choice of liquefaction medium has a significant effect on the lignin depolymerization. It has been suggested that methanol under high-pressure and high-temperature conditions (e.g., supercritical methanol, scMeOH) dehydrogenates to produce formaldehyde, which reacts with active intermediate species to enhance the char formation.[27] On the other hand, when supercritical ethanol (scEtOH) was subjected to the depolymerization of alkali and Kraft lignin at 340 °C for 4 h and 280 °C for 6 h over Cu- and Mo-based catalysts, high monomeric yields of 36.0 wt% and 33.3 wt%, respectively, were obtained.[28–30] This is attributed to the ability of scEtOH as a capping agent by alkylating the lignin-derived reactive intermediates to suppress repolymerization and as a formaldehyde (which is formed during lignin decomposition) scavenger to terminate the phenol-formaldehyde step-growth polymerization reaction; hence decreasing char formation.[31] These findings indicate that scMeOH and scEtOH not only act as a liquefaction solvent, but also as a reactant under high-pressure and high temperature conditions. Therefore, depending on their physiochemical properties and their reactivity with lignin-derived intermediate species, the short-chain alcohols play a vital role in determining the course of the depolymerization reaction. Even though encouraging results for lignin hydrogenolysis have been obtained through the combined use of alcohols (especially ethanol) and heterogeneous catalysts, alcohols could be more actively decomposed over the catalysts to produce various types of solvent-derived liquid products (SDLPs), including higher alcohols, esters, acetals, ethers, and aldehydes;[27–31] the presence of SDLPs in the bio-oil has definitively proven the high self-reactivity of alcohols. For instance, Ma et al. observed some ethanol-derived liquid products (EDLPs; 3.42 wt% based on ethanol) in molybdenum-based catalytic reactions at 280 °C for 6 h The choice of reaction conditions (temperature and pressure) and catalysts to control the lignin depolymerization also influences the self-reactivity of ethanol; for example, Huang et al. reported that EDLPs (e.g., higher alcohols and esters, ethers, aldehydes, and hydrocarbons) with different compositions and yields were produced depending on the reaction conditions.[29] The content of EDLPs (only C_{4+} species were quantified in their study) was up to 15.1 wt% based on ethanol during lignin depolymerization at 340 °C for 4 h in the presence

of CuMgAl$_x$ mixed oxide catalysts. These studies explained well the catalytic decomposition of ethanol to produce EDLPs; however, the non-catalytic decomposition behavior of ethanol is still unclear. Moreover, it is also imperative to understand the extent of solvent consumption in catalytic and non-catalytic reaction systems and other factors affecting its decomposition and reactivity in order to estimate the economic viability of the liquefaction process. Alcohols are much more expensive solvents than water, and thus their high consumption during lignin depolymerization is a primary concern for developing an economically viable liquefaction process. In addition to the economical aspect, the SDLPs formed at the expense of alcohols may complicate the characteristics of bio-oil by changing its physical (e.g., calorific value, molecular weight, viscosity, density) and chemical properties (e.g., chemical composition, stability, shelf life).[32] Therefore, it is highly desired to develop a reasonable approach for the use of alcoholic solvents in the depolymerization of technical lignin, and where a logically ideal approach should provide the complete conversion of technical lignin into a bio-oil phase and the production of a high yield of aromatic monomers, while at the same time suppressing the huge consumption of alcohols used as the solvent.

In this study, Jaehoon Kim's group is first aimed to understand the role of sub and supercritical alcohols (methanol, ethanol, and isopropanol) as a hydrogen donor, their self-reactivity, and degree of consumption in the absence of commonly used hydrodeoxygenation and hydrogenation catalysts (CoMo/Al$_2$O$_3$ and Ru/Al$_2$O$_3$) in blank experiments (in the absence of lignin). They explored the potency of an ethanol–formic acid mixture for depolymerizing technical lignin in the absence of expensive molecular hydrogen. Formic acid (FA) has successfully been employed for the depolymerization of oxidized intact lignin (which is enriched in facile β-aryl ether bonds) via redox neutral reactions to produce high monomeric yields under mild reaction conditions.[33] Therefore, we focused on the conversion of one of the technical lignins, namely alkali lignin, into a high yield of aromatic monomers with a detailed understanding of the role of alcohol and FA, not only as a hydrogen source, but also as a media to suppress the solvent consumption. The effects of reaction time and the FA-to-lignin ratio on the lignin-derived monomers and EDLPs were investigated to find the optimum condition for alkali lignin depolymerization. (**Table 3.1**) To understand the beneficial features of the ethanol–FA mixture and to explore the effect of formic acid in lignin depolymerization, we employed the reactive molecular dynamics (reax-MD) simulation for the solvothermal liquefaction mechanism of the dilignol molecules.

Entry	Time (min)	Conversion[f] (%)	Product yield[f] (wt %)			Reaction byproducts[g] (g)			Gas produced (mmol)				
			Bio-oil	Solid residue	Gas	Ethanol consumed	EDLPs	H_2O	H_2	CO	CO_2	CH_4	C_2H_6/C_2H_4
1[a]	30	60.8	112.7	40.5	3.15	8.8	1.13	0.7	0.98	1.15	0.47	1.19	0.49
2[b]	30	86.9	170.1	15.2	52.7	28.1	2.55	5.74	13.30	2.49	0.88	3.95	50.68
3[c]	30	80.1	157.8	21.7	64.7	25.4	2.03	5.16	9.74	4.86	0.60	34.4	29.47
4[d]	30	99.1	145.6	2.5	150.4	4.2	0.15	6.01	36.10	22.23	15.75	0.95	1.66
5[d]	60	100	164.9	1.3	188.7	7.1	0.38	6.33	35.09	37.51	17.94	1.59	2.25
6[d]	300	98.9	163.7	3.3	199.6	17.5	1.55	7.31	76.35	85.21	33.51	4.52	4.93
7[d]	900	100	221.1	0.8	238.0	27.5	4.05	7.56	116.3	53.12	62.50	8.42	13.40
8[e]	60	97.6	154.7	4.7	172.3	9.1	0.38	6.36	22.39	22.93	22.09	3.01	2.22

Reaction conditions: [a] 3 g lignin, 60 g ethanol. [b] 3 g lignin, 60 g ethanol, 0.5 g CoMoS/γ-Al$_2$O$_3$. [c] 3 g lignin, 60 g ethanol, 0.5 g Ru/γ-Al$_2$O$_3$. [d] 3 g lignin, 60 g ethanol, 12 g formic acid. [e] 6 g lignin, 60 g ethanol, 12 g formic acid. [f] Calculated after drying. [g] Calculated immediately after the reaction, before solvent separation.

Table 3.1 Comparison of product yields and byproducts at 350 °C in the experiment.

3.2 Computational Models and Methods

To predict the depolymerization mechanism of lignin, we employed molecular simulation methods. Since lignin is composed of several representative linkages in its structure,[34] we modeled five dilignol molecules, where two coniferyl alcohol units were connected by a C–O or C–C linkage, to easily identify the bond dissociation mechanisms of each linkage.[35–37] Each dilignol was named by the location of the connecting atoms: 4-O-5, β-1, α-O-4, β–β, and β-O-4 (**Figure 3.1**). **Figure 3.2** presents the simulation procedures. Using these dilignol models, reactive molecular dynamics (reax-MD) simulations were conducted to observe the dissociation process of the dilignol molecules in the ethanol–FA mixture. In addition, the thermodynamic preference of the observed mechanisms in the ethanol–FA mixture was compared with those in different solvent conditions (i.e., the reaction with ethanol or without any solvent) using density functional theory (DFT) calculations.

All the reax-MD simulations were performed by following a reactive forcefield (reaxFF) developed by Chenoweth et al.[38] using the LAMMPS package.[39,40] Considering the weight ratio of ethanol and FA used in the experiment, each system for the reax-MD calculation was constructed with 600 ethanol and 120 FA molecules. To investigate the diverse depolymerization mechanisms of the lignin molecules, we considered 20 molecules, which corresponded to twice the experimental composition. To prevent undesired decompositions possibly caused by instability of the initial model system, the system was subjected to NPT (i.e., an isothermal–isobaric ensemble) MD simulation for 200 ps with a 1 fs timestep using the COMPASS II forcefield;[41] then an additional NPT MD simulation using reaxFF with a 0.1 fs timestep was run for 50 ps at room temperature. For the data production, NVT (i.e., an isothermal ensemble) MD simulation was performed for 100 ps at three temperatures (i.e., 1800 K, 1900 K, 2000 K). The elevated temperature allowed the decomposition reactions to be completed promptly in a practical manner and was applied to previous studies that investigated the

decomposition mechanisms.[35–37,42] The species and simulation trajectory recognized through the bond order were analyzed for every 1000 simulation steps.

DFT calculations were carried out for the identification and energy analysis of the lignin depolymerization mechanism with and without the ethanol–FA mixture. The Dmol[3] program[43,44] was used for the calculation with the Perdew– Burke–Ernzerhof (PBE) functional[45] with the Double Numerical basis with Polarization (DNP) 4.4 basis set. Mechanisms for the C–O and C–C linkage decomposition reaction were obtained considering the conformations of the molecules from the reax-MD simulation result. The conductor-like screening model (COSMO) method[46] was applied to include the effect of the surrounding solvent (i.e., use of the dielectric constant of ethanol) besides the actual ethanol molecules involved in the reaction calculation. The Tkatchenko–Scheffler scheme[47] was applied to account for the van der Waals correction. The convergence criteria for the energy, force, and displacement were set as 1.0×10^{-5} Ha, 0.002 Ha/Å, and 0.005 Å, respectively. The complete linear synchronous transit/Quadric synchronous transit (LST/QST) method[48,49] was applied to obtain the transition state at the kinetic barrier of the decomposition reaction, and the convergence criteria for the root mean square (RMS) force was set to be 0.003 Ha/Å.
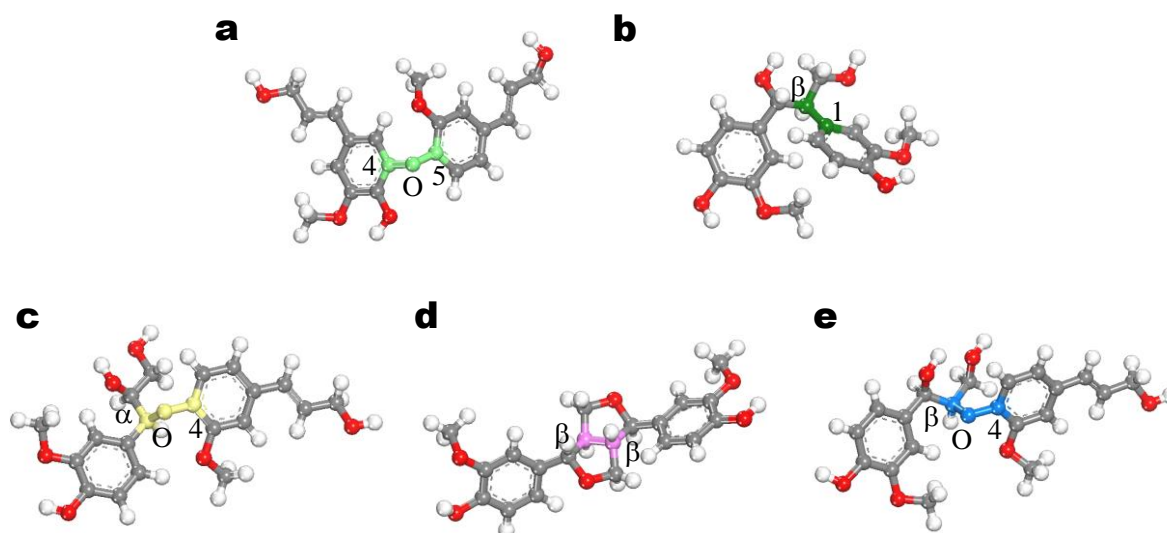
Figure 3.1 Molecular models of (a) 4-O-5, (b) β-1, (c) α-O-4, (d) β-β, and (e) β-O-4 dilignol, respectively. For the clear view, the atoms comprising lignin linkage of the dilignol molecule is colored in green with the notes to indicate the connecting atoms. Carbon, hydrogen, and oxygen atoms are colored in gray, white, and red, respectively, except the linkage atoms.
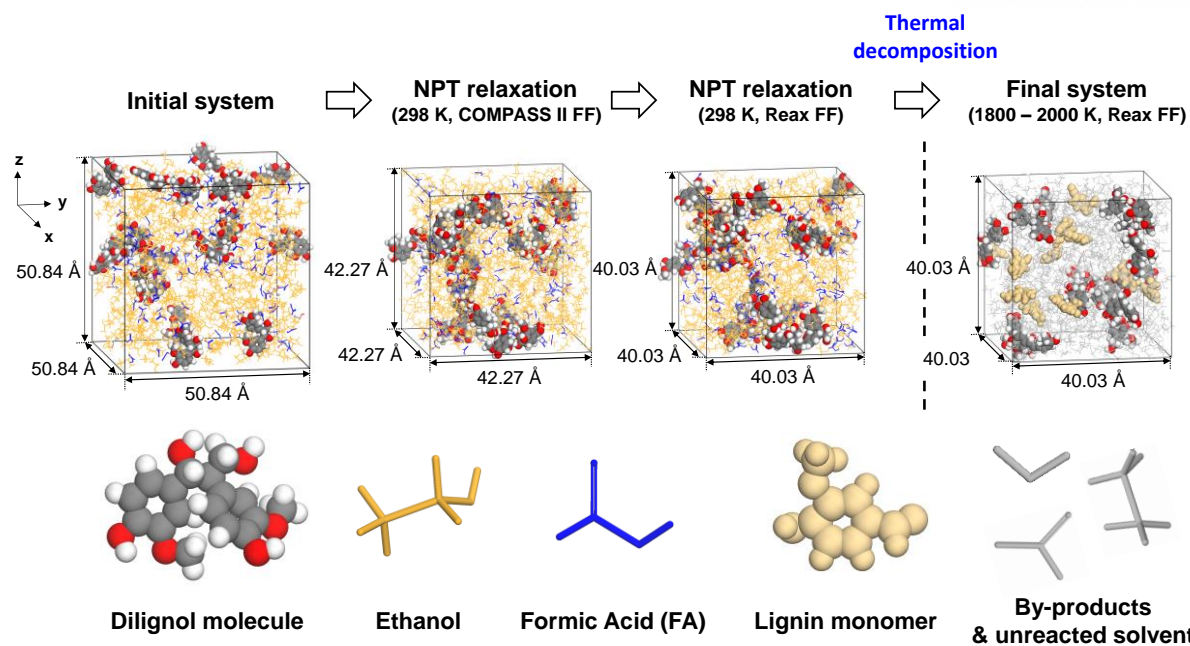
Figure 3.2 Schematic illustration of simulation models by reax-MD simulation procedure. The lattice parameters were taken from the β-1 dilignol system, and there were less than 1 Å differences between systems. From the initial to NPT relaxation using reax FF, simulation system was composed of three species, *i.e.,* dilignol molecule, ethanol, and formic acid (FA). For the clear view, ethanol and FA were presented by orange and blue stick, respectively. Dilignol molecules were shown by CPK style with each atomic color (*i.e.,* gray, red, and white for carbon, oxygen, and hydrogen, respectively). After the thermal decomposition, final system was composed of unreacted reactants, lignin monomers, and byproducts. Except dilignol molecules, lignin monomers and remaining byproducts including unreacted solvent are shown by ivory CPK molecule, and light gray stick, respectively.

3.3 Result and Discussion

To understand the reason behind the increasing efficiency of lignin depolymerization in the ethanol–FA mixture, the lignin depolymerization mechanisms were investigated by employing molecular simulation. The five representative linkages of the lignin, namely C–O (4-O-5, α-O-4, β-O-4), and C–C (β-1, β–β) bonds, were chosen in the dilignol molecules (Figure 3.1). As shown in **Figure 3.3**, both the C–O and C–C bonds in the dilignol molecules were broken in the ethanol– FA mixture; and at the three different temperatures of 1800, 1900, and 2000 K considered during the simulation time of 100 ps, more than 60% dilignols were decomposed. The increase in temperature resulted in an enhanced decomposition rate of each dilignol molecule. The decomposition rate of FA was more than double that of ethanol, which indicated that the depolymerization of lignin was more closely related to

the decomposition of FA rather than ethanol.
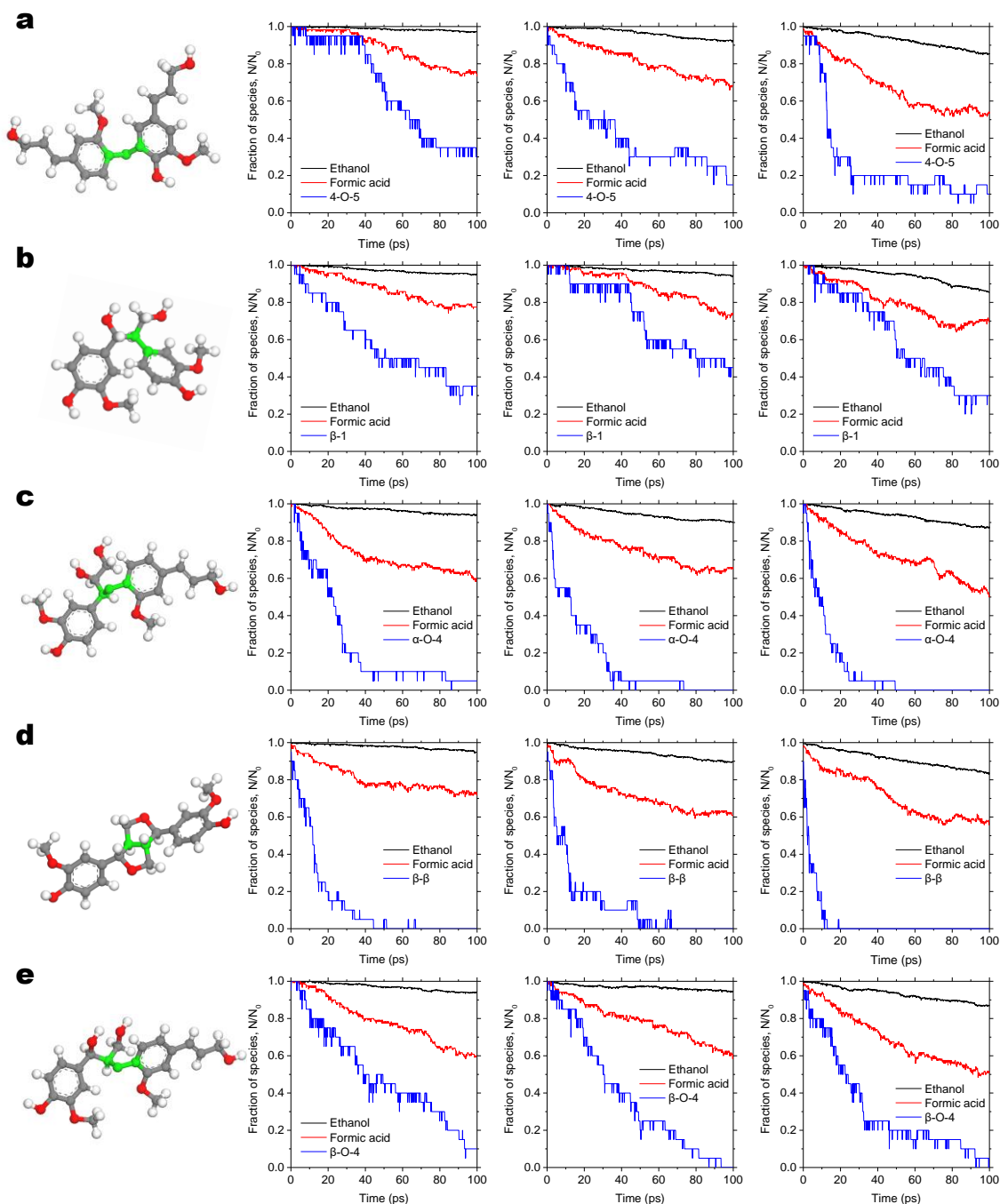
Figure 3.3 Thermal decomposition results of: (a) 4-O-5, (b) β-1, (c) α-O-4. (d) β–β, and (e) β-O-4 dilignol molecules in the ethanol–FA mixture. From left to right, reacting dilignol molecule and scaled number of reactants versus reax-MD simulation time at temperatures of 1800 K, 1900 K, and 2000 K are presented. Number of molecules of each species is scaled by the initial number of each species, i.e., N0 = 20, 600, and 120 for dilignol, ethanol, and FA, respectively. Color scheme of dilignol molecule is same as **Figure 3.1**

To verify this, the step-by-step mechanisms of dilignol depolymerization were investigated under the ethanol–FA mixture environment at each simulation temperature with respect to the simulation time. **Figure 3.4** shows the depolymerization process and corresponding simulation time of each dilignol during the reax-MD simulation at 1800 K. Regardless of the simulation temperatures, the overall dissociation pathway of each linkage was similar except for the time of occurrence. The C–O or C–C bonds were either broken by hydrogen generated from the degraded solvent or by thermal energy. A detailed step-by-step description of the decomposition mechanisms is presented. Briefly, when the radical fragment is formed by the thermal breakage of the bonds, the reaction intermediate became a stable monomer by receiving hydrogen from the solvent around the radical fragment. It was noted herein that the solvent that provided the hydrogen for lignin depolymerization was mainly FA, as predicted from the decomposition rate of the reax-MD simulation.
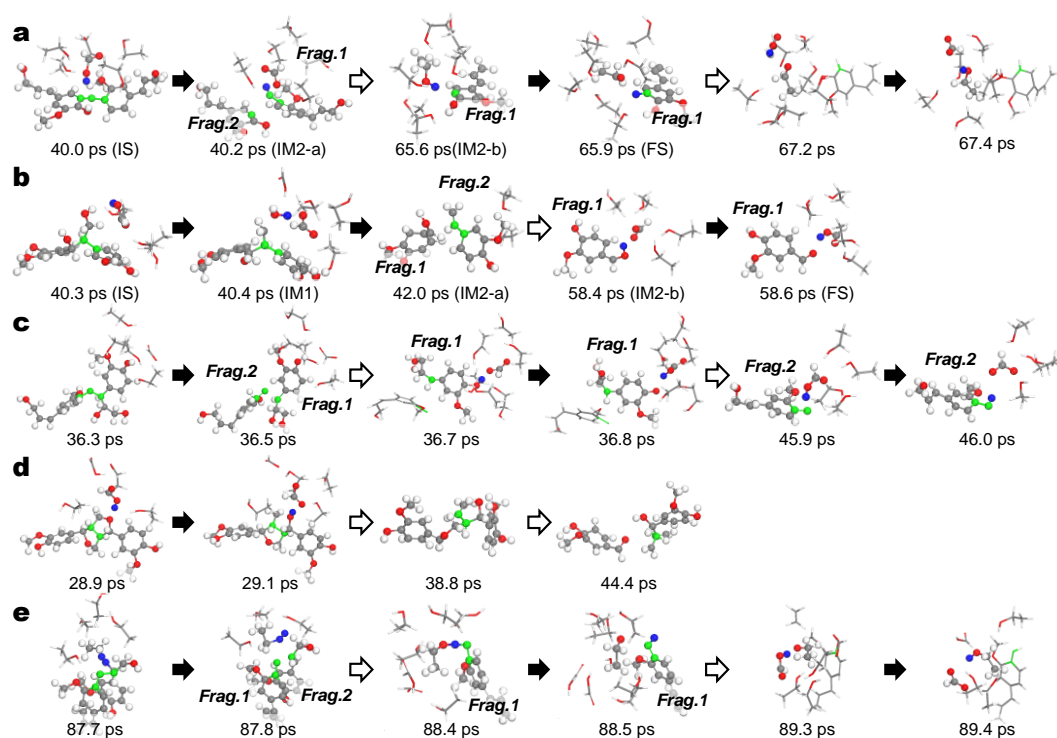
Figure 3.4 Depolymerization mechanisms of the dilignol molecules observed in the reax-MD simulation. The numbers below each figure represent the corresponding time in the decomposition simulation at 1800 K. For a clear view of the reaction mechanism, the reacting molecules in each snapshot are presented using a ball-and-stick model, whereas the others are shown by a stick model. Empty arrows indicate consecutive procedures, and filled arrows indicate the reactant and product of the reaction. Decomposition intermediates of the dilignol molecules are indicated by 'Frag.1' and 'Frag.2', respectively. The atoms comprising lignin linkage of the dilignol molecule are colored in green and transferring H atoms (or OH groups) are colored in blue. Except these atoms, carbon, hydrogen, and oxygen atoms are colored in gray, white, and red, respectively.

On the other hand, it was also observed that ethanol was decomposed to provide hydrogen as a radical fragment. In this case, the ethanol was regenerated after the FA was decomposed and the generated hydrogen then migrated to the previously decomposed ethanol (e.g., 67.4 ps in **Figure 3.4a**; 89.4 ps in **Figure 3.4e**). This phenomenon agrees well with the experimental result; whereby when the ethanol–FA mixture was used, the amount of decomposed ethanol was smaller compared to when ethanol alone was used. In the ethanol–FA mixture, the decomposition of FA was more facilitated than that of ethanol. To compare the effects of ethanol and FA on lignin depolymerization, DFT calculations were employed to predict the mechanisms by which the typical C–O or C–C linkages of dilignols (i.e., 4-O-5 and β-1 cases) break under various reaction conditions. The dissociation mechanisms of the initial lignin linkages were calculated for three different cases, as shown in **Figure 3.5**: thermal dissociation (i.e., without solvent), dissociation in ethanol only, and dissociation in the ethanol– FA mixture. When the C–O bond of 4-O-5 dilignol was thermally broken (IM2′), the required energy was 68.76 kcal/mol. On the other hand, a much lower energy was required when hydrogen was supplied from the solvent and the bond was broken; in particular, the heat of reaction (ΔE) and the activation energy (E_a) of 44.96 kcal/mol and 51.72 kcal/mol, respectively, in the step of transferring hydrogen to 4-O-5 dilignol from the decomposed FA. These values were lower than those when ethanol only participated in the reaction (ΔE = 55.64 kcal/mol, E_a = 63.69 kcal/mol). In addition, only 2.68 kcal/mol was required from the transition of IM1 (40.0 ps in Figure. 3.4) to IM2 stage (40.2 ps in Figure 3.4), where the C–O bond in the hydrogenated structure was broken and thus the dilignol was decomposed into two molecules. From IM2 (65.6 ps in Figure 3.4) to the FS stage (65.9 ps in Figure 3.4), in which the separated radical fragments abstract hydrogen from ethanol, a low activation energy of 0.72 kcal/mol and a large heat of reaction of −22.19 kcal/mol resulted. Therefore, based on the DFT calculations, it was predicted that lignin could be more efficiently decomposed in the ethanol–FA mixture, which agrees well with the experimental results.
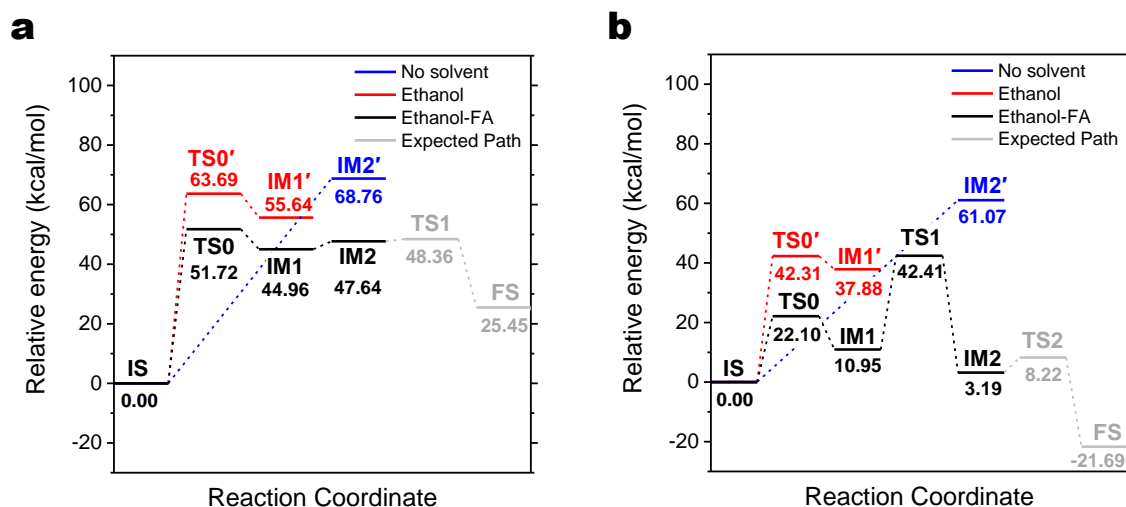
Figure 3.5 DFT calculations of the depolymerization mechanism of: (a) 4-O-5 dilignol and (b) β-1 dilignol molecules without solvent (blue line), with ethanol only (red line), and with the ethanol–FA mixture (black line). Expected mechanism after the dissociation of lignin linkage in the ethanol–FA mixture is shown by the gray line.

As shown in Figure 3.5, similar solvent effects were observed in the decomposition of the C–C bonded, β-1 dilignol molecule. The thermal dissociation reaction led to dissociation of the C–C bond and required a high energy of 61.07 kcal/mol (IM2′). The first step of the C–C bond cleavage of β-1 dilignol using a solvent was considered to be the formation of protonated hydroxyl by bonding of the hydroxyl group centered in β-1 dilignol and transfer of hydrogen from the neighboring solvent (from 40.3 ps to 40.4 ps of Figure 3.4). As expected, FA required less heat of reaction and activation energy to react with β-1 dilignol than those of ethanol only (i.e., $\Delta E = 10.95$ kcal/mol and $E_a = 22.10$ kcal/mol in the presence of FA, while $\Delta E = 37.88$ kcal/mol and $E_a = 42.31$ kcal/mol in the presence of ethanol). The reaction from IM1 (40.4 ps in Figure 3.4) to IM2 (42.0 ps in Figure 3.4) involved breakage of the C– C bond after forming a vinyl group by separating the water from the hydrogenated dilignol radical structure. This reaction required a ΔE of -7.76 kcal/mol and E_a of 31.46 kcal/mol, respectively. This depolymerization step could efficiently proceed as compared to IM2′ (without solvent). After this step, a large exothermic reaction occurred at the regeneration of FA, where the separated radical lignin molecule (from 58.4 ps to 58.6 ps in Figure 3.4) transported hydrogen to the radical FA ($\Delta E = -24.88$ kcal/mol and $E_a = 5.03$ kcal/mol). In short, the decompositions of C–C and C–O linkages of lignin under the ethanol–FA mixture environment (e.g., a large amount of FA was decomposed, while the decomposition of ethanol was suppressed) were more advantageous than those of the thermal- and ethanol-assisted decomposition reactions.

3.4 Conclusion

Although the presence of commonly used molybdenum- or metal-based catalysts increases the hydrogen-donation ability of the alcohols, these catalysts also have enhanced their self-reactivity, which in turn results in a huge solvent consumption. Due to its ability to scavenge lignin-derived active radicals, supercritical ethanol (scEtOH) was selected as a liquefaction solvent. The combined use of scEtOH and formic acid (FA) not only produced high lignin derived monomers (LDMs) from the recalcitrant alkali lignin without using external catalysts and molecular hydrogen, but also suppressed the solvent consumption by retarding the solvent decomposition reactions. According to the lignin solvothermal liquefaction mechanism using the reax-MD simulation and DFT calculation, the scEtOH–FA mixture was efficient enough to dissociate C–C bonds in the alkali lignin along with the labile β-O-4 ether bonds. Furthermore, it was confirmed that formic acid acts as hydrogen supply and scEtOH serves as hydrogen delivery, and the depolymerization of lignin under the scEtOH-formic acid mixture solvent were more advantageous than those of thermal energy or scEtOH solvent. Therefore, although scEtOH is a promising solvent for the liquefaction of technical lignin, the extended reaction times and the use of highly active heterogeneous catalysts can lead to an excess consumption of ethanol.

3.5 References

1. Riaz, A.; Verma, D.; Zeb, H.; Lee, J. H.; <u>Kim, J. C.</u>; Kwak, S. K.; Kim, J. *Green Chemistry* **2018**, 20, 4957–4974.

2. Ragauskas, A. J.; Beckham, G. T.; Biddy, M. J.; Chandra, R.; Chen, F.; Davis, M. F.; Davison, B. H.; Dixon, R. A.; Gilna, P.; Keller, M.; Langan, P.; Naskar, A. K.; Saddler, J. N.; Tschaplinski, T. J.; Tuskan G. A.; Wyman, C. E. *Science*, **2014**, 344, 1246843.

3. Rinaldi, R.; Jastrzebski, R.; Clough, M. T.; Ralph, J.; Kennema, M.; Bruijnincx, P. C.; Weckhuysen, B. M. *Angew. Chem., Int. Ed.*, **2016**, 55, 8164–8215.

4. Calvaruso, G.; Clough, M. T.; Rechulski, M. D. K.; Rinaldi, R. *ChemCatChem*, **2017**, 9, 2691–2700.

5. El Hage, R.; Brosse, N.; Sannigrahi, P.; Ragauskas, A. *Polym. Degrad. Stab.*, **2010**, 95, 997–1003.

6. Belgacem, M. N.; Gandini, A. Monomers, Polymers and Composites from Renewable Resources, Elsevier, Oxford, UK, **2008**.

7. Zakzeski, J.; Bruijnincx, P. C.; Jongerius, A. L.; Weckhuysen, B. M. *Chem. Rev.*, **2010**, 110, 3552–3599.

8. Xu, C.; Arancon, R. A.; Labidi, J.; Luque, R. *Chem. Soc. Rev.*, **2014**, 43, 7485–7500.

9. Deuss, P. J.; Barta, K. Coord. *Chem. Rev.*, **2016**, 306, 510–532.

10. Hidajat, M. J.; Riaz, A.; Park, J.; Insyani, R.; Verma, D.; Kim, J. *Chem. Eng. J.*, **2017**, 317, 9–19.

11. Roberts, V. M.; Stein, V.; Reiner, T.; Lemonidou, A.; Li, X.; Lercher, J. A. *Chem. Eur. J.*, **2011**, 17, 5939–5948.

12. Erdocia, X.; Prado, R.; Corcuera, M. Á.; Labidi, J. *Biomass Bioenergy*, **2014**, 66, 379–386.

13. Long, J.; Zhang, Q.; Wang, T.; Zhang, X.; Xu, Y.; Ma, L. *Bioresour. Technol.*, **2014**, 154, 10–17.

14. Onwudili, J. A.; Williams, P. T. *Green Chem.* **2014**, 16, 4740–4748.

15. Zhang, J.; Teo, J.; Chen, X.; Asakura, H.; Tanaka, T.; Teramura, K.; Yan, N. *ACS Catal.* **2014**, 4, 1574–1583.

16. Ferrini, P; Rinaldi, R. *Angew. Chem., Int. Ed.* **2014**, 53, 8634–8639.

17. Li, C.; Zheng, M.; Wang, A.; Zhang, T. *Energy Environ. Sci.* **2012**, 5, 6383–6390.

18. Song, Q.; Wang, F.; Cai, J.; Wang, Y.; Zhang, J.; Yu, W.; Xu, J. *Energy Environ. Sci.* **2013**, 6, 994–1007.

19. Van den Bosch, S.; Schutyser, W.; Vanholme, R.; Driessen, T.; Koelewijn, S. F.; Renders, T.; De Meester, B.; Huijgen, W. J. J.; Dehaen, W.; Courtin, C. M.; Lagrain, B.; Boerjan, W.; Sels, B. F. *Energy Environ. Sci.* **2015**, 8, 1748–1763.

20. Huang, X. M.; Gonzalez, O. M. M.; Zhu, J. D.; Koranyi, T. I.; Boot, M. D.; Hensen, E. J. M. *Green Chem.* **2017**, 19, 175–187.

21. Van den Bosch, S.; Renders, T.; Kennis, S.; Koelewijn, S. F.; Van den Bossche, G.; Vangeel, T.; Deneyer, A.; Depuydt, D.; Courtin, C. M.; Thevelein, J. M.; Schutyser, W.; Sels, B. F.; *Green Chem.* **2017**, 19, 3313–3326.

22. Sun, Z.; Bottari, G.; Afanasenko, A.; Stuart, M. C. A.; Deuss, P. J.; Fridrich, B.; Barta, K. *Nat. Catal.* **2018**, 1, 82–92.

23. Riaz, A.; Kim, C. S.; Kim, Y.; Kim, J. *Fuel* **2016**, 172, 238–247.

24. Erdocia, X.; Prado, R.; Fernández-Rodríguez, J.; Labidi, J.; *ACS Sustainable Chem. Eng.* **2015**, 4, 1373–1380.

25. Constant, S.; Wienk, H. L. J.; Frissen, A. E.; Peinder, P. d.; Boelens, R.; van Es, D. S.; Grisel, R. J. H.; Weckhuysen, B. M.; Huijgen, W. J. J.; Gosselink, R. J. A.; Bruijnincx, P. C. A. *Green Chem.* **2016**, 18, 2651–2665.

26. Bouxin, F. P.; McVeigh, A.; Tran, F.; Westwood, N. J.; Jarvis, M. C.; Jackson, S. D. *Green Chem.* **2015**, 17, 1235–1242.

27. Huang, X.; Koranyi, T. I.; Boot, M. D.; Hensen, E. J. *ChemSusChem*, **2014**, 7, 2276–2288.

28. Ma, R.; Hao, W.; Ma, X.; Tian, Y.; Li, Y. *Angew. Chem., Int. Ed.* **2014**, 53, 7310–7315.

29. Huang, X.; Atay, C.; Korányi, T. I.; Boot, M. D.; Hensen, E. J. M. *ACS Catal.* **2015**, 5, 7359–7370.

30. Ma, X.; Ma, R.; Hao, W.; Chen, M.; Yan, F.; Cui, K.; Tian, Y.; Li, Y. *ACS Catal.* **2015**, 5, 4803–4813.

31. Huang, X. M.; Koranyi, T. I.; Boot, M. D.; Hensen, E. J. M. *Green Chem.* **2015**, 17, 4941–4950.

32. Zeb, H.; Choi, J.; Kim, Y.; Kim, J. *Energy* **2017**, 118, 116–126.

33. Rahimi, A.; Ulbrich, A.; Coon, J. J.; Stahl, S. S. *Nature*, **2014**, 515, 249–252.

34. Dorresetijin, E.; Laarhoven, L. J. J.; Arends, I. W. C. E.; Mulder, P. *J. Anal. Appl. Pyrolysis*, **2000**, 54, 153–193.

35. Chen, B.; Wei, X.-Y.; Yang, Z.-S.; Liu, C.; Fan, X.; Qing, Y.; Zong, Z.-M. *Energy Fuels*, **2012**, 26, 984–989.

36. Beste, A. *J. Phys. Chem. A*, **2014**, 118, 803–814.

37. Beste, A. *Energy Fuels*, **2014**, 28, 7007–7013.

38. Chenoweth, K.; van Duin, A. C. T.; Goddard, W. A. *J. Phys. Chem. A*, **2008**, 112, 1040–1053.

39. Plimpton, S. *J. Comput. Phys.*, **1995**, 117, 1–19.

40. Aktulga, H. M.; Fogarty, J. C.; Pandit, S. A.; Grama, A. Y. *Parallel Comput.*, **2012**, 38, 245–259.

41. Sun, H.; Jin, Z.; Yang, C. W.; Akkermans, R. L. C.; Robertson, S. H.; Spenley, N. A.; Miller, S.; Todd, S. M. *J. Mol. Model.*, **2016**, 22, 1–10.

42. Zhang, T.; Li, X.; Qiao, X.; Zheng, M.; Guo, L.; Song, W.; Lin, W. *Energy Fuels*, **2016**, 30, 3140–3150.

43. Delley, B. *J. Chem. Phys.*, **1990**, 92, 508–517.

44. Delley, B. *J. Chem. Phys.*, **2000**, 113, 7756–7764.

45. Perdew, J. P.; Ernzerhof, M.; Burke, K.; *J. Chem. Phys.,* **1996**, 105, 9982–9985.

46. B. Delley, Mol. Simul., 2006, 32, 117–123.

47. Tkatchenko, A.; Scheffler, M. *Phys. Rev. Lett.*, **2009**, 102, 073005.

48. Bell, S.; Crighton, J. S. *J. Chem. Phys.*, **1984**, 80, 2464–2475.

49. Halgren, T. A. *Chem. Phys. Lett.*, **1997**, 49, 225–232

Chapter 4. Universal Solution Synthesis of Sulfide Solid Electrolytes Using Alkahest for All-Solid-State Batteries

This chapter includes the following contents:

Lee, J. E.;† Park, K.-H.;† <u>Kim, J. C.</u>;† Wi, T.-U.; Ha, A. R.; Song, Y. B.; Oh, D. Y.; Woo, J.; Kweon, S. H.; Yeom, S. J.; Cho, W.; Kim, K. S.; Lee, H.-W.;* Kwak, S. K.;* Jung, Y. S.* *Advanced Materials* **2022**, 34, 2200083. Reproduced from ref. 1 with permission from the © 2022 Wiley-VCH GmbH Publications. († : equally contributed)

4.1 Introduction

The solution processing of metal chalcogenides is key to various electronic- and energy-related devices. All-solid-state batteries (ASSBs) modified to achieve better safety and higher energy density have been emerging for application in battery driven electric vehicles.[2] In addition, a recent article in transport and environment reported that solid-state-battery, which stores more energy with the less materials, can reduce the carbon footprint of electric car battery.[3] Owing to their high ionic conductivities that reach a maximum of $\approx 10^{-2}$ S/cm at room temperature (*e.g.*, $Li_{10}GeP_2S_{12}$ (LGPS):[4] 12 mS/cm and $Li_{5.5}PS_{4.5}Cl_{1.5}$:[5] 9.4 mS/cm) and mechanical deformability that eases the integration to devices, sulfide superionic conductors hold great promise for practical ASSB technologies.[2a,c,j,4–5] Notably, several sulfide solid electrolyte (SE) materials can be synthesized or processed via soft chemistry using liquid solvents, which has become a popular topic in ASSB research.[6]

The "wet" preparation for sulfide SEs is classified into three categories (**Figure 4.1**) i) suspension synthesis, ii) solution process, and iii) solution synthesis. In suspension synthesis, SE precursors are partly dissolved in organic solvents (*e.g.*, tetrahydrofuran and acetonitrile) and the reaction proceeds via a suspension state, with organic solvents serving as a medium for soft chemistry.[7] Compared to conventional solid-state synthesis, the suspension synthesis of sulfide SEs has multiple advantages, such as a reduced reaction time and scalable production of SEs or electrodes.[6b,8] In the solution process, the sulfide SEs, not precursors, are dissolved in specific polar solvents, forming a homogeneous solution. Original SEs can be precipitated via the removal of solvents and subsequent heat treatment (HT). The liquefied sulfide SEs for the solution process can be utilized for coating on active materials[9] and the infiltration of porous composite electrodes or separators.[9a,10] In addition, in situ formation of nanocomposite electrodes via solution processing has been reported.[8b,11] All these methods have demonstrated exceptional advantages in forming intimate ionic contacts and alternative production

capability of ASSBs. Solution synthesis, in which SE precursors are fully dissolved in solvents and SEs are formed via the removal of solvents, could be ideal because it combines the advantages of both the solution process (i.e., forming a homogeneous solution) and suspension synthesis (i.e., using SE precursors). However, solvents that are known to form homogeneous SE solutions (e.g., ethanol (EtOH) and water) are highly polar and protic, and they readily hydrolyze P_2S_5 and/or Li_2S precursors. This explains the limited types of solution-processable SEs, such as (LiI−) Li_4SnS_4 using methanol (MeOH) or water, Li_6PS_5Cl (LPSCl) using EtOH, and Na_3SbS_4 using MeOH or water.[9b] To date, only a few solution syntheses for sulfide SEs have been identified.[12] Notably, all suspension and solution syntheses of SEs thus far have covered only restricted compositions, those based on binary ($Li_2S−P_2S_5$) or ternary systems ($Li_2S−P_2S_5−LiX$), and excluded metal sulfides such as GeS_2. This is attributed to the limited dissolving power of the solvents used for the suspension synthesis. Thus, the counteracting requirement of solvents for solution synthesis, i.e., high dissolving power for homogeneous solutions but inertness toward vulnerable sulfide precursors, has been a formidable challenge. Here, we demonstrate the first universal solution synthesis of sulfide SEs using an alkahest solvent system. Binary mixtures of 1,2-ethylenediamine (EDA)−1,2-ethanedithiol (EDT) and EDA−ethanethiol (ET), which show strong dissolving power for metal chalcogenides, fully dissolved not only conventional sulfide SE precursors of Li_2S, P_2S_5, and Na_2S, but also metal sulfides, such as GeS_2 by the Raman spectroscopy. (**Figure 4.2**) To identify the effect of EDT in dissolution of germanium disulfide precursor, the dissolution mechanism of GeS_2 in EDA−EDT solvents was revealed using density functional theory (DFT) calculations.
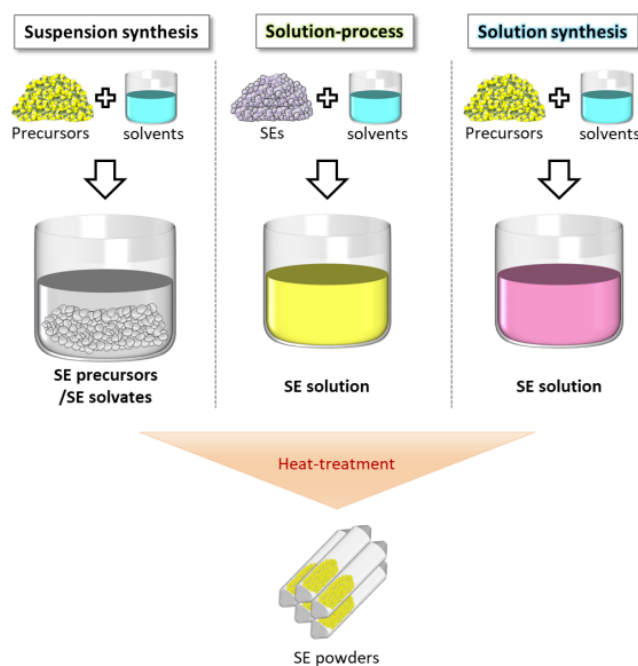
Figure 4.1 Schematic image of three synthetic protocols for sulfide solid electrolytes.
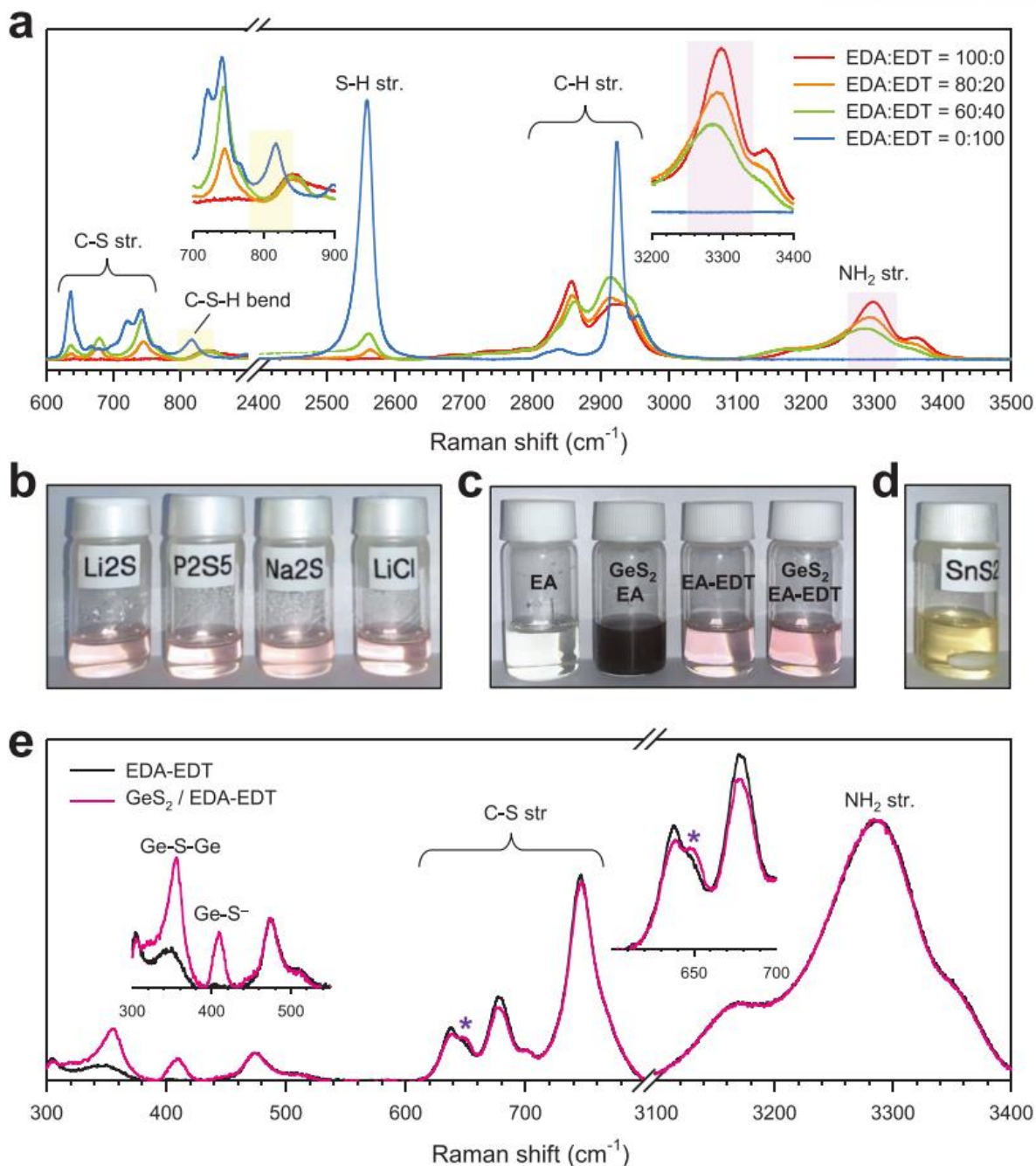
Figure 4.2 Results of the dissolution of sulfide SE precursors in EDA–EDT cosolvents. a) Raman spectra of EDA−EDT cosolvents with varying volume ratio. The insets show enlarged views of the C−S–H bending peaks (highlighted in yellow) and NH_2 stretching peaks (highlighted in pink). b) Photograph of SE precursors, Li_2S, P_2S_5, Na_2S, LiCl, in EDA−EDT. c) Photograph of GeS_2 in EDA and EDA−EDT. d) Photograph of SnS_2 in EDA−EDT. e) Raman spectra for the solution of GeS_2 dissolved in the EDA−EDT cosolvent, showing the signals of Ge−S⁻ and Ge−S−Ge (inset), in comparison with that for the EDA−EDT cosolvent. The inset in the right shows an enlarged view of the C–S stretching peaks and unknown peak (denoted as "*").

4.2 Computational Models and Methods

All DFT calculations were performed using DMol[3] program.[13] The electron exchange-correlation energy was calculated with the generalized gradient approximation and the Perdew−Burke−Ernzerhof functional.[14] The effective core potential was used for core treatment with a basis set of DNP 4.4 level. The convergence criteria for energy, force, and displacement were set as $1.0×10^{-5}$ Ha, 0.002 Ha/Å, and 0.005 Å, respectively. The Conductor−like Screening Model solvation model was applied using the dielectric constant of EDA–EDT (10:1 vol) solvent mixture (ε 15.83).[15] To include the dispersion correction of the van der Waals effect, the DFT empirical dispersion correction (DFT-D3) was used. The Brillouin-zone was sampled by a Monkhorst−Pack as a single k-point (Γ-point) for surface model systems. The dipole slab correction was also employed for all slab calculations. To examine the reaction paths, the linear synchronous transit and quadratic synchronous transit methods were used to satisfy the convergence criteria of the RMS force, which was set as 0.003 Ha/Å.[16] To observe the proton transfer reaction in the EDA−EDT mixture solvent, a DFT model with the explicit solvents was sampled using molecular dynamics (MD) simulation. MD simulation was performed using COMPASS forcefield under the isothermal-isobaric (i.e., NPT) ensemble, where N is the number of atoms, P is the pressure, and T is the temperature.[17] The temperature and pressure were maintained at 298 K and atmospheric pressure using a Berendsen thermostat and barostat.[18] The cutoff distance of the van der Waals interaction was set to 12.5 Å, and the electrostatic interactions were calculated using the Ewald summation method with an accuracy of 10^{-5} kcal/mol. The time step was set to 1 fs, and the total simulation time was 2 ns. The EDA–EDT mixture solvent was considered to contain 60 EDA molecules and 6 EDT molecules (i.e., 10:1 vol) in a 20 Å cubic box, and the equilibrated density was 0.92 g/cc. From the last configuration of MD simulation, one EDT molecule and surrounding molecules within 3 Å around the EDT were selected for calculating the energy of proton transfer as EDA−EDT cluster, which contained the 8 EDA molecules and 2 EDT molecules (**Figure 4.3**).

To carry out theoretical DFT calculations of the dissolution mechanism on GeS_2, a slab model consisting of two atomic layers of GeS_2 with the (001) surface of the experimental structure determined by the XRD measurement (**Figure 4.4a**) was employed. The top layer of the model system was relaxed, while the bottom layer was fixed to represent the bulk phase during the optimization calculation. The vacuum region of the slab model was set to ≈30 Å for all slab models to avoid self-interaction errors. When a deprotonated EDT molecule was added near the GeS_2 slab region, protonated EDA was also added to the vacuum region for charge balance (**Figure 4.4b**). Note that when two or more protonated EDAs were in the vacuum area, the distances between protonated EDAs were maximized to prevent them from reacting.
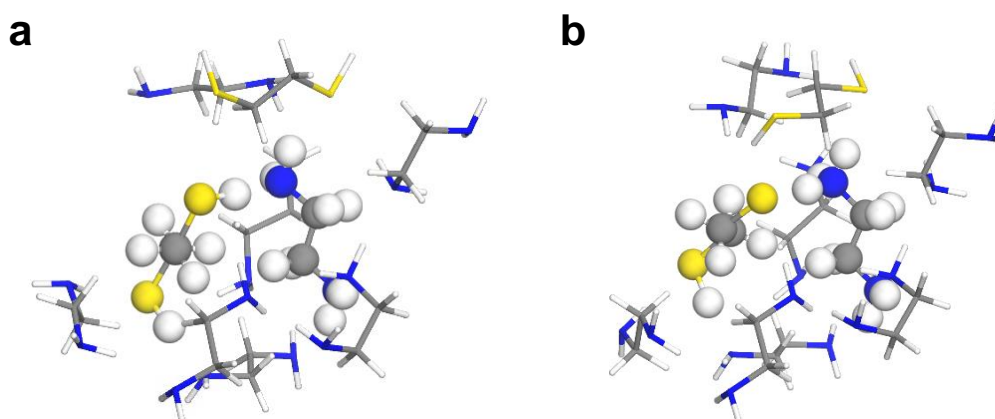
Figure 4.3 The EDA−EDT (10:1 vol.) mixture solvent modeled using molecular dynamics simulation. Molecules within 3 Å around the EDT in the relaxed structure were selected. DFT optimized structure of EDA−EDT mixture (a), first proton transferred EDA−EDT mixture (b). For the clear view, proton transferred EDT and EDA molecules are depicted using the ball-and-stick model, and other molecules are depicted using the stick model. In the color scheme, C, S, N, and H atoms are colored grey, yellow, blue, and white, respectively.
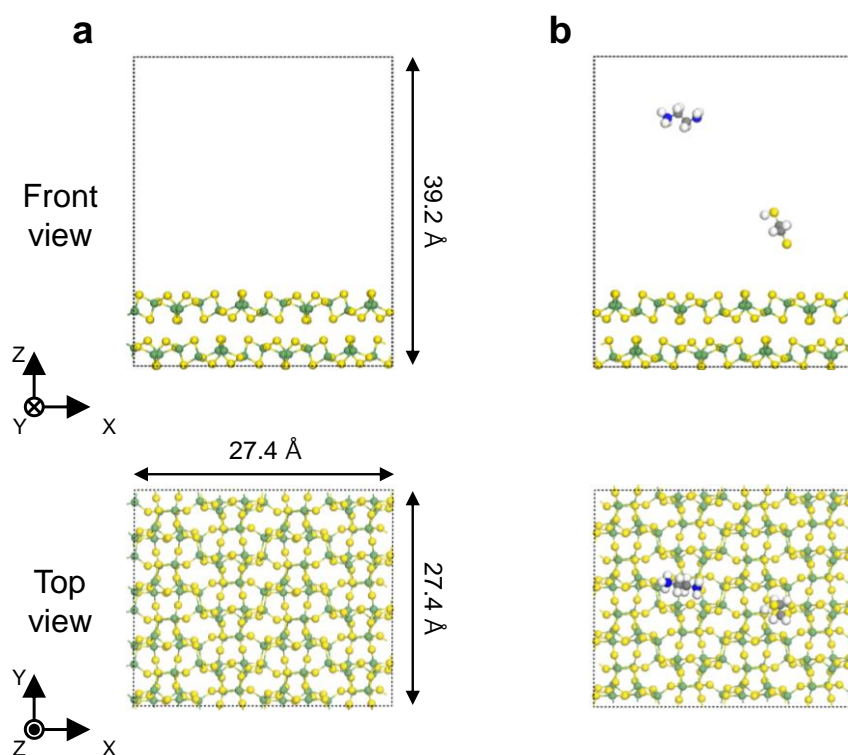
Figure 4.4 (a) DFT calculation model for the GeS$_2$ slab with (001) surface. (b) Optimized configuration of protonated EDA and deprotonated EDT on the GeS$_2$ surface. For the clear view, Ge, C, S, N, and H atoms are colored green, grey, yellow, blue, and white, respectively.

4.3 Result and Discussion

To identify the dissolving ability of EDA−EDT binary solvent mixtures, we examined the proton transfer in the EDA−EDT mixture solution and the dissolution mechanism of GeS$_2$ in EDA−EDT using theoretical calculations. The EDA−EDT (10:1 vol) mixture solvent modeled using molecular dynamics simulation was used to check the probability of proton transfer in the mixture solution. The proton transfer energy from EDT to EDA in molecules within 3 Å around the EDT in the relaxed solvent structure was calculated to be −0.61 eV through DFT calculations. From these results, we revealed that the thiolate anion could be readily formed via proton transfer from EDT to EDA. In addition, the molecular electrostatic potential map reveals that the deprotonated EDT has the point of nucleophilic attack, which is the deprotonated thiolate anion.[19] (**Figure 4.5**)

a   **b**

0.30e

-0.24e
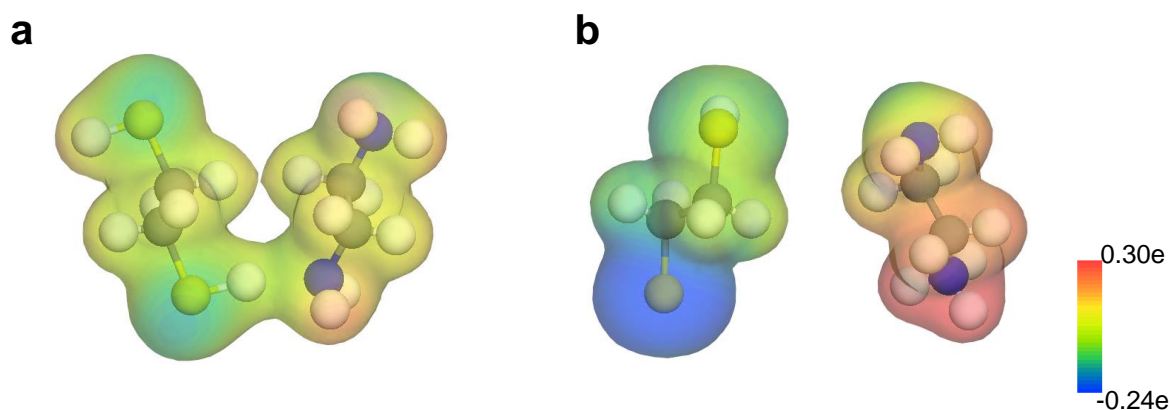
Figure 4.5 DFT optimized structure and molecular electrostatic potential (MEP) map of EDA−EDT mixture (a), and proton transferred EDA−EDT mixture (b). The MEP map indicates the reactive site in molecules, where the electron distribution effect is significant. Blue represents the negative regions while red represents the positive regions of MEP. For the clear view, C, S, N, and H atoms are colored grey, yellow, blue, and white, respectively.

Furthermore, to elucidate the mechanism of the dissolution reaction of the GeS$_2$ crystal, we traced the step-by-step pathway in dissociating the Ge−S bond in the GeS$_2$ surface caused by thiolate anions. (**Figures 4.6**, and **4.7**) The pathway of GeS$_2$ dissolution was assumed to gradually dissociate the Ge−S bond in GeS$_2$ via the nucleophilic attack of thiolate anions. It should be noted that in the first step, the thiolate anion was adsorbed on the uncoordinated Ge site on the GeS$_2$ surface, and the Ge−S bond on the GeS$_2$ surface was dissociated with no activation energy (E_a). In the subsequent reaction, the additional deprotonated EDT was continuously attached to the Ge site exposed on the surface,

dissociating the bond between Ge and sulfur on the surface. To describe the reaction mechanism in more detail, In the first step, when the thiolate anion was adsorbed on an uncoordinated Ge site (G_1 site) on the GeS_2 surface, one Ge−S bond between G_1 and surface sulfur connected with G_1 atom and another Ge atom (G_2 site) and placed on opposite with EDT anion was dissociated with no activation energy (E_a), indicating that the thiolate anion is a strong nucleophilic attacker (i.e., from IS to IS_{ad}). The heat of reaction (ΔE) for the adsorption of the EDT anion and dissociation of the Ge−S bond was −1.28 eV. At the first intermediate step (IM1), after new EDT anion was added near the surface, the thiolate anion was adsorbed at the G_1 site and dissociated the second Ge−S bond between G_1 and surface sulfur connected with G_1 atom and other Ge atom (not G_2 site), with an activation energy of 0.10 eV and heat of reaction of −0.74 eV. Subsequently, the third Ge−S bond between G_1 and surface sulfur atom connected between G_1 and other Ge (not G_2 site) was detached from the G_1 atom and reconnected the initially dissociated Ge−S bond, forming the structure G_1−S_2−G_2 (i.e., from IM1 to IM2) with an activation energy of 0.49 eV and heat of reaction of 0.28 eV. The subsequent reaction step proceeded in the same manner as in the previous steps. At the IM3 step, the added thiolate anion was adsorbed on the uncoordinated Ge site (G_3 site) near the G_2 site and broke down the G_3−S bond. However, unlike the previous thiolate adsorption step, this reaction had a low activation energy of 0.08 eV due to the change in the surface structure, and the heat of reaction was −0.89 eV. The fourth thiolate anion was then introduced and adsorbed onto the G_3 site, and the Ge−S bond between G_3 and S on the surface was dissociated with an activation energy of 0.48 eV and heat of reaction of 0.19 eV from IM3 to IM4. And lastly, the structure in the final state was formed via surface reconstruction in the same manner as the process from IM1 to IM2. Among the Ge atoms connected to G_3 through Ge–S bonds, Ge atoms (i.e., not from G_2) were separated from the sulfur bonded between G_3 and the Ge atom, and the sulfur atom was attached to G_2, forming the G_3−S_2−G_2 structure. In this reaction, the activation energy was 0.58 eV, and heat of reaction was 0.14 eV (i.e., from IM4 to FS). Finally, the product was a (thiolate)$_2$−G_1−S_2−G_2−S_2−G_3−(thiolate)$_2$ structure and completely dissolved from the GeS_2 surface. Importantly, the total GeS2 dissolution mechanism via the nucleophilic attack of the thiolate anion requires a low activation energy, indicating that the Ge−S cluster could be easily formed. This mechanistic calculation suggested a plausible formation of polyanionic Ge−S clusters through a continuous dissolution reaction.
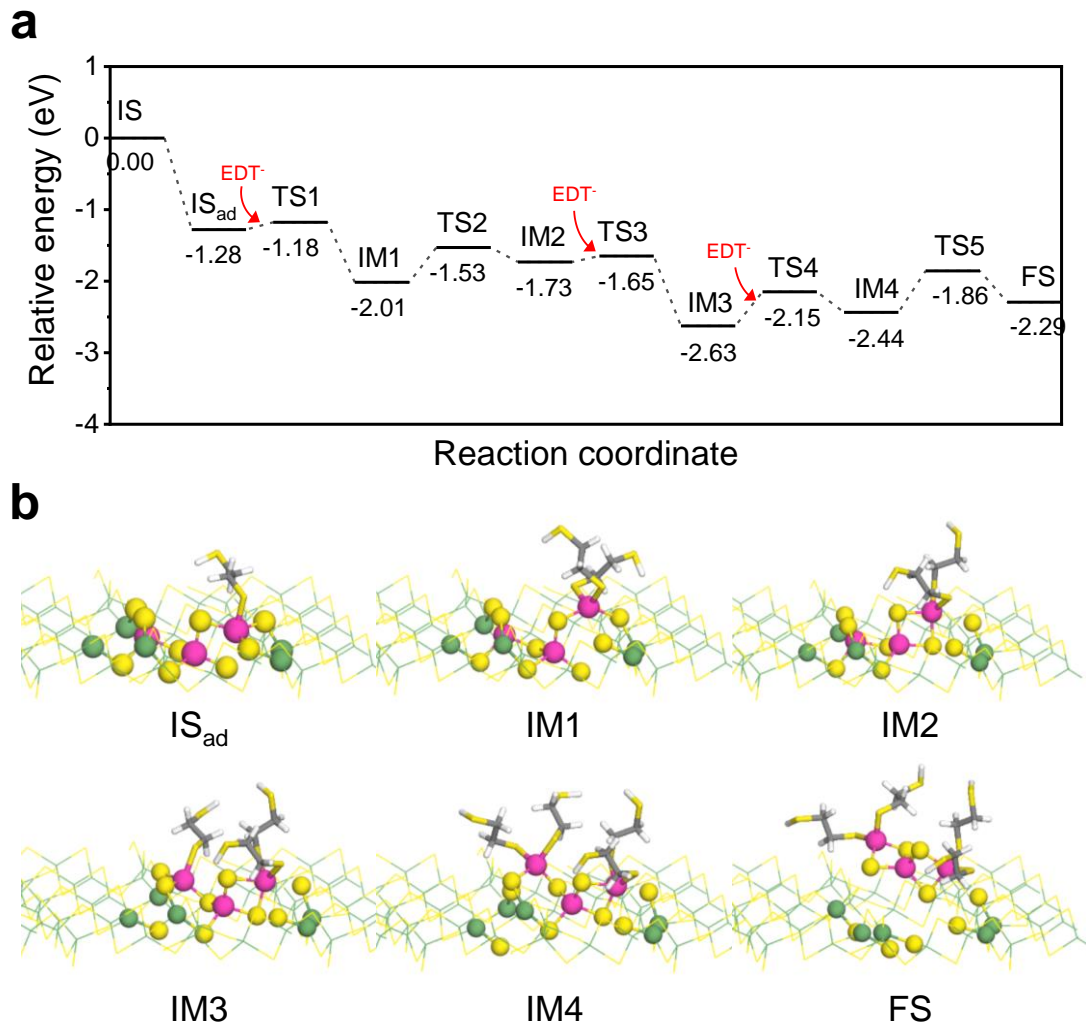
Figure 4.6 Dissolution mechanism of sulfide SE precursors in EDA−EDT cosolvents. (a) Reaction coordinates of dissolution mechanism of the GeS$_2$ surface. (b) Magnified view of the optimized configurations of each state. In (b), IS, IM, TS, and FS in each reaction mechanism represent initial state, intermediate, transition state, and final state, respectively. For the clear view, the dissolved Ge atoms and surface atoms near the Ge atoms are depicted using the ball-and-stick model, and the deprotonated EDT molecules are depicted using the stick model. The remaining atoms are indicated as lines. The dissolved three Ge atoms are colored pink, and the remaining Ge, C, S, N, and H atoms are colored green, gray, yellow, blue, and white, respectively
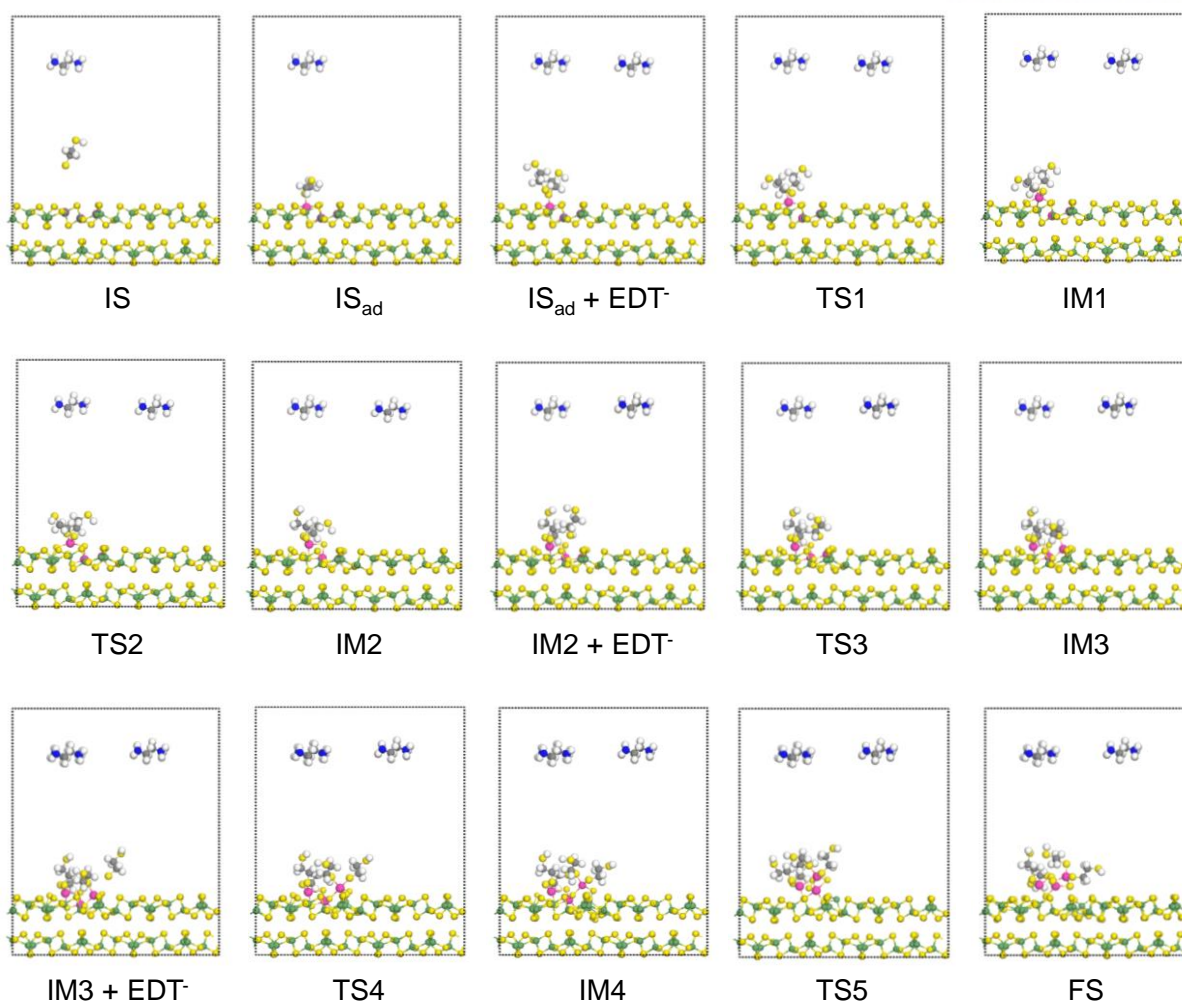
Figure 4.7 Front view of configurations of the reaction state of the dissolution mechanism of GeS$_2$ surface. IS, IM, TS, and FS in each reaction mechanism represent Initial State, Intermediate, Transition State, and Final State, respectively. For the clear view, dissolved three Ge atoms are colored pink and the remaining Ge, C, S, N, and H atoms are colored green, grey, yellow, blue, and white, respectively.

Likewise, the dissociation of P$_2$S$_5$, Li$_2$S, and Na$_2$S by EDT$^-$ were also favorable according to the dissolution reaction mechanism. From the structural results observed in the experiment, the P$_2$S$_5$, modeled a P$_4$S$_{10}$ cluster, and the Li$_2$S and Na$_2$S used the (100) slab model of cubic structure. In the results, note that the thiolate was attached to the other sulfides without activation energy in the initial reaction, indicating that the dissolution could be facilitated by the nucleophilic attack. As shown **Figure 4.8**, in the case of the dissolution mechanism of the P$_4$S$_{10}$ cluster, when the first thiolate was attached to the P atom of the P$_4$S$_{10}$ cluster, the P−S bond of the cluster was dissociated with a heat of reaction (ΔE) of −0.61 eV. In subsequent step, as the second thiolate was also attached to the same P atom, the P−S bond of P$_4$S$_{10}$ cluster was broken again. The activation energy (E_a) and ΔE corresponding to the reaction

from IM1 to IM2 were 0.24 and −1.81 eV. After then, the added third thiolate was reacted in the same pathway to form P−S(thiolate)$_3$ product with the E_a of 0.15 eV and ΔE of −1.08 eV. For the Li$_2$S, and Na$_2$S (100) surface, the dissolution mechanisms in the two sulfide layers were calculated until the stage where the cation was detached from the each surface. In the first step of dissolution mechanism of Li$_2$S surfaces, firstly and secondly added thiolates were adsorbed continuously around one Li$^+$ in the surface without activation energy. (**Figure 4.9**) The adsorption energies of first and second thiolate were −0.53 and −0.41 eV. Subsequently, after third thiolate was added on the surface, the Li$^+$ which connected with two thiolates was lifted slightly from surface, forming the Li−S bond between Li$^+$ and third thiolate with the E_a of 0.58 eV and ΔE of −0.32 eV. Finally, the Li-thiolate complex with the tetrahedral form was produced when Li$^+$ was completely desorbed on the surface by the fourth added thiolate. The E_a and ΔE corresponding to the reaction were 0.60 and 0.29 eV. The dissolution mechanism of Na$_2$S surface had the same route with that of the Li$_2$S surface. (**Figure 4.10**) The adsorption energies of first and second thiolate around the one Na$^+$ in the Na$_2$S surface were −0.43 and −0.62 eV, respectively. In subsequent step, thirdly added thiolate was adsorbed at the Na$^+$ in the surface with the E_a of 0.22 eV and ΔE of −0.10 eV. Finally, the Na$^+$ was dissolved from the Na$_2$S surface by the additional thiolate, forming the Na-thiolate complex as the product with the E_a of 0.51 eV and ΔE of −0.14 eV. In conclusion, the low activation energies of each dissolution mechanism of sulfides SE precursors such as the Na$_2$S, Li$_2$S, and P$_2$S$_5$ as well as GeS$_2$ suggest that they could be dissolved by the nucleophilic attack of the EDT anions.

a

b

IS   IM1   IM1+EDT⁻   TS1

IM2   IM2+EDT⁻   TS2   FS
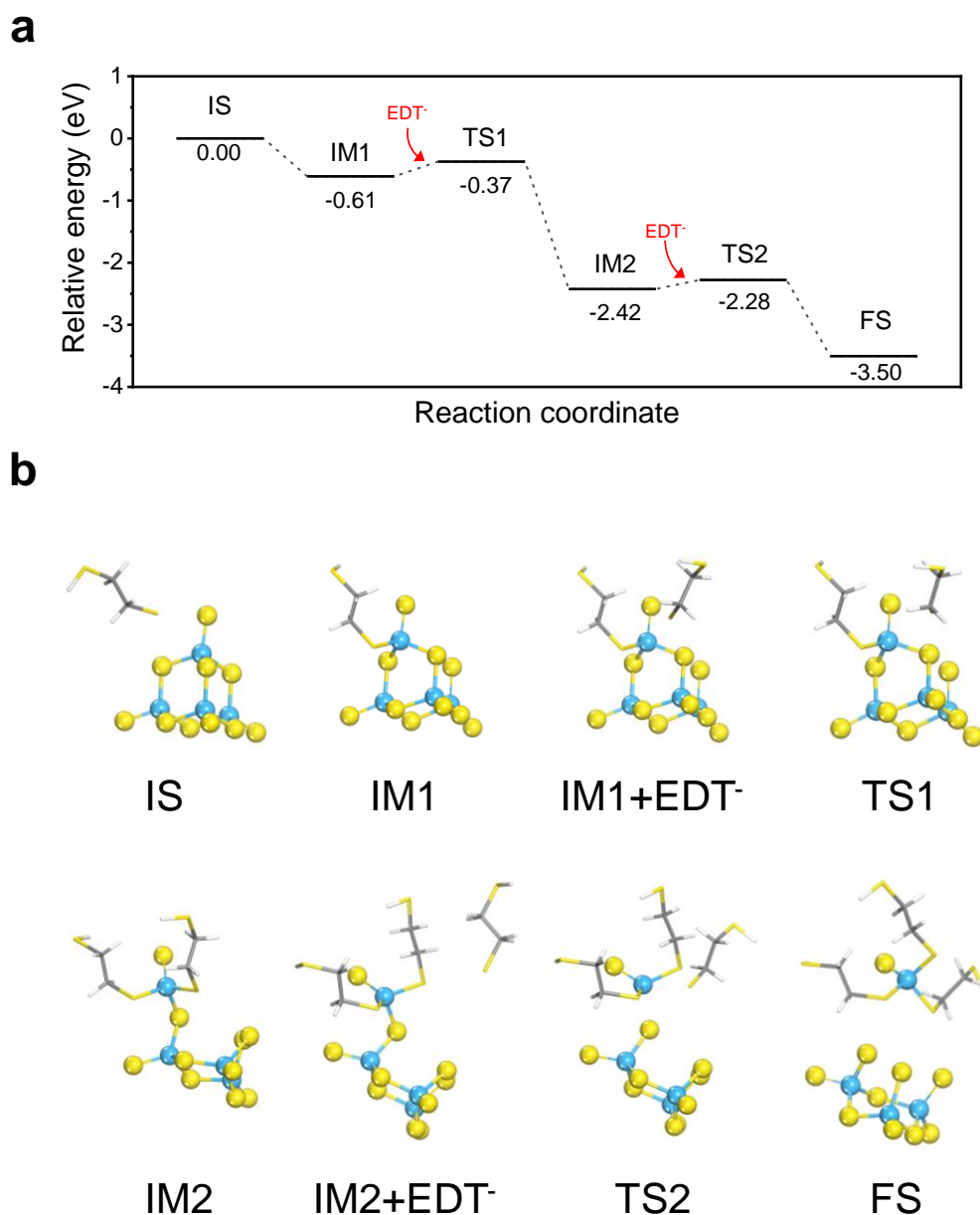
Figure 4.8 Dissolution mechanism of P_4S_{10} sulfide cluster in EDA−EDT cosolvents. (a) Reaction coordinates of dissolution mechanism of the P_4S_{10} sulfide cluster. (b) the optimized configurations of each state. In (b), IS, IM, TS, and FS in each reaction mechanism represent Initial State, Intermediate, Transition State, and Final State, respectively. For the clear view, thiolate molecules are depicted using the stick model, and P_4S_{10} cluster are shown by the ball-and-stick model. The P, C, S, and H atoms are colored in sky blue, grey, yellow, and white, respectively.
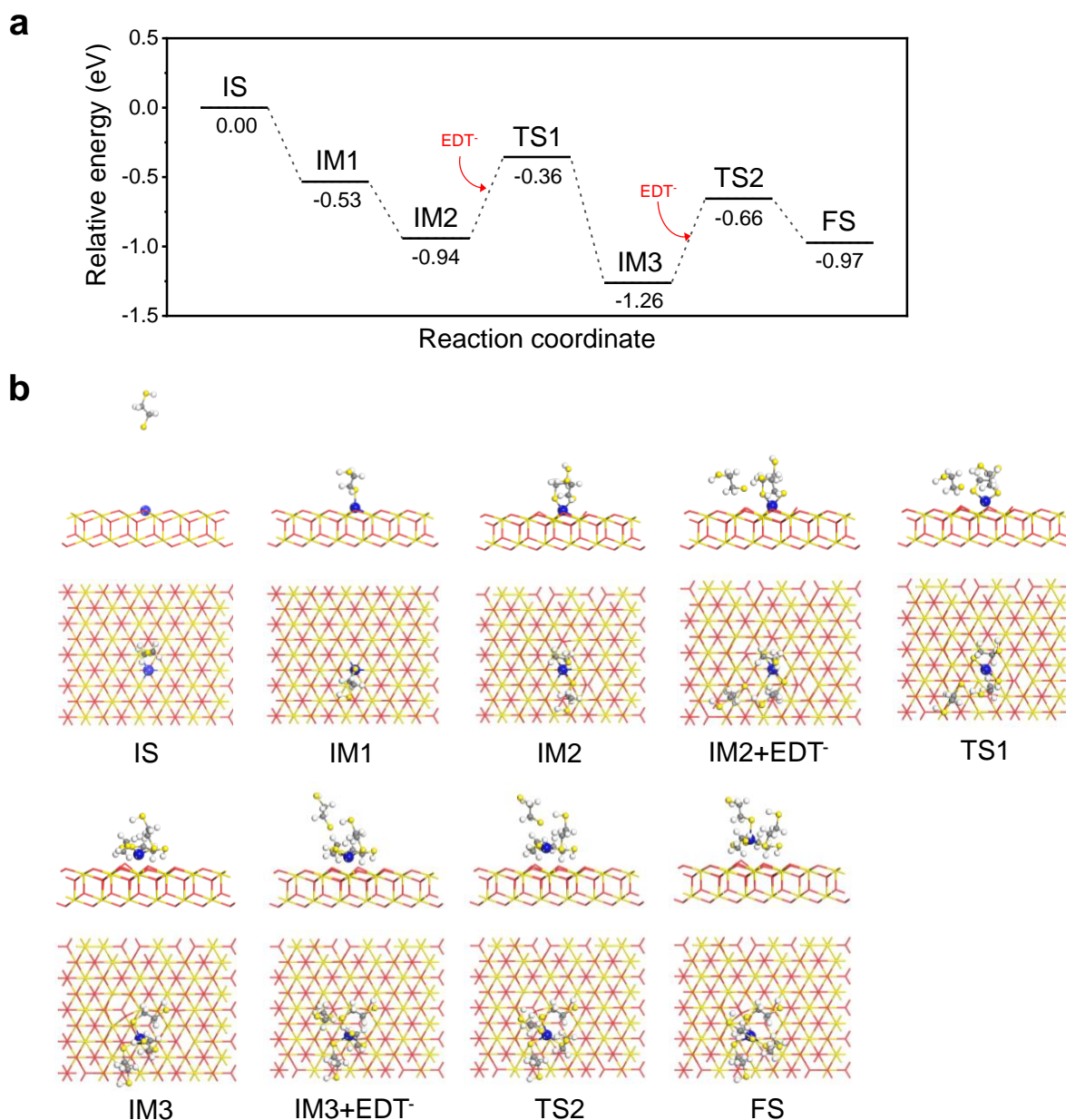
Figure 4.9 Dissolution mechanism of Li₂S sulfide surface in EDA−EDT cosolvents. (a) Reaction coordinates of dissolution mechanism of the Li₂S surface. (b) the optimized configurations of each state. In (b), IS, IM, TS, and FS in each reaction mechanism represent Initial State, Intermediate, Transition State, and Final State, respectively. For the clear view, thiolate molecules and dissolved Li atom are depicted using the ball-and-stick model, and atoms in the Li₂S surface are shown by the stick model. The dissolved Li atom is colored in blue, remaining Li, C, S, and H atoms are colored in red, grey, yellow, and white, respectively.

60
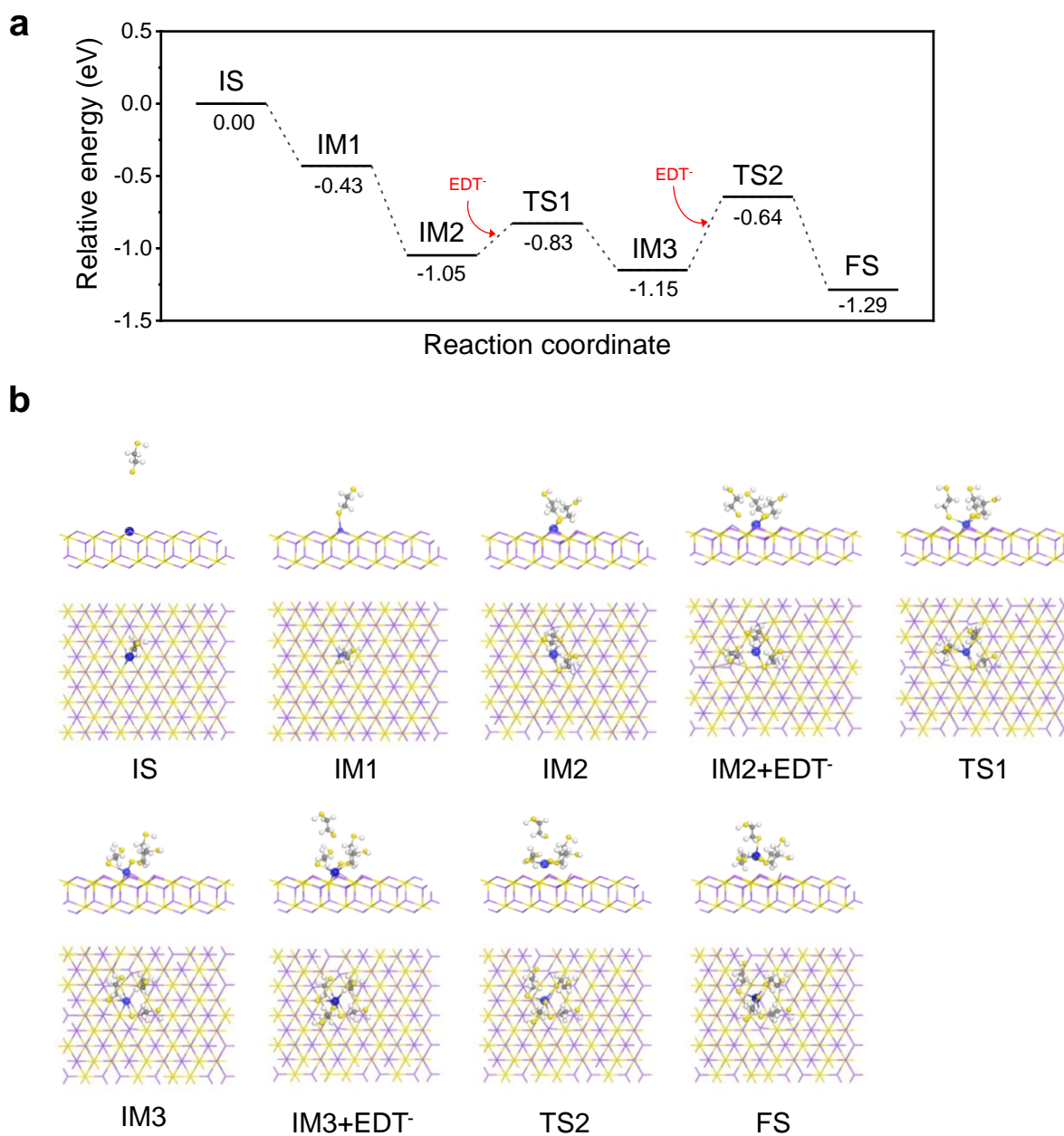
Figure 4.10 Dissolution mechanism of Na_2S sulfide surface in EDA−EDT cosolvents. (a) Reaction coordinates of dissolution mechanism of the Na_2S surface. (b) the optimized configurations of each state. In (b), IS, IM, TS, and FS in each reaction mechanism represent Initial State, Intermediate, Transition State, and Final State, respectively. For the clear view, thiolate molecules and dissolved Na atom are depicted using the ball-and-stick model, and the atoms in the Na_2S surface are shown by the stick model. The dissolved Na atom is colored in blue, remaining Na, C, S, and H atoms are colored in purple, grey, yellow, and white, respectively.

4.4 Conclusion

In summary, we demonstrated the first universal solution synthesis for sulfide SEs using EDA−EDT and EDA−EDT alkahests. The exceptional dissolving power of EDA−EDT for not only conventional precursors (Li_2S, P_2S_5, LiX, and Na_2S) but also metal sulfides, such as GeS_2, and its ability to form homogeneous solutions allowed for the facile synthesis of various classes of sulfide SEs. The dissolution mechanism of GeS_2 in EDA−EDT was revealed using DFT calculation. Specifically, the thiolate anions formed in the EDA−EDT solvent system dissociated metal sulfides via nucleophilic attack, forming polyanionic solutes. We expect that our results will open new opportunities for the scalable synthesis and discovery of new soft-chemistry-guided superionic conductors for ASSBs.

4.5 Reference

1. Lee, J. E.; Park, K.-H.; Kim, J. C.; Wi, T.-U.; Ha, A. R.; Song, Y. B.; Oh, D. Y.; Woo, J.; Kweon, S. H.; Yeom, S. J.; Cho, W.; Kim, K. S.; Lee, H.-W.; Kwak, S. K.; Jung, Y. S. *Advanced Materials* **2022**, 34, 2200083.

2. a) Janek, J.; Zeier, W. G. *Nat. Energy* **2016**, 1, 16141; b) Zhang, Z.; Shao, Y.; Lotsch, B.; Hu, Y.-S.; Li, H.; Janek, J.; Nazar, L. F.; Nan, Maier, C. J.; Armand, M.; Chen, L. *Energy Environ. Sci.* **2018**, 11, 1945; c) Manthiram, A.; Yu, X.; Wang, S. *Nat. Rev. Mater.* **2017**, 2, 16103; d) Pfenninger, R. M. Struzik, R. ; Garbayo, R. ; Stilp, E.; Rupp, J. L. M. *Nat. Energy* **2019**, 4, 475; e) Famprikis, T.; Canepa, P.; Dawson, J. A. Islam, M. S. Masquelier, C. *Nat. Mater.* **2019**, 18, 1278; f) Chen, R. Li, Q.; Yu, X.; Chen, L.; Li, H. *Chem. Rev.* **2020**, 120, 6820; g) Xiao, Y. H.; Wang, Y.; Bo, S. H.; Kim, J. C.; Miara, L. J.; Ceder, G. *Nat. Rev. Mater.* **2020**, 5, 105; h) Zhu, Y.; Mo, Y. *Angew. Chem., Int. Ed.* **2020**, 59, 17472; i) Lewis, J. A.; Cortes, F. J. Q.; Liu, Y.; Miers, J. C.; Verma, A.; Vishnugopi, B. S.; Tippens, J. Prakash, D. Marchese, T. S. Han, S. Y.; Lee, C.; Shetty, P. P.; Lee, H.-W.; Shevchenko, P.; Carlo, F. D.; Saldana, C.; Mukherjee, P. P.; McDowell, M. T.; *Nat. Mater.* **2021**, 20, 503; j) Ning, Z.; Jolly, D. S.; Li, G.; Meyere, R. D.; Pu, S. D.; Chen, Y.; Kasemchainan, J.; Ihli, J.; Gong, C.; Liu, B.; Melvin, D. L. R.; Bonnin, A.; Magdysyuk, O.; Adamson, P.; Hartley, G. O.; Monroe, C. W.; Marrow, T. J.; Bruce, P. G. *Nat. Mater.* **2021**, 20, 1121; k) Xiao, Y. R.; Turcheniuk, K.; Narla, A.; Song, A. Y.; Ren, X. L.; Magasinski, A.; Jain, A.; Huang, S.; Lee, H.; Yushin, G. *Nat. Mater.* **2021**, 20, 984; l) Duchene, L.; Remhof, A.; Hagemann, H.; Battaglia, C. *Energy Storage Mater.* **2020**, 25, 782; m) Kwak, H.; Han, D.; Lyoo, J.; Park, J.; Jung, S. H.; Han, Y.; Kwon, G.; Kim, H.; Hong, S.-T.; Nam, K.-W.; Jung, Y. S. *Adv. Energy Mater.* **2021**, 11, 2003190; n) Han, Y.; Jung, S. H.; Kwak, H.; Jun, S.; Kwak, H.; Lee, J. H.; Hong, S.-T.; Jung, Y. S. *Adv. Energy Mater.* **2021**, 11, 2100126.

3. 2022, Solid state batteries can further boost climate benefits of EVs – study, © 2022 European Federation for Transport and Environment AISBL.

4. Kamaya, N.; Homma, K.; Yamakawa, Y.; Hirayama, M.; Kanno, R.; Yonemura, M.; Kamiyama, T.; Kato, Y.; Hama, S.; Kawamoto, K.; Mitsui, A. *Nat. Mater.* **2011**, 10, 682.

5. Adeli, P.; Bazak, J. D.; Park, K. H.; Kochetkov, I.; Huq, A.; Goward, G. R.; Nazar, L. F. *Angew. Chem. Int. Ed.* **2019**, 58, 8681.

6. a) Park, K. H.; Bai, Q.; Kim, D. H.; Oh, D. Y.; Zhu, Y.; Mo, Y.; Jung, Y. S. *Adv. Energy Mater.* **2018**, 8, 1800035; b) Miura, A.; Rosero-Navarro, N. C.; Sakuda, A.; Tadanaga, K.; Phuc, N. H. H.; Matsuda, A.; Machida, N.; Hayashi, A.; Tatsumisago, M. *Nat. Rev. Chem.* **2019**, 3, 189.

7. a) Wang, Y.; Lu, D.; Bowden, M.; El Khoury, P. Z.; Han, K. S.; Deng, Z. D.; Xiao, J.; Zhang, J.-G.; Liu, J. *Chem. Mater.* **2018**, 30, 990; b) Calpa, M.; Rosero-Navarro, N. C.; Miura, A.; Terai, K.; Utsuno, F.; Tadanaga, K.; *Chem. Mater.* **2020**, 32, 9627.

8. a) Rangasamy, E.; Liu, Z.; Gobet, M.; Pilar, K.; Sahu, G.; Zhou, W.; Wu, H.; Greenbaum, S.; Liang, C. *J. Am. Chem. Soc.* **2015**, 137, 1384; b) Yao, X.; Liu, D.; Wang, C.; Long, P.; Peng, G.; Hu, Y.-S.; Li, H.; Chen, L.; Xu, X. *Nano Lett.* **2016**, 16, 7148; c) Oh, D. Y.; Kim, D. H.; Jung, S. H.; Han, J.-G.; Choi, N.-S.; Jung, Y. S. *J. Mater. Chem. A* **2017**, 5, 20771.

9. a) Park, K. H.; Oh, D. Y.; Choi, Y. E.; Nam, Y. J.; Han, L.; Kim, J. Y.; Xin, H.; Lin, F.; Oh, S. M.; Jung, Y. S. *Adv. Mater.* **2016**, 28, 1874; b) Banerjee, A.; Park, K. H.; Heo, J. W.; Nam, Y. J.; Moon, C. K.; Oh, S. M.; Hong, S. T.; Jung, Y. S. *Angew. Chem., Int. Ed.* **2016**, 55, 9634; c) Yubuchi, S.; Teragawa, S.; Aso, K.; Tadanaga, K.; Hayashi, A.; Tatsumisago, M. *J. Power Sources* **2015**, 293, 941.

10. a) Kim, D. H.; Oh, D. Y.; Park, K. H.; Choi, Y. E.; Nam, Y. J.; Lee, H. A.; Lee, S. M.; Jung, Y. S. *Nano Lett.* **2017**, 17, 3013; b) Kim, D. H.; Lee, Y.-H.; Song, Y. B.; Kwak, H.; Lee, S.-Y.; Jung, Y. S. *ACS Energy Lett.* **2020**, 5, 718.

11. a) Han, F. D.; Yue, J.; Fan, X. L.; Gao, T.; Luo, C.; Ma, Z. H.; Suo, L. M.; Wang, C. S. *Nano Lett.* **2016**, 16, 4521; b) Li, X.; Liang, J.; Yang, X.; Adair, K. R.; Wang, C.; Zhao, F.; Sun, X. *Energy Environ. Sci.* **2020**, 13, 1429; c) Wan, H.; Mwizerwa, J. P.; Qi, X.; Liu, X.; Xu, X.; Li, H.; Hu, Y.-S.; Yao, X. *ACS Nano* **2018**, 12, 2809.

12. a) Lim, H.-D.; Yue, X.; Xing, X.; Petrova, V.; Gonzalez, M.; Liu, H.; Liu, P.; *J. Mater. Chem. A* **2018**, 6, 7370; b) Teragawa, S.; Aso, K.; Tadanaga, K.; Hayashi, A.; Tatsumisago, M. *J. Mater. Chem. A* **2014**, 2, 5095; c) Lim, H.-D.; Lim, H.-K.; Xing, X.; Lee, B.-S.; Liu, H.; Coaty, C.; Kim, H.; Liu, P.; *Adv. Mater. Interfaces* **2018**, 5, 1701328; d) Ito, A.; Kimura, T.; Sakuda, A.; Tatsumisago, M.; Hayashi, A.; *J. Sol-Gel Sci. Technol.* **2021**, 101, 2; e) Subramanian, Y.; Rajagopal, R.; Ryu, K.-S. *Scr. Mater.* **2021**, 204, 114129.

13. a) Delley, B.; *J. Chem. Phys.* **1990**, 92, 508; b) Delley, B.; *J. Chem. Phys.* **2000**, 113, 7756.

14. Perdew, J. P.; Burke, K.; Ernzerhof, M. *Phys. Rev. Lett.* **1996**, 77, 3865.

15. a) Klamt, A. Schüürmann, G. *J. Chem. Soc., Perkin Trans.* **1993**, 2, 799; b) Looyenga, H. *Physica* **1965**, 9, 501.

16. a) Bell, S.; Crighton, J. S.; *J. Chem. Phys.* **1984**, 80, 2464; b) Halgren, T. A.; Lipscomb, W. N. *Chem. Phys. Lett.* **1977**, 49, 225.

17. Sun, H.; Ren, P.; Fried, J. R. *Comput. Theor. Chem.* **1998**, 8, 229.

18. Samoletov, A. A.; Dettmann, C. P.; Chaplain, M. A. J. *J. Stat. Phys.* **2007**, 128, 1321.

19. Northrop, B. H.; Frayne, S. H.; Choudhary, U. *Polym. Chem.* **2015**, 6, 3415.

Chapter 5. Universal Solution Synthesis of Sulfide Solid Electrolytes Using Alkahest for All-Solid-State Batteries

5.1 Introduction

Calcium hydroxide ($Ca(OH)_2$) reacts with CO_2 and SO_2 due to its strong basic nature.[2] The basicity and poor solubility of $Ca(OH)_2$ are effectively attributes for the development of applications in various fields, such as medical, chemical, environmental, and architectural industries. These applications of $Ca(OH)_2$ include the uses in antibacterial agents, sewage treatment, capture and storage of greenhouse gases, and cement.[3–6] The carbonation process of $Ca(OH)_2$ is essential for controlling the extent of increase in the hardness and expansion of cement, for stable storage of CO_2 and radioactive waste, and is used in the paper and paint industries for the synthesis of calcium carbonate by precipitation.[7–13] However, because the carbonation reaction can only occur in aqueous solutions, in-depth understanding of the $Ca(OH)_2$ carbonation reaction mechanism under aqueous conditions is essential.

Previous studies on the carbonation of $Ca(OH)_2$ pursued kinetic approaches to the problem.[14–16] Van Balen et al. reported that the dissolution of $Ca(OH)_2$ and the adsorption of water on its surface are important factors in the carbonation reaction of $Ca(OH)_2$.[14] Bausach et al. revealed that the exposure of a single crystal-phase of $Ca(OH)_2$ to water vapor results in the acceleration of the reaction between $Ca(OH)_2$ and SO_2 due to its dissolution.[2] In addition, Nikulshina et al. reported a kinetic model for the $Ca(OH)_2$ carbonation reaction rate by considering the reaction at the interface with water molecules or OH^-, and found that the reaction took place only on the $Ca(OH)_2$ surface which was not covered by calcium carbonate.[15] Recently, density functional theory (DFT) calculations showed that the adsorbed water molecules can significantly lower reaction barriers and partially stabilize the products of the carbonation reaction.[16] The aforementioned studies conducted kinetic treatments of the $Ca(OH)_2$ and CO_2 carbonation reaction through the dissolution of $Ca(OH)_2$. In addition, the effect of water on the carbonation reaction was interpreted by the interaction between water and calcium carbonate.[17,18] To date, the initial reaction due to the interaction between $Ca(OH)_2$ and water and its effect on the carbonation reaction have not been studied in detail. Considering that the strong basic properties of

Ca(OH)$_2$ can be expressed through contact with water, the prerequisite for clearly understanding the carbonation reaction of Ca(OH)$_2$ is to obtain information on the initial interaction between Ca(OH)$_2$ and water. However, observation of the Ca(OH)$_2$ and water interactions in the initial stages of the widely known calcium carbonate synthesis via supercritical CO$_2$−mediated precipitation by the rapid reaction of CO$_2$ and water, is highly challenging.[19,20] Thus, to fully understand the carbonation reaction mechanism in aqueous solutions, an experimental design that slowly induces the carbonation reaction is necessary to observe the changes due to the interaction between Ca(OH)$_2$ and water.

In this study, a slow carbonation reaction between CO$_2$ dissolved in water and Ca(OH)$_2$ was induced under ambient conditions. (**Figure 5.1**) In the experimental data, X-ray diffraction (XRD) was observed changes in the Ca(OH)$_2$ crystal lattice during the Ca(OH)$_2$ and water mixing, and the intercalation of the water molecules in the Ca(OH)$_2$ interlayers (**Figures 5.2** and **5.3**) was further confirmed by the nuclear magnetic resonance (NMR) results. Therefore, we performed theoretical calculations at the atomistic level, which revealed that water can form the most stable intercalated system among the other chemical species that may appear in the carbonation process and that the water molecules can intercalate into the (100) surface to increase the [001] interlayer distance of Ca(OH)$_2$. In addition, DFT calculations clearly demonstrated the difference in the carbonation reaction mechanism of Ca(OH)$_2$ due to the interaction between Ca(OH)$_2$ and water. To the best of our knowledge, this is the first study which reveals the water-intercalated Ca(OH)$_2$ structure through a combination of experiments and theoretical calculations at the atomistic level. The learnings from this study of the initial reaction due to the interaction between Ca(OH)$_2$ and water, are expected to advance CO$_2$ conversion technologies and the building materials industry.
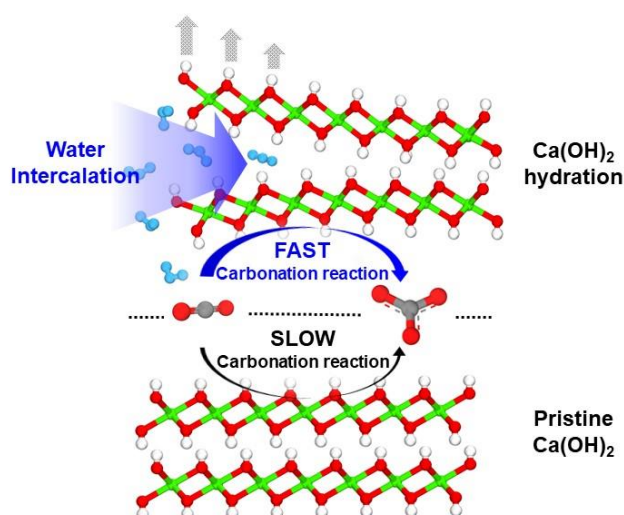
Figure 5.1 Schematic illustration of swelling process by water intercalation which affects carbonation reaction. Water molecules, Ca, O, C, and H are colored as light blue, green, red, gray, and white, respectively.
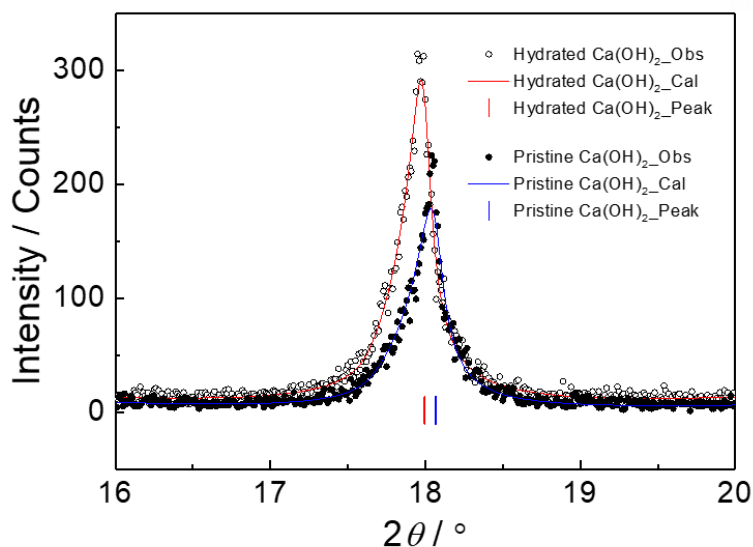
Figure 5.2 XRD analysis of pristine and hydrated $Ca(OH)_2$ with (001) Bragg peak positions. The sample of hydrated $Ca(OH)_2$ was prepared via mixing with water for an hour at ambient condition. The vertical bars were indicated as the peak position of (001) facet and the pristine and hydrated $Ca(OH)_2$ samples were represented by blue and red, respectively.
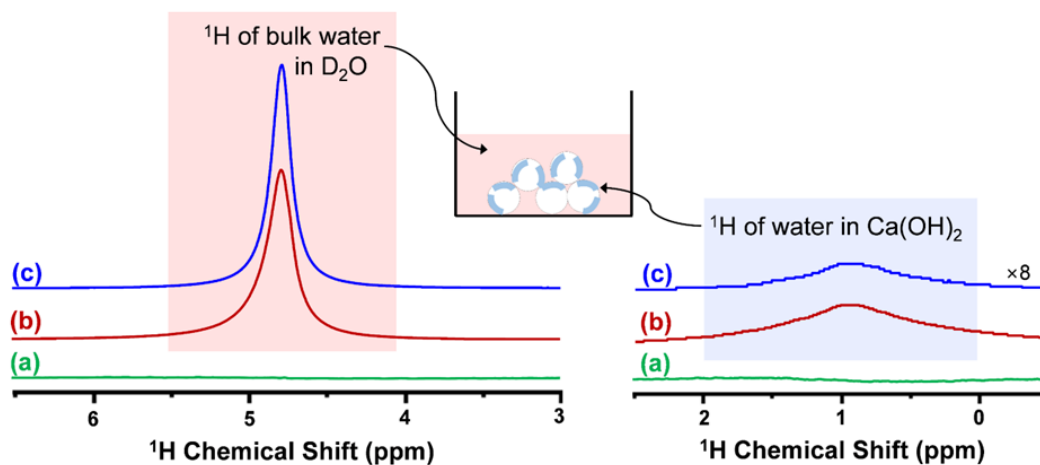
Figure 5.3 ^{1}H MAS NMR spectra of (a) pristine $Ca(OH)_2$, (b) hydrated $Ca(OH)_2$, and (c) $Ca(OH)_2$ reacted with [13]CO_2 dissolved in D2O. All sample were analyzed 1 h after D_2O addition. In the case of (b), the weight of $Ca(OH)_2$ and D_2O were 49.46 and 12.77 mg, respectively. For clarity, intensity of the peak at 0.9 ppm was magnified 8-fold. The inset figure represents the schematic diagram of the experimental products including pristine $Ca(OH)_2$ (white), bulk water (pink), and water intercalated into $Ca(OH)_2$ (pale blue).

5.2 Computational Models and Methods

All DFT calculations were performed using the Dmol[3] program.[21,22] For the exchange-correlation energy, we used the generalized gradient approximation with the Perdew−Burke−Ernzerhof functional,[23] and applied the semi-empirical Tkatchenko−Scheffler (TS) method for dispersion correction.[24] All electron relativistic method was employed for core treatment. The spin-polarized calculations were conducted using the DNP 4.4 basis set. The Brillouin zone was integrated using a single k-point (Γ−point) grid with the Monkhorst−Pack scheme for (100) and (001) surface systems.[25] The convergence criteria for the geometry optimization were 1.0×10^{-5} Ha, 0.002 Ha/Å, and 0.005 Å for energy, force, and displacement, respectively. The self-consistent field convergence was less than 1.0×10^{-6} Ha, and the electron smearing value was set to 0.005 Ha. All DFT calculations were performed using the dielectric constant of water (*i.e.*, 78.54).[26] To determine the carbonation mechanism, we used the linear synchronous transit (LST) and quadratic synchronous transit (QST) methods until the convergence criterion of the root mean square (RMS) force was satisfied, which was set to 0.002 Ha/Å.[27,28]

To describe the interaction between the $Ca(OH)_2$ surface and water, all MD simulations were performed using ClayFF under the isothermal-isobaric (i.e., NPT) ensemble, where N is the number of atoms, P is the pressure, and T is the temperature.[29] The pressure and temperature were controlled at 0.0001 GPa and 298 K using the Parrinello−barostat and the Nosé−Hoover−Langevin (NHL) thermostat, respectively.[30,31] The cutoff distance of the van der Waals interaction was set to 12.5 Å, and the electrostatic interactions were calculated by the Ewald summation method with an accuracy of 10^{-5} kcal/mol. The time step was set to 1 fs, and the total simulation time length of the bulk and interface systems were 20 and 100 ns, respectively.

5.3 Result and Discussion

We performed DFT calculations to compare the stabilities of the intercalated systems as a function of the intercalated species. For the intercalated species, we considered the reactants or intermediates of carbonation reaction (i.e., H_2O, CO_2, Ca^{2+}, CO_3^{2-}, and HCO_3^{-}).[32] Because $Ca(OH)_2$ is periodically bonded along [100], [010], and [110] and forms a layered structure,[33] it is expected that the intercalated species can enter the space between the $Ca(OH)_2$ interlayers in the [001] direction rather than being inserted by breaking the bonds between Ca and O in the $Ca(OH)_2$ crystal structure. We calculated the formation energies depending on the intercalated species, as shown in **Figures 5.4** and **5.5**. Generally, the formation energies of the charged ions were higher than those of the neutral molecules, and the

larger was the size of the intercalated species, the higher was its formation energy. In addition, the interlayer distance tended to increase as the size of the intercalated species increased. Interestingly, for the water molecule, not only was the formation energy the lowest, but the interlayer distance was also the shortest even when the size of the water molecule was larger than that of Ca^{2+}. Due to hydrogen bonding interactions between water molecules and the OH groups in the $Ca(OH)_2$ interlayer, proton transfer occurred from water to $Ca(OH)_2$. Therefore, the water-intercalated system was optimized as H_2O bonded to Ca. This reaction is consistent with the proton-deuteron exchange reaction in the NMR results analyzed above. In addition, owing to the water intercalation, a slight increase in interlayer distance of hydrated $Ca(OH)_2$ (i.e., less than 1%) was observed compared to that of pristine $Ca(OH)_2$, which is consistent with the XRD peak shift analysis.
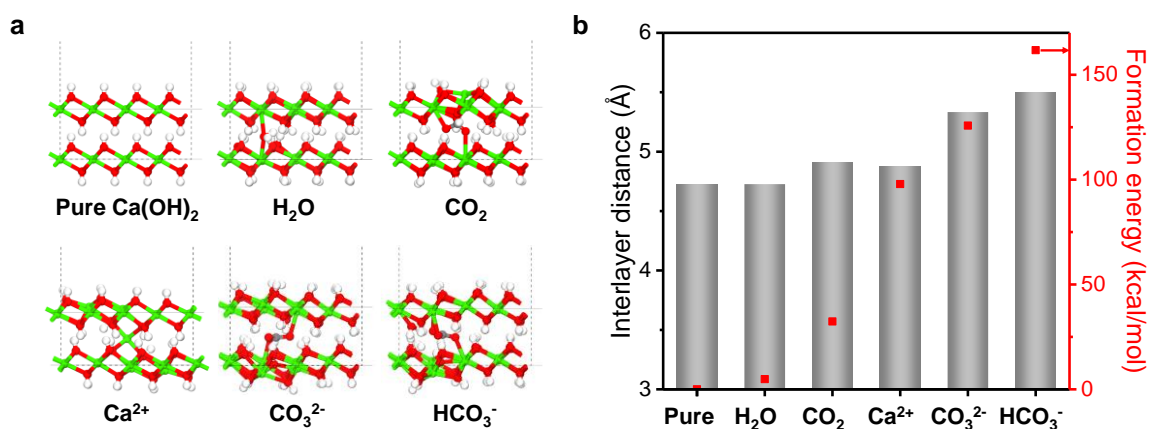
Figure 5.4 (a) Optimized structures of pristine and intercalated $Ca(OH)_2$ systems with various intercalated species. Ca, O, C, and H are colored green, red, gray, and white, respectively. (b) Interlayer distances (left axis) and formation energies (right axis) of intercalated $Ca(OH)_2$ systems as a function of intercalated species.
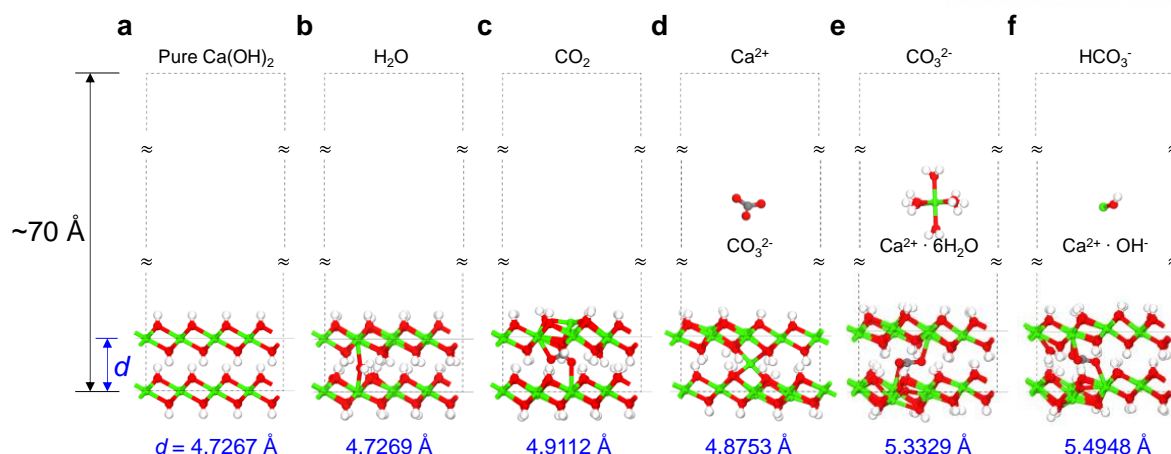
Figure 5.5 Optimized Ca(OH)₂ slab models. (a) Pristine Ca(OH)₂, (b) H₂O intercalated, (c) CO₂ intercalated, (d) Ca²⁺ intercalated, (e) CO₃²⁻ intercalated, and (f) HCO₃⁻ intercalated systems. Distances between Ca(OH)₂ interlayers are represented below in blue. Ca, O, C, and H are colored green, red, grey, and white, respectively.

To investigate the intercalation mechanism of water molecules, MD simulations were performed using the interface systems between water and the exposed (100) and (001) surfaces of Ca(OH)₂ (**Figure 5.6**). Over time, OH⁻ dissolved from both the (100) and (001) interfaces (**Figure 5.7**), and Ca²⁺ was also dissolved in the case of the relatively unstable (100) surface. To check whether water intercalated into the interior of the Ca(OH)₂ crystal lattice, the number of water molecules in the Ca(OH)₂ crystal slab between the outermost Ca layers in contact with water was determined from the concentration profile. For the stable (001) surface, no water molecules were intercalated between the Ca(OH)₂ crystal, and it was observed that water molecules were adsorbed at the OH⁻ vacancy (**Figure 5.8a** and **b**). In contrast, for the (100) surface exposed by uncoordinated Ca²⁺ and OH⁻, the intercalated water in the Ca(OH)₂ crystal existed with a much larger amount of dissolved Ca²⁺ and OH⁻ (**Figure 5.8c** and **d**). This means that during the dissolution of Ca²⁺ and OH⁻ at the interface between water and the Ca(OH)₂ (100) surface, some water molecules were adsorbed on the surface, and other water molecules intercalated into the Ca(OH)₂ interlayer. To prove the lattice expansion from these conditions, the average distance between Ca(OH)₂ interlayers was measured by the radial distribution function (RDF) between alternating Ca−Ca layers (**Figure 5.9**). The average Ca−Ca distance of the interface system between the Ca(OH)₂ (100) surface and water was approximately 0.04 Å longer than those of the bulk system and the interface system between the Ca(OH)₂ (001) surface and water. From these results, we confirmed that the water molecules intercalated into the Ca(OH)₂ interlayers through the (100) surface and caused Ca(OH)₂ lattice expansion.
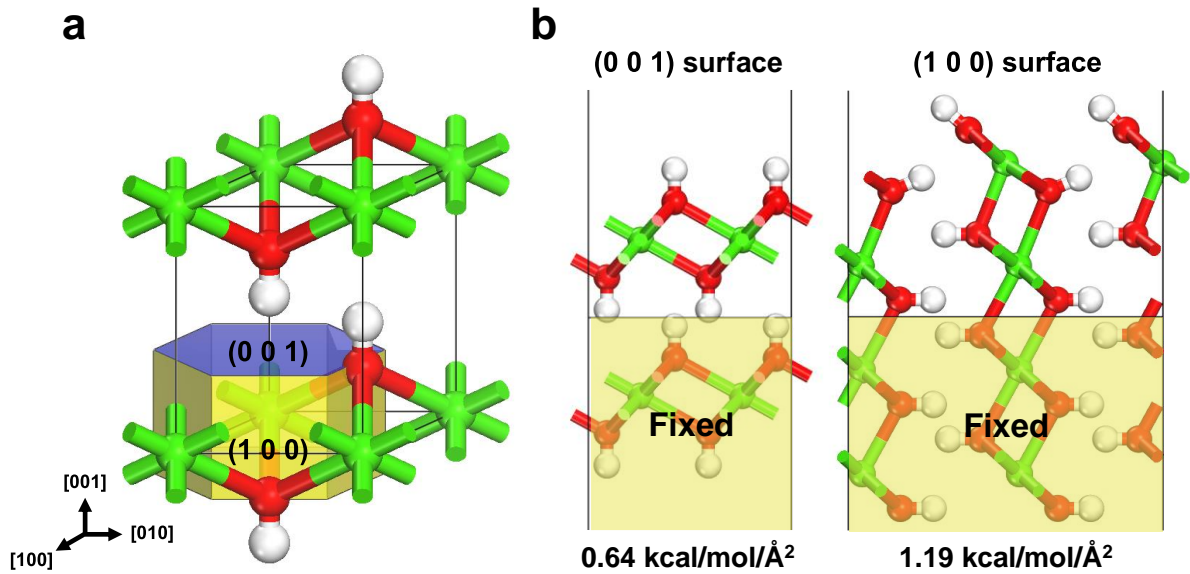
Figure 5.6 (a) BFDH morphology of Ca(OH)$_2$, (b) Optimized structures of (001) and (100) surfaces of Ca(OH)$_2$ with respective surface energies. Bottom yellow regions are fixed to represent the bulk crystal phase. Ca, O, and H are colored green, red, and white, respectively.
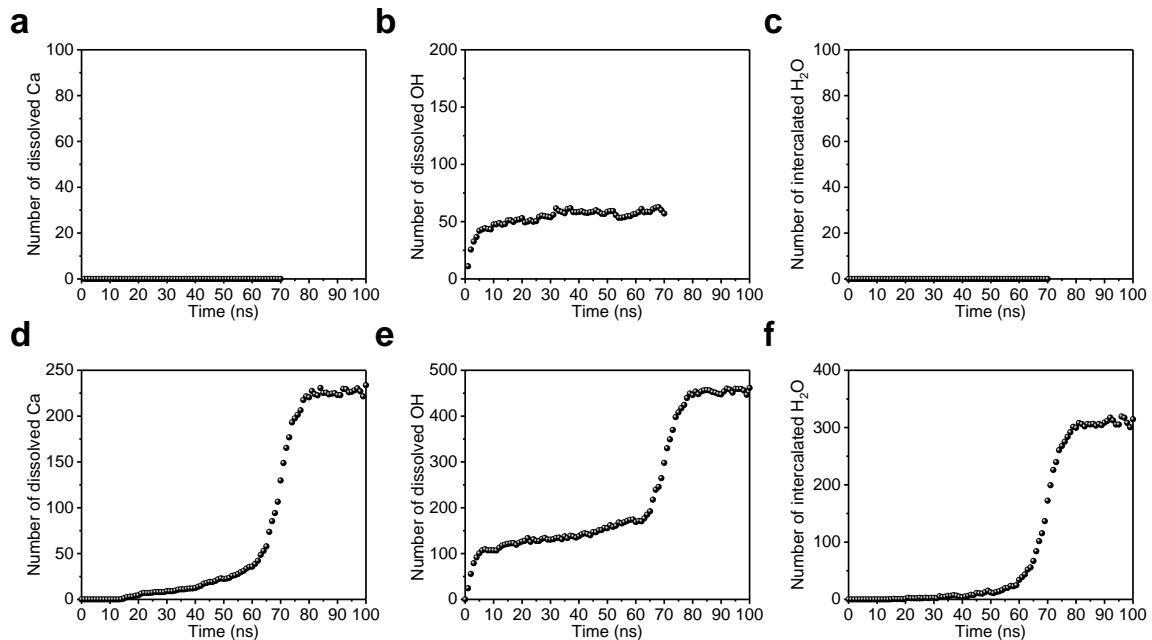
Figure 5.7 Number of (a) dissolved Ca^{2+}, (b) dissolved OH$^-$, and (c) intercalated H$_2$O molecules in the interface system between water and (001) surface. (d) Number of dissolved Ca^{2+}, (e) dissolved OH$^-$, and (f) intercalated H$_2$O molecules in the interface system between water and (100) surface.

71
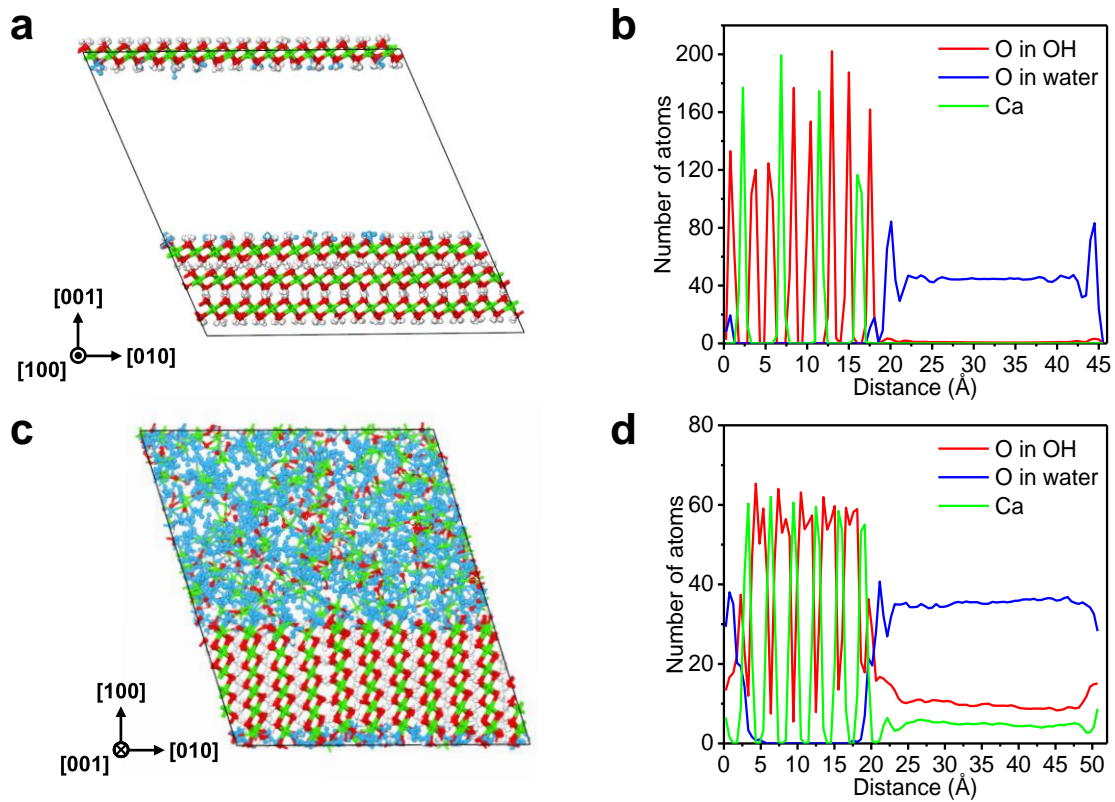
Figure 5.8 (a) Snapshot of interface system between water and Ca(OH)$_2$ (001) surface and (b) concentration profiles along the [001] direction. (c) Snapshot of interface system between water and Ca(OH)$_2$ (100) surface, and (d) concentration profiles along the [100] direction. Water, Ca, O, and H are colored light blue, green, red, and white, respectively. Dissolved Ca^{2+}, OH$^-$ and free water molecules which were not bonded to Ca(OH)$_2$ were omitted for the clarity.
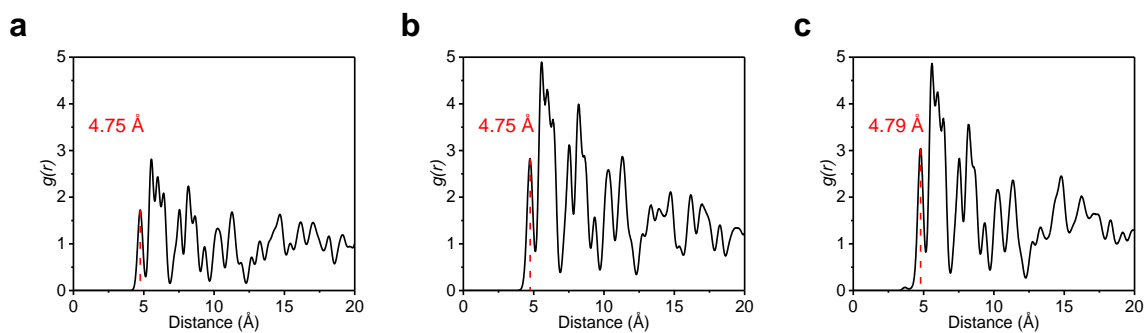
Figure 5.9 Radial distribution functions between alternating Ca^{2+} layers of (a) pristine Ca(OH)$_2$, (b) Ca(OH)$_2$ (001), and (c) Ca(OH)$_2$ (100) systems. First peak is represented by red dashed-vertical line with its distance.

Furthermore, to identify the effect of water intercalated into the $Ca(OH)_2$ interlayers on carbonation reaction, we compared the carbonation reaction mechanisms of pristine $Ca(OH)_2$ and water intercalated $Ca(OH)_2$ (i.e., hydrated $Ca(OH)_2$). The overall carbonation mechanism can be divided into two steps after CO_2 adsorption: HCO_3^- formation from CO_2 and CO_3^{2-} formation from HCO_3^-. First, in the case of the (001) surface (**Figure 5.10**), the CO_2 adsorption energy on the pristine $Ca(OH)_2$ is lower (*i.e.*, 15.16 kJ/mol) than that on the hydrated $Ca(OH)_2$ because the water molecules adsorbed on the surface prevent the interaction between CO_2 and the $Ca(OH)_2$ surface. Subsequently, in both carbonation reaction mechanisms of pristine $Ca(OH)_2$ and hydrated $Ca(OH)_2$, the CO_3^{2-} formation step from HCO_3^-, where the hydrogen of HCO_3^- is transferred to OH^- of $Ca(OH)_2$ to form CO_3^{2-} and H_2O was confirmed to be the rate-determining step (RDS). The water molecules in hydrated $Ca(OH)_2$ reduce the activation energy of 7.34 kJ/mol as mediators of proton transfer in the RDS. In addition, the adsorbed water molecules formed hydrogen bonds with the products, thereby reducing the heat of reaction by -53.00 kJ/mol. This implies that the water molecules adsorbed on the surface can promote the carbonation reaction. Second, in the case of the (100) surface (**Figure 5.11**), the RDSs appear to be different depending on the presence of water molecules. For pristine $Ca(OH)_2$, the RDS is the HCO_3^- formation step from CO_2, whereas for hydrated $Ca(OH)_2$, the RDS is the CO_3^{2-} formation step from HCO_3^-. In the initial CO_2 adsorption step, compared to the pristine $Ca(OH)_2$ surface, the hydrated $Ca(OH)_2$ surface exhibited the lowest adsorption energy of CO_2 (*i.e.*, -128.61 kJ/mol), which had a strong tendency for chemisorption. In the subsequent step, the hydrogen of the hydroxyl group on the hydrated $Ca(OH)_2$ surface was directly transferred to adsorbed CO_2 to form HCO_3^-, resulting in lower activation energy due to intercalated water molecules. The intercalated water molecules formed chemical bonds with uncoordinated Ca^{2+}; thus, the relatively more unstable OH^- was exposed on the (100) surface. Furthermore, in the RDS of hydrated $Ca(OH)_2$, the intercalated water molecules also act as proton-transfer mediators, which results in lower activation energy. In conclusion, for the case of the (001) surface, the water molecules adsorbed on the $Ca(OH)_2$ surface slightly accelerate the carbonation reaction by acting as mediators for proton transfer, whereas in the case of the (100) surface, the intercalated water molecules bound to uncoordinated Ca^{2+} facilitate the formation of CO_3^{2-} by rendering the OH^- more unstable.
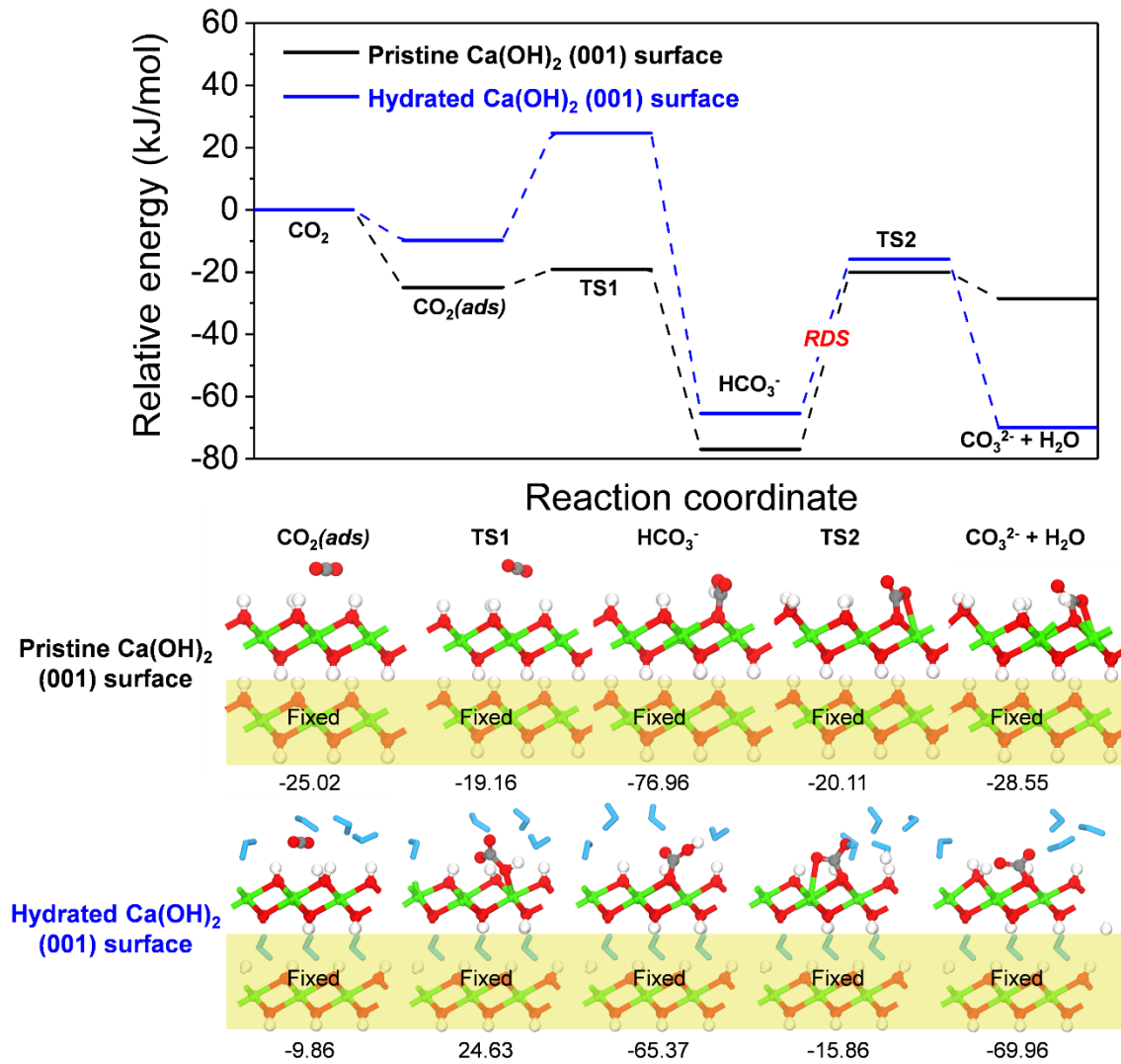
Figure 5.10 Carbonation reaction mechanisms of pristine $Ca(OH)_2$ and hydrated $Ca(OH)_2$ on (001) surface. Optimized configurations of each reaction state with energy values are represented below. Unit of energy is kJ/mol. Bottom yellow regions are fixed to represent the bulk crystal phase. Water molecules, Ca, O, C, and H are colored light blue, green, red, gray, and white, respectively.
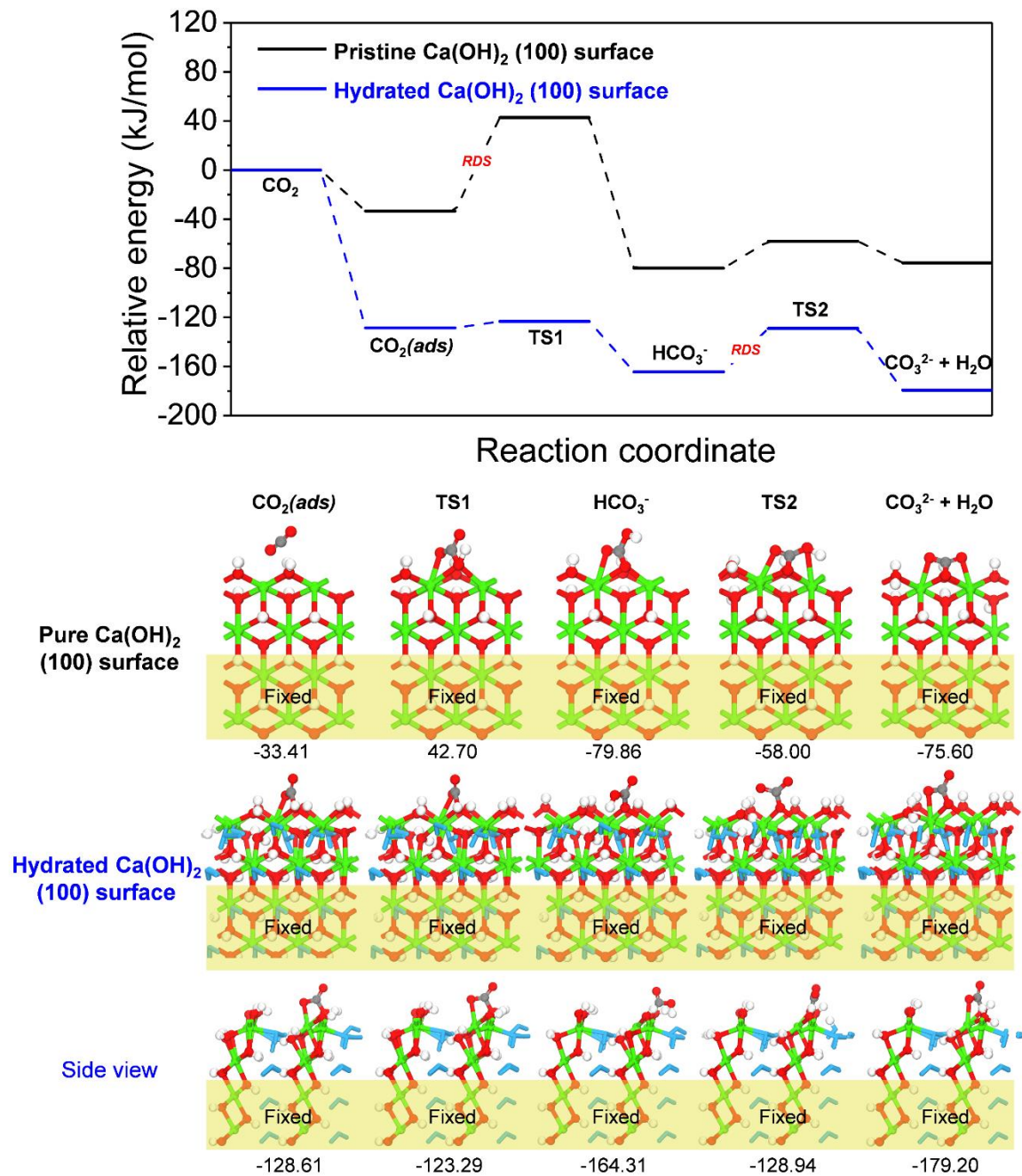
Figure 5.11 Carbonation reaction mechanisms of pristine $Ca(OH)_2$ and hydrated $Ca(OH)_2$ on (100) surface. Optimized configurations of each reaction state with energy values are represented below. Unit of energy is kJ/mol. Bottom yellow regions are fixed to represent the bulk crystal phase. Water molecules, Ca, O, C, and H are colored light blue, green, red, gray, and white, respectively.

5.4 Conclusion

During the mixing of $Ca(OH)_2$ with water, the physical and chemical properties of hydrated $Ca(OH)_2$ changed due to the water molecules. Theoretical calculations confirmed that the $Ca(OH)_2$ crystal with intercalated water molecules can form the most stable structure among the other intercalated species (i.e., CO_2, Ca^{2+}, CO_3^{2-}, and HCO_3^-). The water molecules that were intercalated into the $Ca(OH)_2$ crystal lattice through the relatively unstable (100) surface increased the interplanar distance in the [001] direction. Notably, the intercalated water molecules can lower the heat of reaction and activation energy of the carbonation reaction, thus causing spontaneous carbonation. Based on the results of theoretical calculations, the changes in the physical and chemical properties that appear due to the interaction between $Ca(OH)_2$ and water were explored, and in addition, the fundamental driving force for the carbonation reaction of hydrated $Ca(OH)_2$ was studied. This approach improves the fundamental understanding of the role of water in the carbonation reaction and provides a new strategy for CO_2 storage using cement materials.

5.5 Reference

1. Park, J. H.; Kim, S. H.; Kim, J. C.; Choi, B.-Y. Kwak, S. K.; Han, O. H.; Kim, Y.-I.; Lee, S. W. *Chemical Engineering Journal* **2021**, 420, 130422.

2. Bausach, M.; Pera-Titus, M.; Fite, C.; Cunill, F.; Izquierdo, J.-F.; Tejero, J.; Iborra, M. *AIChE Journal* **2006**, 52, 2876−2886.

3. Czechowski, F.; Marcinkowski, T. *Water Research* **2006**, 40, 1895–1905.

4. Laèevi, A.; Vrani, E.; Zuli, I. *Journal of Basic Medical Sciences* **2003**, 3, 26−29.

5. Snæbjornsdottir, S. Ó.; Sigfússon, B.; Marieni, C.; Goldberg, D.; Gislason, S. R.; Oelkers, E. H. *Nature Reviews Earth & Environment* **2020**, 1, 90–102.

6. Moorehead, D. R. *Cement and Concrete Research* **1986**, 16, 700−708.

7. Ramachandran, V. S. *Cement and Concrete Research* **1979**, 9, 677−684.

8. Chatterji, S. *Cement and Concrete Research* **1979**, 9, 185−188.

9. Blamey, J.; Lu, D. Y.; Fennell, P. S.; Anthony, E. J. *Industrial & Engineering Chemical Research* **2011**, 50, 10329−10334.

10. Pogge von Strandmann, P. A. E.; Burton, K. W.; Snæbjörnsdóttir, S. O.; Sigfússon, B.; Aradóttir, E. S.; Gunnarsson, I.; Alfredsson, H. A.; Mesfin, K. G.; Oelkers, E. H.; Gislason, S. R. *Nature Communications* **2019**, 10, 1−7.

11. Corkhill, C. L.; Bridge, J. W.; Chen, X. C.; Hillel, P.; Thornton, S. F.; Romero-Gonzalez, M. E.;

Banwart, S. A.; Hyatt, N. C. *Environ. Sci. Technol.* **2013**, 47, 13857−13864.

12. Ewing, R. C. *Nat. Mater.* 2015, 14, 252−257.

13. Thenepalli, T.; Ahn, Y. J.; Han, C.; Ramakrishna, C.; Ahn, J. W. *Korean J. Chem. Eng.* **2015**, 32, 1009−1022.

14. Van Balen, K. *Cem. Concr. Res.* **2005**, 35, 647−657.

15. Nikulshina, V.; Galvez, M. E.; Steinfeld, A. *Chem. Eng. J.* **2007**, 129, 75−83.

16. Funk, A.; Trettin, H. F. R. *Ind. Eng. Chem. Res.* **2013**, 52, 2168−2173.

17. Raiteri, P.; Gale, J. D. *J. Am. Chem. Soc.* **2010**, 132, 17623−17634.

18. Farhadi-Khouzani, M.; Chevrier, D. M.; Zhang, P.; Hedin, N.; Gebauer, D. *Angew. Chem. Int. Ed.* **2016**, 55, 8117−8120.

19. Wray, J. L.; Daniels, F. *J. Am. Chem. Soc.* **1957**, 79, 2031−2034.

20. Gu, W.; Bousfield, D. W.; Tripp, C. P. *J. Mater. Chem.* **2006**, 16, 3312−3317.

21. Delley, B. *J. Chem. Phys.* **1990**, 92, 508−517.

22. Delley, B. *J. Chem. Phys.* **2000**, 113, 7756−7764.

23. Perdew, J. P.; Burke, K.; Ernzerhof, M. *Phys. Rev. Lett.* **1996**, 77, 3865−3868.

24. Tkatchenko, A.; Scheffler, M. *Phys. Rev. Lett.* 2009, 102, 073005.

25. Monkhorst, H. J.; Pack, J. D. *Phys. Rev. B* 1976, 13, 5188−5192.

26. Klamt, A.; Schüürmann, G. *J. Chem. Soc. Perkin Trans. 2* 1993, 5, 799–805.

27. Bell, S.; Crighton, J. S. *J. Chem. Phys.* **1984**, 80, 2464–2475.

28. Halgren, T. A.; Lipscomb, W. N. *Chem. Phys. Lett.* 1977, 49, 225–232.

29. Cygan, R. T.; Liang, J. -J.; Kalinichev, A. G. *J. Phys. Chem. B* **2004**, 108, 1255−1266.

30. Samoletov, A. A.; Dettmann, C. P.; Chaplain, M. A. J. *J. Stat. Phys.* **2007**, 128, 1321−1336.

31. Parrinello, M.; Rahman, A. *J. Appl. Phys.* **1981**, 52, 7182−7190.

32. Somasundaran, P.; Agar, G. E.; *J. Colloid Interface Sci.* **1967**, 24, 433−440.

33. Ruiz-Agudo, E.; Kudłacz, K.; Putnis, C. V.; Putnis, A.; Rodriguez-Navarro, C. *Environ. Sci. Technol.* **2013**, 47, 11342−11349.

Chapter 6. Summary and Future Perspectives

6.1 Summary

In depth understanding of the chemical reactions is important in various research theme related to renewable energy and environment. Through this, it is possible to devise an eco-friendly synthesis method for the formation of chemical materials or to provide the characteristic on materials capable of improving the low energy efficiency. This dissertation proposes the theoretical studies on the reaction mechanism in renewable energy and environment applications using the multi-scale molecular simulations.

In Chapter 1, a brief overview of the importance of chemical reaction in renewable energy and environment was discussed. Although continuous studies have been conducted on these applications, several issues such as low performance and uneconomical synthesis methods still remain. We provided the in-depth understanding for chemical reaction and revealed the driving force of the chemical phenomena by investigating the reaction mechanism. In this regard, we have described the multiscale simulation methods including the DFT calculation and MD simulation to figure out the reaction mechanism.

In Chapter 2, we proposed the noble protocol for formation of desired products from the biomass with the highly effective and selective catalytic systems. Based on the solvation energy in each solvent and the reaction mechanisms of glucose isomerization, The solvent effect of 1-butanol and the catalytic ability of hydrotalcite served as important factors in the glucose isomerization. Furthermore, we identified that the stable initial structure of adsorbed fructose at mannitol pathway was more thermodynamically favorable and mannitol formation reaction has the lower activation energy. Thus, by presenting an effective biomass synthesis method, these studies can have a great impact on renewable energy and environmental aspects.

In Chapter 3, we presented the investigation of solvothermal liquefaction mechanism of lignin constituents in the formic acid and supercritical ethanol mixture solvent using the reactive molecular dynamics (reax-MD) and DFT calculation. In the mechanism, the formic acid provided hydrogen to facilitate the dissociation of the C−O bond of lignin. Besides, the supercritical ethanol solvent served to transfer hydrogen away from formic acid to lignin. In short, the decompositions of C−C and C−O linkages of lignin under the ethanol−FA mixture environment were more advantageous than those of the thermal- and ethanol-assisted decomposition reactions.

In Chapter 4, we theoretically elucidated the first universal solution synthesis of sulfide SEs

using an alkahest solvent system. Binary mixtures of EDA and EDT which manifest strong dissolving power for metal chalcogenides, fully dissolved not only conventional sulfide SE precursors of Li_2S, P_2S_5, and Na_2S, but also metal sulfides, such as GeS_2. This mechanistic calculation suggested a plausible formation of polyanionic Ge−S clusters through a continuous dissolution reaction. Thus, this result will provide the new opportunities for synthesis of the soft-chemistry-guided conductors for ASSBs which reduce the carbon footprint.

In Chapter 5, many studies on mineral carbonation which can reduce the air pollution and use it as a renewable energy source by capturing carbon dioxide in the air have been conducted. We theoretically demonstrated the effect of intercalated water in the carbonation reaction of calcium hydroxide. Through MD simulation, we identified that the water molecules can be infiltrated at interlayer space of calcium hydroxide and the distance between the interlayers was increased. Notably, the intercalated water molecules can lower the heat of reaction and activation energy of the carbonation reaction, thus causing spontaneous carbonation. This approach improves the fundamental understanding of the role of water in the carbonation reaction and provides a new strategy for CO2 storage using cement materials.

Overall, we investigated the mechanism of chemical reaction for renewable energy and environmental applications, that could propose the new protocol for biomass products or develop the materials that reduce carbon footprint. From these studies, we can provide the fundamental knowledge of the highly effective chemical reaction from a molecular point of view and can suggest a new strategy for designing new material or process beyond our molecular understanding of the reaction.

6.2 Future Perspectives

We put forward future work to design new catalyst for the target reaction by screening the characteristics of the catalyst materials for forming the biomass product which related to current investigation in renewable energy system. We are aiming to extend our works from the calculation of reaction mechanism to the search for the optimal catalyst.

Recently, with the rapid advances in computational method, the design of catalyst has been attempted.[1–3] In theoretical screening methods to search for ideal catalyst, sequential steps are indispensable, as shown Figure 6.1. First, we have to obtain the mechanistic insight for target reaction using a known catalytic material. Afterwards, we investigate the physical and chemical properties of the catalyst, find the relationship between these properties and the reaction mechanism, and then derive a descriptor which is an important key factor in the screening study. Generally, various catalytic reactions are quite complex, so there are too many factors to consider such as many reaction paths, the presence of many intermediate, and structural complexity of catalyst materials. The solution to this problem lies in the generality of the scaling relations by the descriptors such as adsorption energy of reactant on surface and electrical properties of catalyst. In subsequent step, these descriptors will be applied to different catalyst candidates. Finally, the optimal catalyst for target reaction can be proposed from the expected performance of catalysts by the descriptors.

STEP 1

Reaction mechanism
Analysis of reaction mechanism and rate

STEP 2

Descriptors
Determine of factors for catalytic reaction by scaling relationship

STEP 3

Catalyst screening
Screening of reaction factors for various catalysts

STEP 4

Design catalyst
Optimization of catalyst performance for each reaction
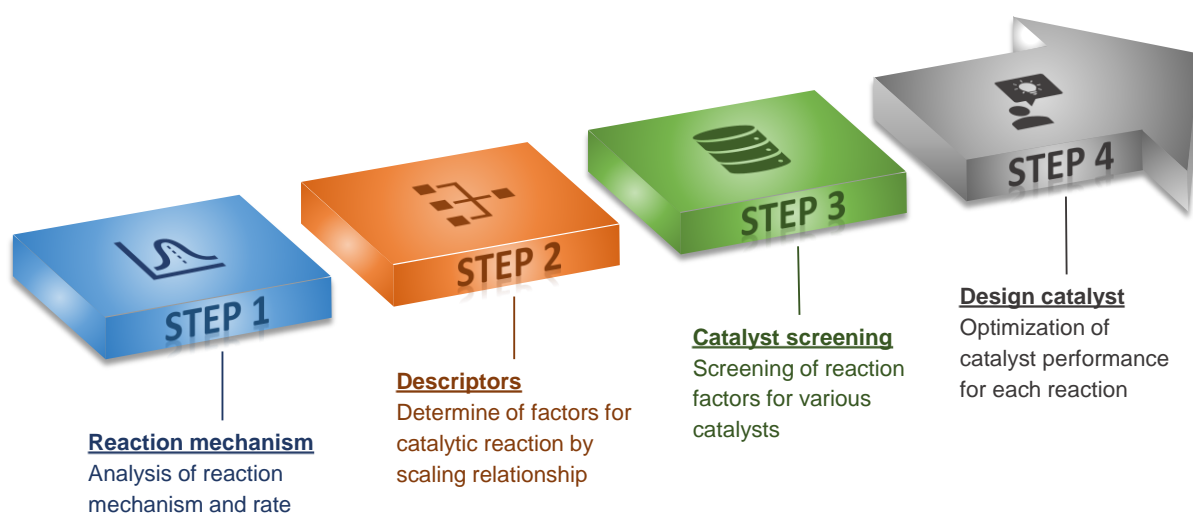
Figure 6.1 Schematic to design optimal catalyst for target reaction.

As the first target reaction through these methods, we will try to design the optimal tandem catalyst

for conversion of carbon dioxide to high-value chemicals using zeolite and metal oxide. (**Figure 6.2**) The high added value and direct utilization of CO_2 has been suggested as important approach, which can serve to a sustainable carbon footprint and economic growth. In current trend, to solve its environmental and renewable energy issues, the conversion of CO_2 has been studied through various strategies such as the photocatalytic, chemo-biocatalytic, chemo-enzymatic, and catalytic reaction.[4–7] Among these methods, we intend to convert CO_2 through the most efficient and practical catalytic reaction. First, to design the optimal catalyst, it is necessary to explore what chemical materials with high-value that can be produced from CO_2, and the reaction mechanisms for these products should be investigated. F. Jaramillo and coworker detected a total of 16 different reaction products: number of which were novel products that were for the first time identified and quantified from a surface of Cu metal catalyst. Of the 16 reaction products detected, 12 of them were C_2 or C_3 species, comprised of a broad mix of oxygenated species including hydrocarbons, ketones, aldehydes, carboxylic acids, and alcohols.[8] They also presented the mechanistic view of each product formed from the CO_2 reduction reaction. However, since the reaction of CO_2 conversion is quite complex, it is difficult to obtain the desired products with simple heterogeneous catalyst. Tan's research team performed the catalytic conversion of CO_2 into high value-added hydrocarbons using a tandem catalyst which is composed of different types of catalytic sites.[9] Applying this strategy, we will also investigate the reaction mechanism and descriptors of tandem catalyst which composed to zeolite and metal oxide. Through these descriptors, we want to develop the most optimal catalyst by screening various zeolite models and metal types. This future research direction for developing new optimal tandem catalyst is expected to be one of the most promising strategies in the conversion of CO_2 to sustainable fuels and renewable energy.
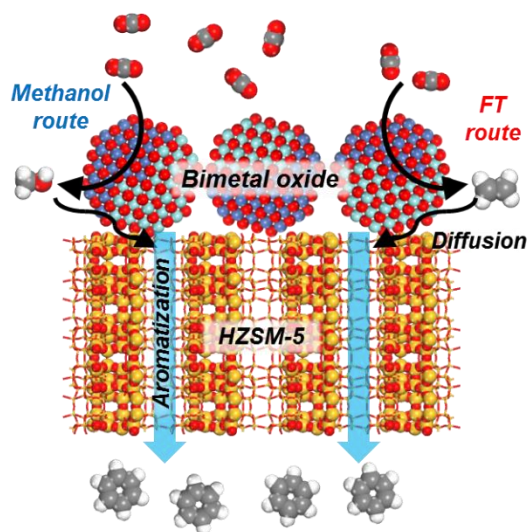
Figure 6.2 Schematic of tandem catalyst for conversion of carbon dioxide to high-value chemicals.

6.3 Reference

1. Rossmeisl, J.; Greeley, J.; Karlberg G.S. (2008) Chapter 3: *Electrocatalysis and Catalyst Screening from Density Functional Theory Calculations in Fuel Cell Catalysis: A Surface Science* Approach John Wiley & Sons

2. Yeo, B. C.; Nam, H.; Nam, H.; Kim, M.-C.; Lee, H. W.; Kim, S.-C.; Won, S. O.; Kim, D.; Lee, K.-L.; Lee, S. Y.; Han, S. S *npj Comput. Mater.* **2021**, 7, 137.

3. Yang, Z.; Gao, W.; Jiang, Q. *J. Mater. Chem. A*, **2020**, 8, 17507–17515.

4. Nguyen, D. L. T.; Nguyen, T. M.; Lee, S. Y.; Kim, J.; Kim, S. Y.; Le, Q. V.; Varma, R. S.; Hwang, Y. J. *Environmental Research* **2022**, 211, 113116.

5. Galhardo, T. S.; Braga, A. H.; Arpini, B. H.; Szanyi, J.; Goncalves, R. V.; Zornio, B. F.; Miranda, C. R.; Rossi, L. M. *J. Am. Chem. Soc.* **2021**, 143, 4268−4280.

6. Ye, R.-P.; Ding, J.; Gong, W.; Argyle, M. D.; Zhong, Q.; Wang, Y.; Russell, C. K.; Xu, Z.; Russell, A. G.; Li, Q.; Fan, M.; Yao, Y.-G. *Nat. Commun.* **2019**, 10, 5698.

7. Pérez-Rodríguez, S.; Rillo, N.; Lázaro, M. J.; Pastor, E. Appl. Catal. B: Environ. 2015, 163, 83–95.

8. Kuhl, K. P.; Cave, E. R.; Abram, D. N.; Jaramillo, T. F. *Energy Environ Sci.*, **2012**, 5, 7050–7059.

9. Xing, W. X.; Hong, D. Y.; Feng, Z. J.; Sheng, T. Y. *J. Fuel Chem. Technol.* **2022**, 5, 538-563.

Acknowledgement

Since I entered UNIST as an undergraduate student in March 2012, it has taken about 11 years to complete the combined master's and doctoral course after graduation. With the support of many people, I can overcome many difficulties and finally graduate. So, I would like to express my gratitude to the many people who helped.

First of all, I would like to express my deep gratitude to Professor Sang Kyu Kwak, who guided me as my advisor when I was interested in research from the sophomore year of undergraduate studies to now. The professor gave me suitable research topics and a lot of supports because I wanted to look for the motions of molecules in various reactions. Also, a lot of advice of the professor helped me by guiding me not out of path of research. The sincerity of the professor always motivates me to do research and I was able to work hard.

Next, I would like to thank Professor Jong-beom Baek for giving me the opportunity to deal with the various mechanisms of the organic synthesis process during my degree course. I would also like to thank Professor Ja Hyoung Ryu for suggesting various joint research topics, including research on biomaterials for cancer cell processing. In addition, I would like to thank Professor Yoon Seok Jung for giving me the opportunity to conduct research on all-solid-state batteries, which are currently being studied the most. Lastly, I have not been able to conduct research together, but I would also like to thank Professor Kwangjin An for participating in the degree review and commenting on the direction I should go forward as a computational researcher and the problems to be corrected. I will try to become a better researcher with the valuable advice given by professors.

Furthermore, I would like to express my gratitude to Dr. Jeong Hyeon Lee, who meticulously looked at the problems I missed and helped me with a lot of knowledge while studying together for a long time since my undergraduate days. And I would like to express my gratitude to the lab seniors, Prof. Tae Kyung Lee, Dr. Gwan Yeong Jung, Dr. Woo Cheol Jeon, Dr. Eunhye Shin, Dr. Sung O Park, Dr. Dae Yeon Hwang, Dr. Ju Hyun Park, Dr. Su Hwan Kim, Dr. Se Hun Joo, and Dr. Eun Min Go, and Dr. kris. Additionally, I would like to thank other lab members, Jiyun Lee, Kyung Min Lee, Hyeong Yong Lim, Hyeongjun Kim, Ji Eun Lee, Yu Jin Kim, Seung Hak Oh, Seong Hyeon Kweon, Seung Min Lee, Yumi Cho, and Ju Hwan Kang, for their helps during Ph.D. course. I hope you accomplish everything thing that you want.

Finally, I would like to thank my family for always supporting. I would like to say that I am always grateful to my parents for always worrying about my health and taking care of me.

Sincerely, *Jin Chul Kim*

Acknowledgement (감사의 글)

2012년 3월 UNIST에 학부생으로 입학하여 학부 졸업 이후 석박사통합과정을 마무리하기까지 약 11년의 시간이 지났습니다. 현재까지 많은 분들의 지원을 받아 많은 어려움을 넘어 무사히 졸업하게 되었습니다. 도움을 주셨던 많은 분들께 감사의 인사를 전하고자 합니다.

먼저, 학부 2학년 당시 연구에 대해 관심이 많던 저를 이끌어 주시고 지금까지 지도해주신 곽상규 교수님께 깊은 감사를 드립니다. 여러 반응 내에서 분자들의 움직임을 보고 싶었던 저에게 적절한 연구 주제를 주셨고, 연구 외의 생활에서도 수많은 지원을 아끼지 않으셨습니다. 또한 연구의 길에서 벗어나지 않도록 교수님께서 주셨던 많은 조언들이 저에게 큰 힘이 되었습니다. 연구를 진행함에 있어 언제나 진심을 다하시는 교수님의 모습이 자극이 되어 저 또한 노력할 수 있었습니다. 다시 한번 감사드립니다.

다음으로, 지난 학위 과정 동안 유기 합성 과정에 대한 여러 메커니즘을 다룰 수 있도록 기회를 주신 백종범 교수님께 감사의 말씀을 드립니다. 또한, 암 세포 처리를 위한 생체 물질 연구를 포함한 다양한 공동 연구 주제를 제안해주신 유자형 교수님께도 감사의 말씀드립니다. 뿐만 아니라 현재 가장 많은 연구가 이루어지고 있는 전고체 배터리에 대한 연구를 함께 진행할 수 있는 기회를 주신 정윤석 교수님께도 감사드립니다. 마지막으로 함께 연구를 진행해보진 못했으나, 학위 심사에 참여해 주셔서 계산 연구자로써 앞으로 제가 나아가야할 방향 및 고쳐야할 문제에 대한 코멘트를 주신 안광진 교수님께도 감사드립니다. 교수님들께서 주셨던 귀중한 조언들을 담아 더 나은 연구자가 되도록 노력하겠습니다.

그리고 학부생 시절부터 함께 오랫동안 연구하며 제가 놓친 문제들을 꼼꼼하게 살펴주고 많은 지식으로 저를 도와주었던 이정현 박사님에게 고맙다는 말을 전합니다. 그리고 항상 앞서 나가 저에게 연구의 길을 알려주셨던 연구실 선배님들께도 (이태경 교수님, 정관영 박사님, 전우철 박사님, 신은혜 박사님, 박성오 박사님, 황대연 박사님, 박주현 박사님, 주세훈 박사님, 김수환 박사님, 고은민 박사님, kris 박사님) 감사의 마음을 전합니다. 아울러 같이 연구실 생활을 하며 도움을 주고받았던 연구실 동기 및 후배들 (지윤이형, 경민, 형용이형, 형준, 지은, 유진, 승학, 성현, 승민, 유미, 재권이, 대현이, 주환이)에게 고맙다는 말을 전합니다. 모두 하고 있는 연구들이 모두 잘 풀리길 바랍니다.

마지막으로 제가 무슨 일을 하는 지 관계없이 항상 저를 지지해주시고 도와준 가족들에게 감사의 말씀을 드리고 싶습니다. 항상 저의 건강을 걱정해 주시며 챙겨 주신 부모님께 항상 감사하다는 말을 전해드립니다.

<div align="right">김진철 올림.</div>

List of Publications

Total publications : 34 papers (including papers in preparation/submitted accepted)

First or co-first author [†: equal contribution]

1. Jeong Hyeon Lee†, **Jin Chul Kim†**, Jiyun Lee†, Seung Hak Oh, Seung Woo Lee, Byeong Yeong Choi*, and Sang Kyu Kwak*, "Theoretical and Mechanistic Insights into Control Factor-Assisted CO_2 Mineralization with Olivine", *submitted*

2. Jinseong Kim,† Jaehee Shim,† Jin Chul Kim,† Eunhee Jang, Jeong Hyeon Lee, Hionsuck Baik, Chun Yong Kang, Chang Hwan Kim, Kwan-Young Lee, Sang Kyu Kwak,* and Jungkyu Choi*, "Unveiling the elusive roles of Cu species in Cu-impregnated MFI type zeolites in determining the hydrocarbon trap abilities during cold start" *submitted*

3. **Jin Chul Kim†**, Jeong Hyeon Lee†, Seung Hak Oh, Kyeongmin Baek, Jong-San Chang*, and Sang Kyu Kwak*, "A Mechanistic Study of the Hydrolysis of Tetrafluoromethane on γ-Alumina", *submitted*

4. Ji Eun Lee†, Kern-Ho Park†, **Jin Chul Kim†**, Tae-Ung Wi, A. Reum Ha, Yong Bae Song, Dae Yang Oh, Jehoon Woo, Seong Hyeon Kweon, Su Jeong Yeom, Woosuk Cho, Kyung Su Kim, Hyun-Wook Lee*, Sang Kyu Kwak*, and Yoon Seok Jung* "Universal Solution Synthesis of Sulfide Solid Electrolytes Using Alkahest for All-Solid-State Batteries"
   Advanced Materials, 34(16), 2200083, **2022**

5. Woo Cheol Jeon†, Jeong Hyeon Lee†, **Jin Chul Kim†**, Sang-Hyun Jung, Soo Gyeong Cho, and Sang Kyu Kwak*, "Controllable Explosion of Nanobomb by Modifying Nanocontainer and External Shocks"
   Journal of Physical Chemistry C, 124(5), 3341-3351, **2020**

6. Woo Cheol Jeon†, Jeong Hyeon Lee†, **Jin Chul Kim†**, Seok Ju Kang, Sang-Hyun Jung, Soo Gyeong Cho, and Sang Kyu Kwak*, "Reaction Kinetics of Mixture of Nitromethane and Detonator Confined in Carbon Nanotube"
   Journal of Industrial and Engineering Chemistry, 83(25), 64-71, **2020**

7. Gyujin Song†, Jaegeon Ryu†, **Jin Chul Kim†**, Jeong Hyeon Lee, Sungho Kim, Chongmin Wang, Sang Kyu Kwak*, and Soojin Park*, "Revealing salt-expedited reduction mechanism for hollow Silicon microsphere formation in bi-functional halide melts"
   Communications Chemistry, 1:42, **2018**

8. Jeong Hyeon Lee†, **Jin Chul Kim†**, Woo Cheol Jeon†, Soo Gyeong Cho*, and Sang Kyu Kwak*, "Explosion Study of Nitromethane Confined in CNT Nanocontainer via Reactive Molecular Dynamics"
   Journal of Physical Chemistry C, 121(12), 6415–6423, **2017**

Co-author

9. M. T. Jeena†, Seongeon Jin†, Keunsoo Jeong, Yuri Cho, **Jin Chul Kim**, Jeong Hyeon Lee, Seokyoung Lee, Suk-Won Hwang, Sang Kyu Kwak*, Sehoon Kim*, and Ja-Hyoung Ryu*, "Cancer-Selective Supramolecular Chemotherapy by Disassembly-Assembly Approach", *Advanced Functional Materials,* 32(52), 2208098, **2022**

10. Seung-Jun Kim†, Jin-Hong Seok†, In Cheol Yu†, Jeong Hyeon Lee†, Won Tae Kim, Bong-Rim Shin, Ga-Eun Yoon, Yun-Sang Lee, **Jin Chul Kim**, Woojin Yoon, Hoseop Yun, Mojca Jazbinsek, Sang Kyu Kwak*, Fabian Rotermund*, O-Pil Kwon*, "Orthogonal Molecular Assembly: Eliminating Intrinsic Phonon Modes in Organic THz Generators"
    Advanced Optical Materials, 10(23), 2102654, **2022**

11. Inho Song†, Xiaobo Shang†, Jaeyong Ahn, Jeong Hyeon Lee, Wanuk Choi, Hiroyoshi Ohtsu, **Jin Chul Kim**, Sang Kyu Kwak, and Joon Hak Oh*, "Surface Doping Effect on the Optoelectronic Properties of Tetrachloro-Substituted Chiral Perylene Diimides Supramolecular Nanowires", *Chemistry of Materials*, 34(19), 8675-8683, **2022**

12. Kyung Ho Cho, Ji Woong Yoon, Jeong Hyeon Lee, **Jin Chul Kim**, Kiwoong Kim, Jong-San Chang*, Sang Kyu Kwak*, U-Hwang Lee*, "Separation of ethane/ethylene gas mixture by ethane-selective CAU-3-NDCA adsorbent"
    Microporous and Mesoporous Materials, 530, 111572, **2022**

13. Soo-Young Yu, **Jin Chul Kim**, Hyuk-Jun Noh, Yoon-Kwang Im, Javeed Mahmood, In-Yup Jeon*, Sang Kyu Kwak*, and Jong-Beom Baek*, "Direct conversion of aromatic amides into crystalline covalent triazine frameworks by a condensation mechanism"
    Cell Reports Physical Science, 2(12), 100653, **2021**

14. Byeong M. Oh†, Sung-Ha Park†, Jeong Hyeon Lee, **Jin Chul Kim**, Jong Bum Lee, Hyeong Ju Eun, Yun-Sang Lee, Bo Eun Seo, Woojin Yoon, Hoseop Yun, Sang Kyu Kwak*, O-Pil Kwon*, and Jong H. Kim*, "Strategic Approach for Enhancing Sensitivity of Ammonia Gas Detection: Molecular Design Rule and Morphology Optimization for Stable Radical Anion Formation of Rylene Diimide Semiconductors"
    Advanced Functional Materials, 31(42), 2101981, **2021**

15. Kyung Ho Cho, Ji Woong Yoon, Jeong Hyeon Lee, **Jin Chul Kim**, Kiwoong Kim, U-Hwang Lee, Minkee Choi*, Sang Kyu Kwak*, and Jong-San Chang*, "Pore control of Al-based MIL-53 isomorphs for the preferential capture of ethane in an ethane/ethylene mixture"
    Journal of Materials Chemistry A, 9(25), 14593-14600, **2021**

16. Ju Hyun Park, Sun Ha Kim, **Jin Chul Kim**, Byoung-Young Choi, Sang Kyu Kwak, O.H. Han*, Yong-Il Kim*, and Seung-Woo Lee*, "Role of intercalated water in calcium hydroxide interlayers for carbonation reaction"

Chemical Engineering Journal, 420(3), 130422, **2021**

17. Xiaobo Shang†, Jaeyong Ahn†, Jeong Hyeon Lee, **Jin Chul Kim**, Hiroyoshi Ohtsu, Wanuk Choi, Inho Song, Sang Kyu Kwak, and Joon Hak Oh*, "Bay-Substitution Effect of Perylene Diimides on Supramolecular Chirality and Optoelectronic Properties of Their Self-Assembled Nanostructures"
ACS Applied Materials & Interfaces, 13(10), 12278-12285, **2021**

18. Xiaobo Shang†, Inho Song†, Myeonggeun Han, Jeong Hyeon Lee, Hiroyoshi Ohtsu, Wanuk Choi, **Jin Chul Kim**, Jaeyong Ahn, Sang Kyu Kwak, and Joon Hak Oh*, "Majority-Rules" Effect on Supramolecular Chirality and Optoelectronic Properties of Chiral Tetrachloro-Perylene Diimides"
Advanced Optical Materials, 9(6), 2001911, **2021**

19. Van Nhieu Le†, The Ky Vo†, Jeong Hyeon Lee, **Jin Chul Kim**, Tea-Hoon Kim, Kwang Hyun Oh, Youn-Sang Bae*, Sang Kyu Kwak*, and Jinsoo Kim*, "Novel approach for preparing Cu(I)Zn@MIL-100(Fe) adsorbent with high CO adsorption capacity, CO/CO_2 selectivity, and stability via controlled host–guest redox reaction"
Chemical Engineering Journal, 404, 126492, **2021**

20. Xiaobo Shang†, Inho Song†, Jeong Hyeon Lee, Wanuk Choi, Jaeyong Ahn, Hiroyoshi Ohtsu, **Jin Chul Kim**, Jin Young Koo, Sang Kyu Kwak*, and Joon Hak Oh*, "Surface-Doped Quasi-2D Chiral Organic Single Crystals for Chiroptical Sensing"
ACS Nano, 14(10), 14146-14156, **2020**

21. Pravin P. Upare, Young Kyu Hwang, **Jin Chul Kim**, Jeong Hyeon Lee, Sang Kyu Kwak*, and Dong Won Hwang*, "A Robust and Highly Selective Catalytic System of Copper-Silica Nanocomposite and 1-Butanol in Fructose Hydrogenation to Mannitol"
ChemSusChem, 13(18), 5050-5057, **2020**

22. Kyung Ho Cho, Ji Woong Yoon, Jeong Hyeon Lee, **Jin Chul Kim**, Kiwoong Kim, U-Hwang Lee, Sang Kyu Kwak*, and Jong-San Chang*, "Effect of framework rigidity in metal–organic frameworks for adsorptive separation of ethane/ethylene"
Microporous and Mesoporous Materials, 307, 110473, **2020**

23. Eunhee Jang†, Jeong Hyeon Lee†, Sungwon Hong, Yanghwan Jeong, **Jin Chul Kim**, Dongjae Kim, Hionsuck Baik, Eunjoo Kim, Nakwon Choi, Jaewook Nam, Sung June Cho, Sang Kyu Kwak*, and Jungkyu Choi*, "An Unprecedented *c*-Oriented DDR@MWW Zeolite Hybrid Membrane: New Insights into H_2-Permselectivities via Six Membered-Ring Pores"
Journal of Materials Chemistry A, 8(28), 14071, **2020**

24. Kyungeun Baek†, Woo Cheol Jeon†, Seongho Woo, **Jin Chul Kim**, Jun Gyeong Lee, Kwangjin An*, Sang Kyu Kwak*, and Seok Ju Kang*, "Synergistic effect of quinary molten salts and ruthenium catalyst for high-power-density lithium-carbon dioxide cell"
Nature Communications, 11:456, **2020**

25. Pravin P. Upare, Ali Chamas, Jeong Hyeon Lee, **<u>Jin Chul Kim</u>**, Sang Kyu Kwak*, Young Kyu Hwang*, and Dong Won Hwang*, "A highly efficient hydrotalcite/1-butanol catalytic system for production of the high-yield fructose crystal from glucose"

    ACS Catalysis, 10(2), 1388-1396, **2020**

26. Kibeom Kim†, Sungmin Lee†, Eunji Jin, L. Palanikumar, Jeong Hyeon Lee, **<u>Jin Chul Kim</u>**, Jung Seung Nam, Tae-Hyuk Kwon, Sang Kyu Kwak*, Wonyoung Choe*, and Ja-Hyoung Ryu*, "MOF X Biopolymer: Collaborative Combination of Metal–Organic Framework and Biopolymer for Advanced Anticancer Therapy"

    ACS Applied Materials & Interfaces, 11(31), 27512-27520, **2019**

27. Xiaobo Shang†, Inho Song†, Jeong Hyeon Lee, Myeonggeun Han, **<u>Jin Chul Kim</u>**, Hiroyoshi Ohtsu, Jaeyong Ahn, Sang Kyu Kwak*, and Joon Hak Oh*, "Tuning Supramolecular Chirality and Optoelectronic Performance of Chiral Perylene Diimides Nanowires via N-Substituted Side Chain Engineering"

    Journal of Materials Chemistry C, 7, 8688, **2019**

28. Du San Baek†, Gwan Yeong Jung†, Bora Seo, **<u>Jin Chul Kim</u>**, Hyun-Wook Lee, Tae Joo Shin, Hu Young Jeong, Sang Kyu Kwak*, and Sang Hoon Joo*, "Ordered Mesoporous Metastable alpha-MoC_{1-x} with Enhanced Water Dissociation Capability for Boosting Alkaline Hydrogen Evolution Activity"

    Advanced Functional Materials, 29(28), 1901217, **2019**

29. Asim Riaz, Deepak Verma, Hassan Zeb, Jeong Hyeon Lee, **Jin Chul Kim**, Sang Kyu Kwak*, and Jaehoon Kim*, "Solvothermal liquefaction of alkali lignin to obtain a high yield of aromatic monomers while suppressing solvent consumption"

    Green Chemistry, 20(21), 4957-4974, **2018**

30. Soochan Lee, Jeong Hyeon Lee, **<u>Jin Chul Kim</u>**, Sungmin Lee, Sang Kyu Kwak*, and Wonyoung Choe*, "Porous Zr_6L_3 Metallocage with Synergetic Binding Centers for CO_2"

    ACS Applied Materials & Interfaces, 10(10), 8685-8691, **2018**

31. Eunjoo Kim, Sungwon Hong, Eunhee Jang, Jeong Hyeon Lee, **<u>Jin Chul Kim</u>**, Nakwon Choi, Churl-Hee Cho, Jaewook Nam, Sang Kyu Kwak, Alex Yip, and Jungkyu Choi*, "An Oriented, Siliceous Deca-dodecasil 3R (DDR) Zeolite Film for Effective Carbon Capture: Insight into Its Hydrophobic Effect"

    Journal of Materials Chemistry A, 22(5), 11246-11254, **2017**

32. Pravin Upare, Ji Woong Yoon, Dongwon Hwang, U-Hwang Lee, Yong Kyu Hwang, Do-Young Hong, **<u>Jin Chul Kim</u>**, Jeong Hyeon Lee, Sang Kyu Kwak, Hyeyoung Shin, Hyungjun Kim, and Jong-San Chang*, "Design of a heterogeneous catalytic process for continuous and di-rect synthesis of lactide from lactic acid"

    Green Chemistry, 18, 5978-5983, **2016**

33. Bijoy P. Mathew, Hyun Ji Yang, Himchan Jeon, Jeong Hyeon Lee, **Jin Chul Kim**, Tae Joo Shin, Kyungjae Myung, Sang Kyu Kwak*, Ja Hun Kwak*, and Sung You Hong*, "C-H bond arylation of anilides inside copper-exchanged zeolites"

    Journal of Molecular Catalysis A: Chemical, 417, 64-70, **2016**

34. Bora Seo, Gwan Yeong Jung, Young Jin Sa, Hu Young Jeong, Jae Yeong Cheon, Jeong Hyeon Lee, Ho Young Kim, **Jin Chul Kim**, Hyeon Suk Shin, Sang Kyu Kwak*, and Sang Hoon Joo*, "Monolayer-Precision Synthesis of Molybdenum Sulfide Nanoparticles and Their Nanoscale Size Effects in the Hydrogen Evolution Reaction"

    ACS Nano, 9(4), 3728-3739, **2015**